DEPARTAMENTO DE ELECTRICIDAD Y ELECTRÓNICA
ELEKTRIZITATEA ETA ELEKTRONIKA SAILA

Universidad del País Vasco
Euskal Herriko Unibertsitatea

Optical properties and high-frequency electron transport in plasmonic cavities

Thesis submitted by

Olalla Pérez González

for the degree of

Philosophiae Doctor, Ph.D.

Supervised by

Nerea Zabala and Javier Aizpurua

Leioa, October 2011

ABSTRACT

Along this thesis we present several contributions to improve the understanding of the interaction between the optical properties of plasmonic nanostructures and electronic transport.

Chapter 1 provides an introduction to the emerging fields of nanophotonics and plasmonics in the framework of nanoscience and nanotechnology. The main concepts regarding the electromagnetism of metals and plasmon excitations are revised. The connection between optical properties and nanoelectronics is also presented.

This thesis is devoted to study the optical response of a plasmonic dimer where both sides of the nanostructure are connected by an ensemble of molecules, focusing on the relation between the fields of plasmonics and nanoelectronics. The molecules are modelled as a conductive material linking the dimer. The dielectric response of the linker has been characterized using different approaches to understand its impact on the optical properties of the whole system.

In chapter 2 the Localized Surface Plasmon Resonances (LSPRs) gov-

erning the optical response of a conductively connected dimer are introduced. The conductance of the linker is shown to be the crucial magnitude influencing the response.

Chapter 3 presents a model to connect the optical and transport properties by means of a pure conductive linker connecting a plasmonic dimer. The influence of the conductive linker in the optical properties is analyzed. Time-scale arguments are used to derive analytical expressions which provide the thresholds of conductance which determine the optical response. The effects of the size of the conductive linker and its morphology are also studied in detail.

In order to describe the linker connecting the dimer in a more realistic way, Chapter 4 explores the optical response of the nanostructure when the material forming the linker presents an excitonic transition. The presence of an exciton substantially alters the behaviour of the LSPRs. Different dielectric responses of the molecular linker are considered by means of changes in the characteristics of the excitonic transition. It is confirmed that the expressions for the thresholds of conductance derived from time-scale arguments for the pure conductive linker are still valid, even though a more complex optical spectrum is produced due to the coupling of plasmons and excitons in this case.

Due to the potential application of plasmonic nanostructures as sensors, Chapter 5 studies the efficiency of plasmonic structures conductively connected for LSPR sensing. Finally, a new paradigm for LSPR sensing is proposed, in which the magnitude to be exploited in sensing is the change in the intensity of the LSPR, rather than the shift of the resonance.

ACKNOWLEDGEMENTS

En los últimos meses he pensado mucho en una película que vi por primera vez en mi adolescencia, “The loneliness of the long-distance runner”. En ella, Tom Courternay da vida a un adolescente británico que, internado en un reformatorio para adolescentes problemáticos, encuentra una válvula de escape en las carreras de larga distancia, siempre corriendo, siempre hacia delante, sin volver la vista atrás.

A lo largo de esta tesis me he sentido así varias veces, sobre todo en la última etapa: no sabía ni cómo, ni por qué, ni para qué, pero seguía adelante con mi particular maratón. Ahora que se acerca el ansiado final, nearly free at last, he de reconocer que ha habido momentos en los que me he sentido totalmente exhausta, casi sin fuerzas y, a veces, hasta sin ánimo para buscarlas. Sin embargo, una tarde de este lluvioso mes de julio, al comenzar a escribir estos agradecimientos, también me sentí abrumada por la cantidad de personas a las que tenía algo que agradecer y que, sabiéndolo o no, han aportado su granito de arena para que yo acabe mi tesis. Recordé todo lo que he crecido como persona en estos años y lo mucho que he aprendido. Recordé los buenos momentos que he vivido con muchos de vosotros. Recordé los viajes, los congresos, las reuniones, los cafés, las sesiones de queja/terapia compartida... Y entonces

entendí por qué tenía que acabarla.

Seguramente me dejaré a muchos y, por falta de espacio, no puedo nombrar a todo el mundo, pero hay algunos que se merecen especialmente unas líneas. Y no puedo comenzar por otros que no sean mis jefes.

A Nerea me gustaría agradecerle la oportunidad que me brindó cuando, sin apenas conocerme, decidió dirigirme la tesis. Muchas gracias por tu ayuda incondicional, por tu total disposición, por tus consejos, los científicos y los no científicos, por tu punto de vista siempre tranquilizador, y, sobre todo, por haber sido una jefa y compañera envidiable.

A Javi me gustaría agradecerle lo muchísimo que me ha ayudado, en todos los sentidos, a lo largo de estos años. Muchas gracias por tus consejos, por la oportunidad que me has dado de asomarme a un mundo tan interesante, por tus ánimos, pero sobre todo, por ayudarme y motivarme a sacar lo mejor de mí.

A ambos, muchas gracias por formar, ya, parte de mi vida, y por todos los buenos momentos compartidos, en Leioa, en Donostia, en un barco huyendo de las cenizas de un volcán y en otros tantos sitios.

No puedo olvidarme tampoco de un centro tan particular como el DIPC, y del CSIC, ya que sin su apoyo económico esta tesis no hubiera sido posible. Por supuesto, gracias a todas las personas de la administración de estos centros que con su ayuda han hecho que el no estar físicamente en Donostia no fuera un problema.

I would also like to thank Professor Peter Nordlander for his support along this work. Thank you for your ideas, your e-mails and discussions and also for being so encouraging and so kind with me, it has been a real pleasure to work with you. Tack!!

Gracias a todos mis compañeros del Departamento de Electricidad y Electrónica de Leioa y a los del DIPC, CFM y nanoGUNE de Donostia por los buenos ratos compartidos. A Esti y a Patricia por todos los cafés, por las charlas, por vuestro apoyo y porque no sé qué hubiese hecho sin

vosotras!! Al club del tupper por hacerme tan agradables las comidas. A Esti Asua por su ayuda para que el formato de la tesis quedara como yo quería. A Axi porque, aunque hemos trabajado en temas diferentes, hemos compartido jefa, y eso une mucho. Gracias por ayudarme con UNIX, pero sobre todo por escucharme y animarme. Specially, I would like to thank all the members and former members of the Nanophotonics Group in the CFM, Alberto, Aitzol, Alejandro, Nicolas, Rubén, Jianing, Ameen, and Pablo. It has been a pleasure to work and travel with you, and, specially it has been great to have the opportunity to meet you. Rubén, no sé cómo agradecerte todo lo que me has ayudado con la computación, dudas generales, etc... Te debo una campeón!! Aitzol, muchas gracias por tu ayuda técnica y anímica y, sobre todo, por tu amistad, te echo de menos!!!

I also have to mention all the people I have had the opportunity to meet along these years in courses, workshops, schools, conferences, the CUBIHOLE European project, etc... It has been a great experience to meet and keep in touch with people from so many different places. Thanks for showing me that there are many ways to live science and life.

A Sol por darme tanto sin pedir nada a cambio y por enseñarme que siempre hay que seguir adelante, aunque no sepamos cómo.

Gracias a tod@s mis amigos de la uni, que muchos habéis seguido siendo compañeros de fatigas en la investigación, por acompañarme en una de las etapas más intensas de mi vida. Gracias Txema tu capacidad para hacerme reir hasta en los peores momentos, y gracias Tamara por estar siempre a mi lado.

A toda mi gente de la escuela porque sin agarrarme a la barra de una clase de ballet, sin las puntas, las agujetas, las actuaciones, los tules, los corchetes y sobre todo, sin vosotras, todo habría sido mucho más dificil.

A mis amig@s de siempre por entender lo absorbida que he estado últimamente y respetarlo. Por hacerme saber con una sonrisa que seguís

a mi lado, aunque ya no nos veamos ni hablemos todos los días, y porque lo que soy a día de hoy es en parte por vosotr@s. En especial, gracias María por todo tu apoyo cuando estábamos a punto de teminar nuestras carreras, porque quizá sin él no hubiese empezado esta aventura.

A mi maravillosa familia no tradicional, a los que estáis y a los que desgraciadamente ya no, porque sois lo mejor que me ha podido pasar en la vida. A tod@s los que me han animado este verano, y otros, mientras curraba en una habitación en Otero. A mi ahijada Lidia por regalarme su sonrisa. A Macu por sus preciosas fotos y por mil cosas más. A la familia de mi chico por aceptarme con los brazos abiertos aunque les haya *robado* a su niño. A mis abuelos por ser el mejor ejemplo en el que fijarme y por enseñarme, a mis padres y a mí , la importancia de la educación que a ellos la guerra y la miseria les negó. A Julián y a Arantza, y a toda la tropa de Eibar y Lujua, por quererme tanto cuando en principio no os tocaba nada. Y a Ama y a Papá por mimarme, reñirme, respetarme, apoyarme y, sobre todo, por quererme como sólo ellos pueden hacerlo. En especial, gracias Ama por creer en mí más que yo misma.

Finalmente, a Fermín, al que le agradezco tanto, que no sé ni por donde empezar. Gracias por todo tu apoyo a lo largo de esta tesis, sabes que también es tuya. Gracias por aguantar mis nervios y mis malos humores, los domingos trabajando, los retrasos, los agobios, espero saber compensarte... Tú y yo sabemos que esto es sólo el principio, que lo mejor está aún por llegar. Sobre todo, gracias por compartir tu vida conmigo, jamás imaginé que la física pudiera hacerme un regalo tan bonito.

Gracias de nuevo a los que he nombrado y a los que no, os quiero un montón, de verdad.

Besos para tod@s

CONTENTS

CHAPTER 1

INTRODUCTION

In prehistoric times, before the crucial invention of writing and when knowledge was transmitted orally, human being was able to create primitive technology which allowed the increase of the probabilities of survival and the improvement of the quality of life. From our current perspective, fire (controlled by early humans approximately 1.5 million years ago), agriculture (developed at least 10.000 years ago in Western Asia, Ancient Egypt and India) or the appearance of the wheel (used nearsimustaneously in Mesopotamia, Northern Caucasus and Central Europe from the mid 4th millennium B.C.), may appear as everyday knowledge, but they once formed the primitive basis of our progress. Along History, technology, understood as the application of knowledge for practical purposes, has developed in parallel to the social, political, religious, economical, artistic and scientific evolution of cultures all around the globe. Our current world is the consequence of the astonishing scientific and technological explosion which took place along the XIXth and XXth centuries. In the past, the transfer of knowledge between our basic understanding of natural phenomena and technical purposes used to be a long process. However, nowadays, due to the demanding necessities of our global so-

ciety, the relation between scientific knowledge and technology has been systematized resulting in a rapid transmission between the results of basic research and technological applications.

Nanotechnology, understood as the application of nanoscience, takes advantage of our knowledge of nanometre-sized systems. This multidisciplinary field has emerged in the last decades as one of the most promising areas of technology contributing to human progress, with potential applications in medicine, communication technologies or renewable energy, to cite only a few [1]. Nanophotonics is the branch of nanotechnology which studies the interaction between light and matter on the nanometre size scale. Plasmonics, one of the areas of nanophotonics, explores the interaction of light with nanometre-sized metallic structures supporting Surface Plasmon Resonances (SPRs), which are collective excitations of the electrons in the free electron gas. This thesis explores theoretically the connection between transport and optical properties of plasmonic systems.

In the following, a brief historical introduction to the study of light-matter interaction, nanophotonics and plasmonics is presented. The rest of the chapter is mainly devoted to introduce some basic concepts of electromagnetism applied to metallic nanostructures and to introduce SPRs in a variety of canonical systems. We conclude the chapter introducing the connection between the optical properties of plasmonic systems and their transport properties when an electronic conduction channel is established between plasmonic structures.

1.1 Introduction to nanophotonics and plasmonics

Light, which plays a central role in current technology, has always fascinated human beings. Even before any serious theory explaining its

nature was developed, Romans or medieval masons, for example, were able to surprisingly manipulate light with technology mainly based on trial and error. The well-known Lycurgus cup, a magnificent piece of roman smithery made of ruby glass illustrating the myth of king Lycurgus, looks green in daylight, when observed in reflected light. However, if it is illuminated from the inside, in transmission mode, the cup turns red, showing its glowing ruby colour. This effect is due to the presence of small gold and silver particles in the glass, around $5 - 60$ nm in size [2]. The same effect is also responsible for the colours of stained glass, very popular in Western Europe since the High Middle Ages. Figure 1.1 a) shows a detail of a colourful stained glass window as seen in daylight, in transmitted light, from the inside of the gothic cathedral in Figure 1.1 b). The beautiful ruby red colour has its origin in the presence of tiny gold particles, formed in the process of the fabrication of the glass by the reduction of metallic ions [3]. These colours cannot be appreciated when the windows are observed in daylight from the outside of the building, in a reflected mode of observation. This difference is shown in Figures 1.1 c) and d), where the rose window of the cathedral appears as seen from the inside (c), and from the outside (d) of the building.

Nowadays, we consider the nature of light based on the concept of the wave-particle duality. In simple terms, light, which is emitted and absorbed in discrete packets called photons, exhibits a dual nature, showing corpuscular characteristics when it interacts with matter and behaving as a wave when it propagates. From the corpuscular theory of the XVIIIth century to current quantum electrodynamics, physics has travelled a long route to understand and explain all the physical phenomena related to light. Without any doubt, one of the most important moments along this path was when James Clerk Maxwell published his famous work *A Treatise on Electricity and Electromagnetism* in 1873. Maxwell concluded that light was a form of electromagnetic radiation

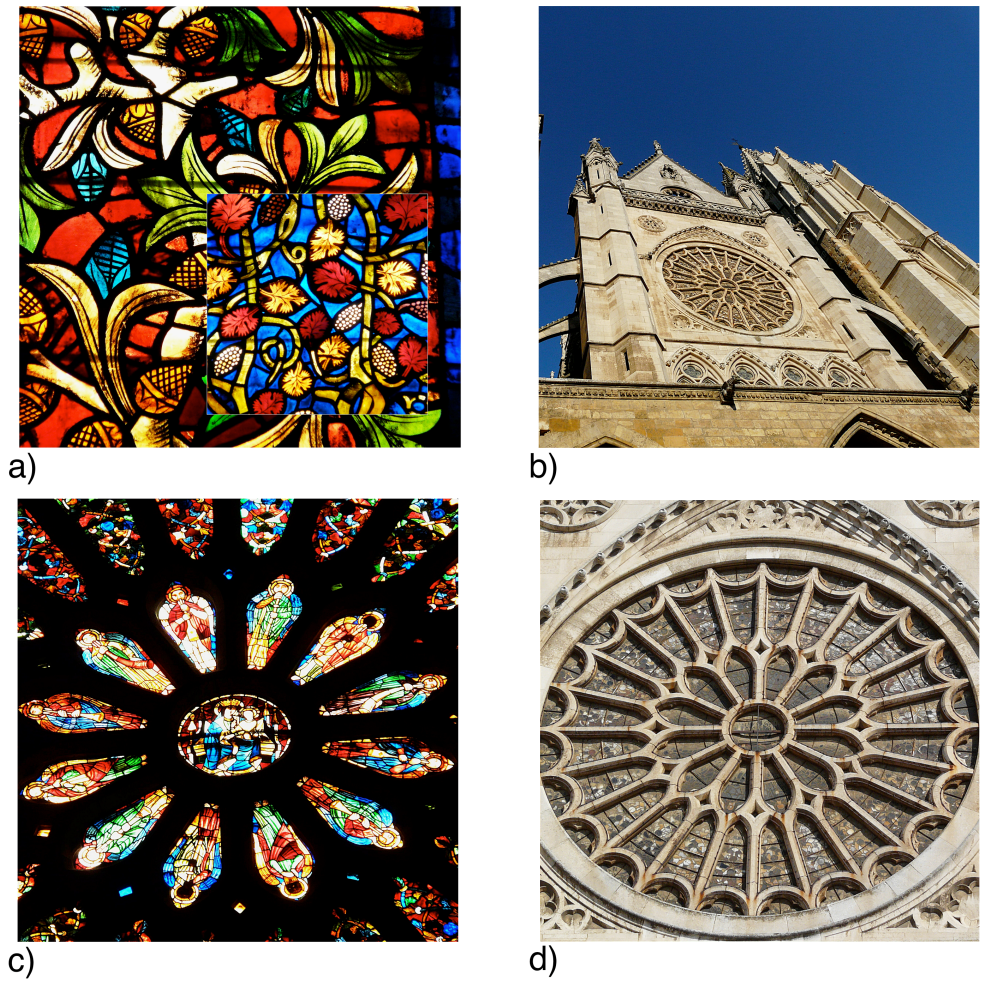

Figure 1.1: a) Detail of a coloured stained glass window of the gothic cathedral of León, Spain (XIIIth century). The beautiful colours appear in daylight when observed from the inside of the building, in transmitted light. b) Outside of the cathedral with stained glass windows. c) Rose window as seen from the inside of the building, in transmitted light. d) Rose window in c), as seen from the outside of the building, in a reflected mode of observation, when the colours cannot be appreciated. (Photographs courtesy of Macu Álvarez).

and reported a full mathematical description of the dynamics of the electromagnetic fields governed by what is nowadays known as Maxwell's equations [4]. Ironically, when Maxwell's wave theory of light was confirmed by the experiment by H.R. Hertz in 1887, the photoelectric effect was also discovered. This effect was later explained by Albert Einstein in terms of a corpuscular theory of light [5]. The study of the interaction of electromagnetic waves and matter contributed to the progress of the theory of electromagnetic radiation, which culminated in the development of quantum electrodynamics by Richard Feynman, Julian Schwinger, Shin-Ichiro Tomonaga, and others.

In the last part of the XXth century, nanotechnology, boosted by breakthroughs such as the development of the scanning tunneling microscope [6], arose as the area of science and technology which explores the properties of matter in the range of the nanometre. Nowadays, even though scientific research has become so specialized, nanotechnology can only be understood as a multidisciplinary area of basic science and technology where different disciplines, such as physics, chemistry, biology, medicine and engineering, merge harmoniously.

Nanophotonics, understood as the study of the interaction between light and matter on the nanometre size scale, has become a frontier branch of nanotechnology providing new challenges for research and novel technologies. Nanophotonics explores phenomena such as the confinement of light to dimensions which are much smaller than the wavelength of light, or the interaction between light and matter when the dimension of the materials is on the nanometric scale [7]. Another approach of this area is the study of the confinement of a photoprocess where the change in the chemical phase is light-induced [7]. Among the opportunities provided by nanophotonics, one can find novel synthetic routes of nanomaterials [8], single photon sources for quantum information processing [9], nanoscale nonlinear optical processes [10], devices based on

photonic crystals [11] or optical nanoprobes for clinical diagnosis [12].

In the last years, the interaction between electromagnetic waves and metallic nanostructures has become particularly important in nanophotonics. Metallic nanostructures support SPRs, which are collective excitations of the electronic charge density localized at the metallic boundaries. The particles sustaining SPRs, which from now on are called plasmonic nanoparticles, exhibit unique optical properties derived from the huge enhancement and localization of the electromagnetic fields associated with the excitation of SPRs. The optical properties of these metallic nanostructures differ from the optical response of the same metallic material in bulk. The differences are not originated by quantum effects of the confinement of the materials, but they appear due to electrodynamical effects and also to the modification of the dielectric environment [7, 13].

Although plasmonics is a novel area of research, the understanding of the optical properties of small particles and the existence of electromagnetic surface waves have been long known. About one century ago, Mie explained the strong absorption of green light by subwavelength gold spheres when illuminated by plane waves by means of classical electrodynamics [14]. SPRs have been studied for decades since the theoretical prediction of plasma losses in metallic slabs by Ritchie in 1957 [15], and the consequent experimental evidence by Powell and Swan [16]. As a fundamental excitation in condensed matter, during the second half of the XXth century, SPRs have been extensively analyzed mainly from the perspective of surface science, giving rise to a good understanding of the SPR properties when excited on metallic surfaces and small particles [17, 18].

With the advent of the new century and thanks to the emergence of sophisticated synthesis methods and analysis tools, a renewed interest in plasmons has been boosted [19]. It has been found that the shape of metallic structures on the nanometric scale and the configuration of the

materials are crucial to determine the surface plasmon properties, what resulted in a big effort in basic and applied investigation searching for potential applications such as biosensing, surface-enhanced spectroscopies, cancer therapies, renewable energies or active devices [20, 21, 22, 23, 24].

When, instead of extended surfaces, metallic nanoparticles are considered, electromagnetic waves are localized on the finite surface of the particle, adopting the terminology of Localized Surface Plasmon Resonances (LSPRs). A key property of metallic nanoparticles is the dependence of the energies of their LSPRs on the geometry of the structure, as well as their sensitivity to the dielectric environment [25, 26]. Thus, depending on the particular property of interest and, by engineering the shape, the materials or the geometric configuration, a huge variety of nanostructures has been synthesized, such as rings, nanoparticle dimers, nanoshells, nanoeggs, rods, nanorices or nanostars [27, 28, 29, 30, 31, 32, 33]. In this thesis, we focus our attention on nanoparticle dimers, as a canonical structure where the energy of the coupled LSPR sustained by the structure can be strongly modified, both in spectral position and intensity, in comparison to the LSPR of the individual constituent nanoparticles.

1.2 Basics of electromagnetism in metals

The interaction between electromagnetic fields and metals is described by means of classical electrodynamics. Even for nanometre-sized particles, the high density of free carriers in metallic materials implies a negligible separation between the energy levels of the electrons in comparison to the thermal excitation $k_B T$ at room temperature and, consequently, in many practical situations there is no need to use quantum theory to describe the optical response [13].

In this section, we review important ingredients of electromagnetism involved to understand the interaction between light and metallic mate-

rials. We also introduce the dielectric formalism within linear response theory describing the response of metals.

Note that along this thesis, we use Gaussian units to express the mathematical expressions, otherwise it is explicitly pointed out.

1.2.1 Maxwell's equations and constitutive relations of materials

The description of the interaction between light and matter, in the framework of classical electrodynamics, is summarized by Maxwell's equations. In Gaussian units, Maxwell's equations are expressed in a differential form as follows [4]:

$$\nabla \cdot \mathbf{D} = 4\pi\rho, \tag{1.1}$$

$$\nabla \cdot \mathbf{B} = 0, \tag{1.2}$$

$$\nabla \times \mathbf{E} + \frac{1}{c}\frac{\partial \mathbf{B}}{\partial t} = 0, \tag{1.3}$$

$$\nabla \times \mathbf{H} - \frac{1}{c}\frac{\partial \mathbf{D}}{\partial t} = \frac{4\pi}{c}\mathbf{j}, \tag{1.4}$$

where $\mathbf{E}$ and $\mathbf{H}$ are the electric and magnetic fields. $\mathbf{D}$ is the electric displacement vector and $\mathbf{B}$ is the magnetic flux density or magnetic induction. These four macroscopic fields ($\mathbf{E}$, $\mathbf{H}$, $\mathbf{D}$ and $\mathbf{B}$) are thus related via Maxwell's equations to the external charge and current densities, ρ and $\mathbf{j}$ respectively.

The electric and magnetic fields, $\mathbf{E}$ and $\mathbf{H}$, are related to the electric displacement $\mathbf{D}$ and to the magnetic induction $\mathbf{B}$ by means of the constitutive relations of the materials. The electric field is connected to the electric displacement vector via the dielectric constant or permittivity ε:

$$\mathbf{D} = \mathbf{E} + 4\pi\mathbf{P} = \varepsilon\mathbf{E}, \tag{1.5}$$

where $\mathbf{P}$ is the polarization. $\mathbf{P}$ describes the electric dipole moment per unit volume in the material, caused by the alignment of the microscopic

dipoles of the material with the electric field. The magnetic field is connected to the magnetic induction via the magnetic permeability μ:

$$\mathbf{B} = \mathbf{H} + 4\pi\mathbf{M} = \mu\mathbf{H}, \tag{1.6}$$

where $\mathbf{M}$ is the magnetization. $\mathbf{M}$ describes the magnetic moment per unit volume in the material, i.e., the magnetic response of the material. Typically, the magnetic response of metallic materials at optical frequencies is several orders of magnitude smaller than the dielectric response at the same frequencies and, for this reason, the diamagnetic and paramegnetic properties are usually neglected in comparison to the dielectric properties when the optical electromagnetic field interacts with a metallic medium [34]. In this thesis, we follow this assumption supposing that the imaginary component of the permeability is zero, and that $\mu = 1$.

Another important relation to point out is Ohm's law, relating the electric field $\mathbf{E}$ to the current density $\mathbf{j}$ [34]:

$$\mathbf{j} = \kappa\mathbf{E}, \tag{1.7}$$

where the relation is defined in terms of the conductivity κ, which is the magnitude describing the ability of a certain material to conduct the electrical current. The complex conductivity, $\kappa = \kappa_1 + i\kappa_2$, and the dielectric constant, $\varepsilon = \varepsilon_1 + i\varepsilon_2$, can be related by the following expression [34]:

$$\varepsilon = 1 + i\frac{4\pi\kappa}{\omega}. \tag{1.8}$$

This relation implies that the real part of the dielectric function ε_1 is related to the imaginary contribution of the conductivity σ_2, and viceversa as follows:

$$\varepsilon_1 = 1 - \frac{4\pi\kappa_2}{\omega}, \tag{1.9}$$

$$\varepsilon_2 = \frac{4\pi\kappa_1}{\omega}. \tag{1.10}$$

We finish this section introducing the wave equations for the electromagnetic field in the case of vacuum and in the presence of matter. In

vacuum and in the absence of external charge and free current ($\rho = 0$ and $\mathbf{j} = 0$), when applying vector identities to Maxwell's equations (see Eqs. (1.1) to (1.4)), the following relations are obtained [34]:

$$\nabla^2\mathbf{E} = \frac{1}{c^2}\frac{\partial^2\mathbf{E}}{\partial t^2}, \tag{1.11}$$

$$\nabla^2\mathbf{B} = \frac{1}{c^2}\frac{\partial^2\mathbf{B}}{\partial t^2}. \tag{1.12}$$

The above equations correspond to a partial differential equation describing the propagation of a wave, of amplitude u and velocity v, generically expressed as:

$$\nabla^2 u = \frac{1}{v^2}\frac{\partial^2 u}{\partial t^2}. \tag{1.13}$$

In the case of an electromagnetic wave, the velocity corresponds to the speed of light in vacuum $v = c$. Thus, Maxwell's equations show implicitly that both the electric and the magnetic fields can adopt the form of propagating waves, stressing the wave nature of light.

In the presence of matter and in the absence of external charge and free current ($\rho = 0$ and $\mathbf{j} = 0$), the wave equations are expressed as [34]:

$$\nabla^2\mathbf{E} = \frac{\varepsilon\mu}{c^2}\frac{\partial^2\mathbf{E}}{\partial t^2} + \frac{4\pi\mu\kappa_1}{c^2}\frac{\partial\mathbf{E}}{\partial t}, \tag{1.14}$$

$$\nabla^2\mathbf{B} = \frac{\varepsilon\mu}{c^2}\frac{\partial^2\mathbf{B}}{\partial t^2} + \frac{4\pi\mu\kappa_1}{c^2}\frac{\partial\mathbf{B}}{\partial t}, \tag{1.15}$$

where, in this case, the velocity is $v = c/\sqrt{\varepsilon\mu}$. The new terms in Eqs. (1.14) and (1.15) are associated to the conductivity, and account for the damping of electromagnetic waves in conductive materials.

1.2.2 Dielectric response of metals

As a consequence of the strong dependance of the optical properties of metallic materials on frequency, there is a big variety of unexpected optical phenomena when studying the optical properties of metallic nanostructures.

In the low-frequency regime, for frequencies up to the visible range (see the electromagnetic spectrum shown in Figure 1.2), metals behave as perfect conductors and do not allow the penetration of electromagnetic waves into the material. When higher frequencies are considered, towards the visible and Near-InfraRed (NIR) ranges of the electromagnetic spectrum, the penetration of the field into the metal is no longer negligible. Thus, under these conditions, a strategy based on the size-scaling of metallic structures working properly at lower frequencies, such at radio-frequency or microwave wavelengths, is not straightforward. For frequencies in the ultraviolet range, metals behave as dielectric materials and allow the propagation of electromagnetic waves inside them with different degrees of attenuation related to the details of the particular electronic band structure [13].

The optical response of metals and the dispersive behaviour pointed out above are described by means of a dielectric response function $\varepsilon = \varepsilon(\mathbf{k}, \omega)$, which, in principle, depends on both the momentum $\mathbf{k}$ and the frequency ω of the incoming electromagnetic signal [35, 36]. There have been many approximations to the dielectric function. Lindhard [37] obtained an expression using the random phase approximation, where the electrons are assumed to respond to the external fields independently. Mermin [38] modified this approximation to take into account the damping of the electronic oscillations. However, when the main interest is the collective excitation of the free electron gas of metals, the dependence of the dielectric response on the momentum can be surpassed, using the optical approximation where $\varepsilon = \varepsilon(\mathbf{k} \to 0, \omega) = \varepsilon(\omega)$ [36]. This approximation is valid as long as the wavelength inside the material is longer than its characteristic dimensions, i.e., the dimension of its unit cell or the mean free path of the electrons.

The simplest dielectric response function describing the behaviour of a metallic material is based on the Drude model. This model considers

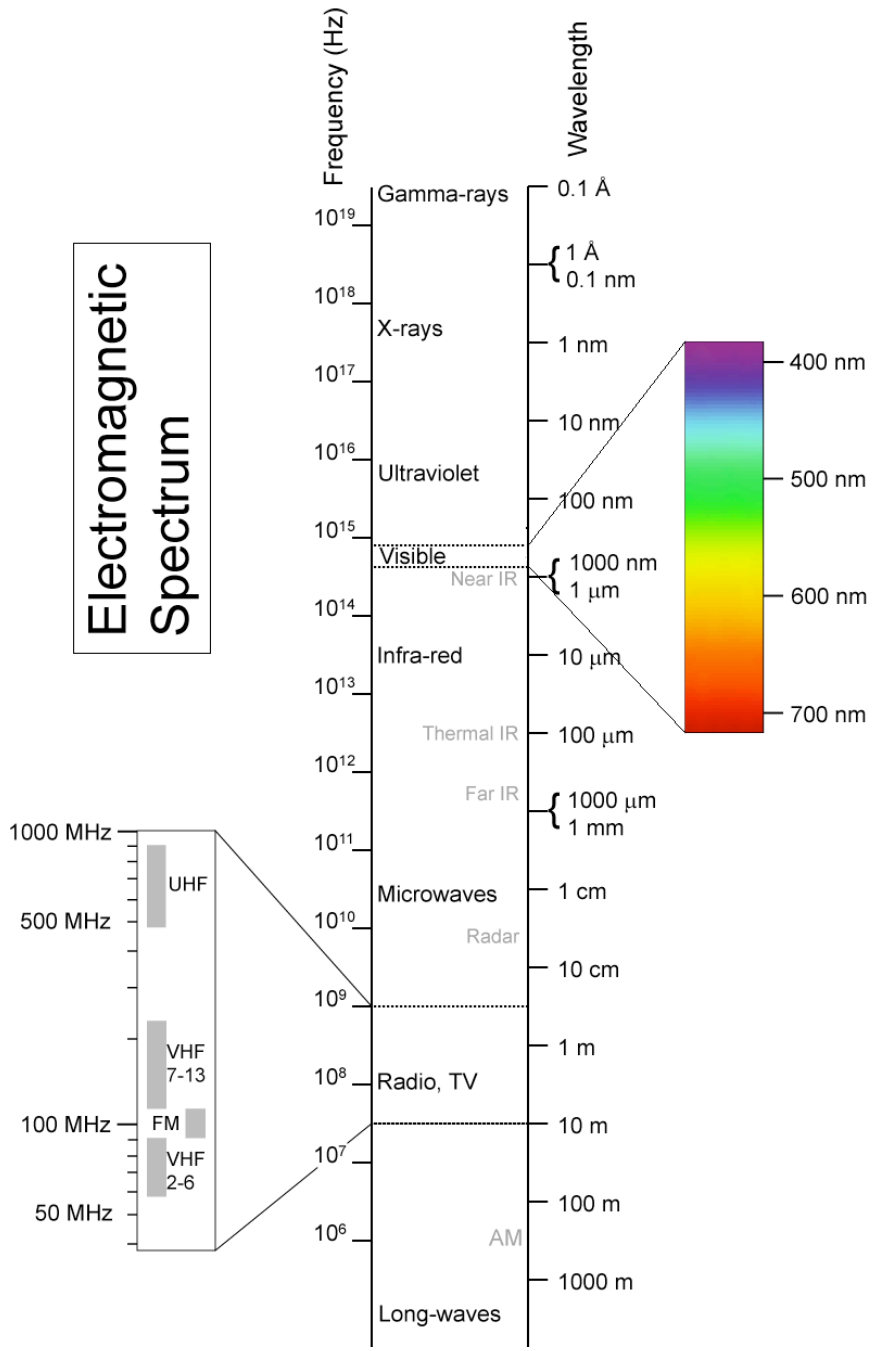

Figure 1.2: Band division of the electromagnetic spectrum (Source: *Creative Commons*).

that the metal is formed of a core of positive ions and free electrons in the vicinity characterized by a damping constant γ. The explicit expression of the dielectric function giving account for the energy losses of these free electrons is the following:

$$\varepsilon(\omega) = \varepsilon_1(\omega) + i\varepsilon_2(\omega) = 1 - \frac{\omega_p^2}{\omega(\omega + i\gamma)}, \tag{1.16}$$

where ω_p is the plasma frequency, a natural frequency of the collective oscillations of the electron gas (its physical meaning is discussed in more detail later). Figure 1.3 a) shows the real and imaginary parts of a Drude dielectric function used to describe the optical response of aluminum. The parameters defining the function for Al are $\omega_p = 15.3$ eV and $\gamma = 0.1$ eV [35]. A zoom-in is also included to show the details of the function in the proximity of the plasma frequency ω_p. The damping constant of the metal γ basically takes into account the relaxation of the motion of the electron gas into lattice vibrations or phonons. Considering $\gamma = 0$ implies that the motion of the electron gas does not decay and Eq. (1.16) reduces to:

$$\varepsilon(\omega) = 1 - \frac{\omega_p^2}{\omega^2}. \tag{1.17}$$

This situation is commonly used to easily calculate the position of modes.

A more detailed description of a particular material is provided by means of the experimental dielectric response function. This function is usually obtained from experimental optical data, based on the measurement of the reflectance of the metal [39]. In Figure 1.3 b) the real and imaginary parts of ε are plotted for the experimental dielectric function of gold [40]. Although the experimental function still resembles the form of a Drude-like function, the included zoom-in shows that the spectral details in the proximity of ω_p differ from the form of the Drude model and that other features, including inter-band transitions, can be described better by the experimental function.

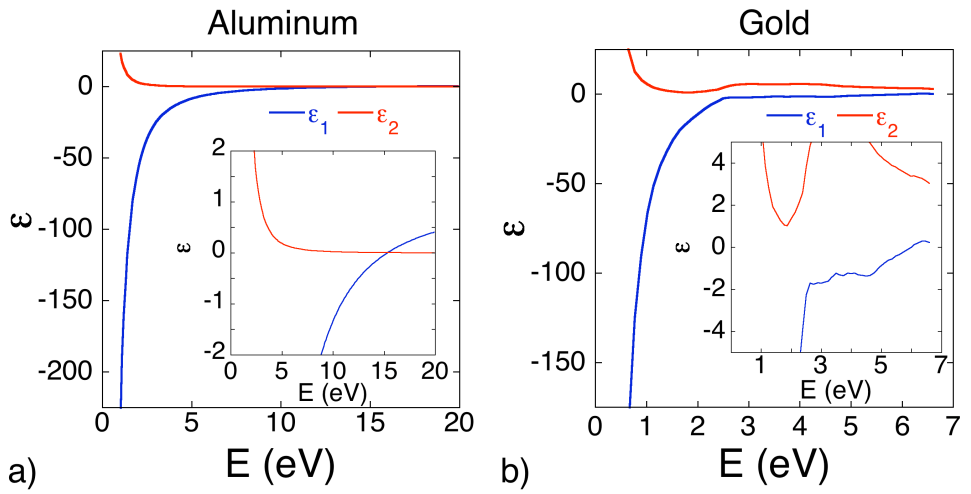

Figure 1.3: a) Real ε_1 and imaginary ε_2 parts of the Drude dielectric response function $\varepsilon = \varepsilon_1 + i\varepsilon_2$ for Al. The defining parameters are $\omega_p = 15.3$ eV and $\gamma = 0.1$ eV [35]. b) Real ε_1 and imaginary ε_2 parts of the dielectric response function $\varepsilon = \varepsilon_1 + i\varepsilon_2$ for Au from the experimental optical data by Johnson and Christy [40].

1.3 Plasmons

In this section, we introduce the concept of SPR as the collective oscillation of the free electron gas. We also show the extension of this concept to a situation where planar interfaces are present. Finally, we focus on the localization of SPR on the surfaces of finite-sized particles.

1.3.1 Collective electromagnetic oscillations of the free electron gas: bulk plasmons

A solid can be described as an electrically neutral medium where there is equal concentration of positive and negative charges, being one of them mobile [35]. In metals, the negative charges of the free mobile conduction electrons are compensated by the positive charges of the ion

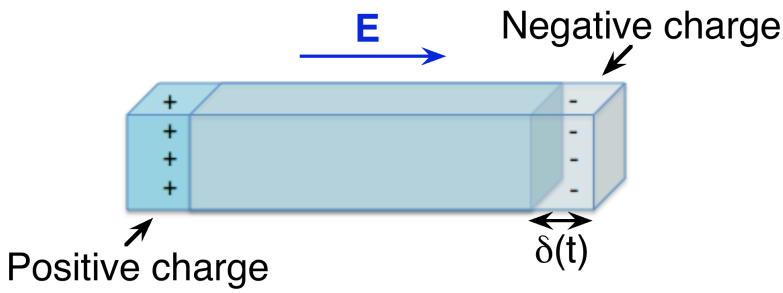

Figure 1.4: Schematic representation of a bulk plasma oscillation in a metal. The action of an electric field **E** produces the deviation of the free electron gas from its equilibrium position. The positive ion cores induce a restoring force to move the electron cloud back to its original position, causing a collective oscillatory motion of the electron gas around the equilibrium position.

cores. When an electric (or electromagnetic) signal $E(t)$ is applied to a metal, the electron gas reacts to this incoming field displacing the electrons a certain distance $\delta(t)$ from the equilibrium position, as depicted in Figure 1.4. As a consequence, the positive ion cores induce a restoring force which induces the motion of the electron cloud back to its original position. The simultaneous action of these two forces causes a collective oscillatory motion of the electron gas around the equilibrium position which is damped due to the collisions of the mobile electrons with the lattice. This damped motion is characterized by a damping constant γ, which is relatively large in metals at optical frequencies.

The dielectric response of the electron gas is derived from the equation of motion of an electron in an electric field [13, 35]:

$$m_e \frac{d^2\delta(t)}{dt^2} + m_e\gamma\frac{d\delta(t)}{dt} = -eE(t), \tag{1.18}$$

where m_e and e are the mass and electric charge of an electron, respectively, $\delta(t)$ is the displacement of the electron gas, γ is the damping constant and E is the incident electric field. Both $\delta(t)$ and $E(t)$ have the same harmonic temporal dependance, $\delta(t) = \delta e^{-i\omega t}$ and $E(t) = Ee^{-i\omega t}$.

We assume this dependence and establish Eq. (1.18) in the Fourier-transformed space:

$$-\omega^2 m_e \delta - i\omega m_e \gamma \delta = -eE. \tag{1.19}$$

The polarization, defined as the dipolar moment ($p = -e\delta$) per unit volume is given by:

$$P = -ne\delta = -\frac{ne^2}{m_e(\omega^2 + i\gamma\omega)}E, \tag{1.20}$$

where n is the electron concentration. The dielectric function at a given frequency is (see Eq. (1.5)):

$$\varepsilon(\omega) = \frac{D}{E} = \frac{E + 4\pi P}{E} = 1 + 4\pi\frac{P}{E}. \tag{1.21}$$

Taking into account Eq. (1.42), we can express $\varepsilon(\omega)$ as:

$$\varepsilon(\omega) = 1 - \frac{4\pi ne^2}{m_e(\omega^2 + i\gamma\omega)} = 1 - \frac{\omega_p^2}{(\omega^2 + i\gamma\omega)}, \tag{1.22}$$

where a natural frequency of the oscillation of a free electron gas, or plasma frequency ω_p, is defined as:

$$\omega_p \equiv \frac{4\pi ne^2}{m_e}. \tag{1.23}$$

Since we have assumed that all the electrons move in phase, these oscillations correspond to the long-wavelength limit where $\mathbf{k} = 0$. The quanta of these charge density oscillations are called bulk plasmons. The plasma frequency of metals can be determined experimentally by means of Electron Energy Loss Spectroscopy (EELS), where fast electrons travel through portions of metallic materials loosing energy in quanta of $\hbar\omega_p$ due to the excitation of bulk plasmons. Typically, for most metals, the plasma frequency falls in the visible-ultraviolet regime, $2-15$ eV, whereas for doped semiconductors, with lower free carrier concentration, plasma

frequencies at InfraRed (IR) and THz regimes can be found [35].

The effects of the plasma oscillations for frequencies below the plasma frequency ω_p, where the real part of the dielectric constant ε_1 is negative, lead to electromagnetic properties which differ from those of ordinary dielectrics in that spectral range. In this frequency range, the wave vector of light in the medium is imaginary, consequently, electromagnetic waves cannot propagate.

1.3.2 Surface plasmons and surface plasmon polaritons

When we consider a surface in a metal which breaks the symmetry of the bulk material, electron plasma oscillations or Surface Plasmons (SPs) can be sustained at the surface [41]. The frequency of a SP excitation ω_{SP} on the flat surface dividing space into two semi-infinite regions, being one of the regions a metal and the other one a dielectric, is determined based on the boundary conditions for the electromagnetic field at the metal-dielectric interface.

In the following, we derive the explicit expression in the electrostatic approximation, without retardation effects, by solving the problem of two semi-infinite media separated by a flat surface (see Figure 1.5 a)). The metallic medium is characterized by the frequency dependent dielectric functions $\varepsilon_m(\omega)$ and the dielectric medium is characterized by $\varepsilon_d(\omega)$. Since there is no electric charge, the solution of the electrostatic problem consists in solving Laplace's equation for the particular boundary conditions:

$$\nabla^2\phi = 0, \tag{1.24}$$

where ϕ is the electrostatic potential. This procedure leads to the following resonance condition for the electromagnetic modes:

$$\varepsilon_m(\omega) + \varepsilon_d(\omega) = 0. \tag{1.25}$$

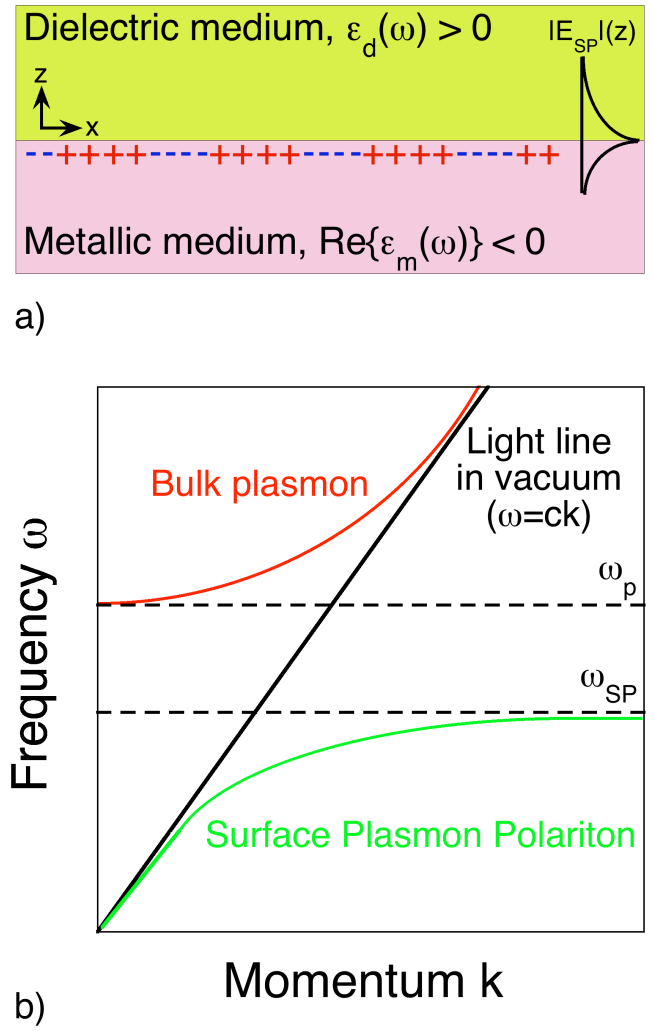

Figure 1.5: a) Simplest geometry sustaining SPPs: two semi-infinite media separated by a flat interface, where one of the media is a dielectric characterized by $\varepsilon_d(\omega) > 0$, and the other one is a metal with $\mathrm{Re}\{\varepsilon_m(\omega)\} < 0$. The black lines in the schematic indicate the decay of the field associated with SPPs at each medium. b) Representation of the dispersion curves for bulk plasmon (red line), light in vacuum (black line) and SPP (green line). The frequencies of the bulk plasmon ω_p and the SP ω_{SP} are also marked with dashed black lines.

If the frequency dependent dielectric functions for the metal is expressed as a Drude function without damping, $\varepsilon_m(\omega) = 1 - \omega_p^2/\omega^2$, and the dielectric constant characterizing the dielectric medium is ε_d then, the frequency of the plasmon excitation on the surface is:

$$\omega_{SP}^2 = \frac{\omega_p^2}{1+\varepsilon_d}, \tag{1.26}$$

where ω_p is the plasma frequency of the metallic medium. When the dielectric medium is vacuum, Eq. (1.25) leads to the semi-infinite surface plasmon resonance frequency:

$$\omega_{SP} = \frac{\omega_p}{\sqrt{2}}. \tag{1.27}$$

Surface Plasmon Polaritons (SPPs) are electromagnetic excitations propagating at interfaces, resulting from the coupling of a SP to light [41]. These excitations are evanescently confined in the perpendicular direction to the interface. In general, plasmons do not couple to photons (see the dispersion curve for SPPs in Figure 1.5 b)).

The simplest geometry sustaining SPPs is a flat interface separating a semi-infinite, loss-less dielectric and a semi-infinite metal, characterized by frequency-dependent dielectric functions $\varepsilon_d(\omega)$ and $\varepsilon_m(\omega)$, respectively (see Figure 1.5 a)). Whereas for the loss-less, dielectric medium $\varepsilon_d(\omega) > 1$, note that for the metal $Re\{\varepsilon_m(\omega)\} < 1$. In order to derive the wave solutions propagating at the interface, Maxwell's equations are solved considering the appropriate boundary conditions. The dispersion relation of SPPs propagating at the interface between the two media is given by [13, 41]:

$$\omega_{SPP} = \sqrt{\frac{\varepsilon_m + \varepsilon_d}{\varepsilon_m \varepsilon_d}} ck. \tag{1.28}$$

Assuming a Drude function for the metal, $\varepsilon_m(\omega) = 1 - \omega_p^2/\omega^2$, one obtains the dispersion curve for SPPs shown in Figure 1.5 b), where the ω_p and ω_{SP} are also included.

1.3.3 Localized surface plasmons

Localized Surface Plasmon Resonances (LSPRs) are non-propagating excitations which arise from the coupling of light to the charge density oscillations on the closed surfaces of metallic nanoparticles [25]. As in the case of bulk plasmons, an incoming electric signal deviates the electron cloud inside the particle from its equilibrium position. As a consequence, regions of positive and negative charge appear, and the positive background of the nanostructure tries to restore the equilibrium, thus establishing the collective oscillation known as LSPR, schematically depicted in Figure 1.6. The closed, curved surface of the nanoparticle provides the neccesary momentum so that momentum conservation is fulfilled and light can couple to the electromagnetic excitation.

These localized electromagnetic modes arise naturally from the scattering problem of a small sub-wavelength nanoparticle in an oscillating electromagnetic field. We begin studying explicitly the case of the electromagnetic modes of a spherical metallic nanoparticle. We also summarize the results of other geometries and, finally, we introduce the plasmon hybridization picture explaining the plasmonic modes of more complex nanostructures.

1.3.3.1 LSPRs in spherical geometry

When considering the problem of a metallic sphere with radius R in a dielectric environment under the effect of an incoming electromagnetic field, the quasi-static approximation is valid as long as the particle is much smaller than the incident wavelength in the surrounding medium, i.e., when $2R << \lambda$ [13]. Under these conditions, the phase of the oscillating electromagnetic field is approximately constant over the volume of the particle, thus, the calculation of the electromagnetic field can be treated as an electrostatic problem. Once the fields are calculated, the harmonic temporal dependence can be added to the solution.

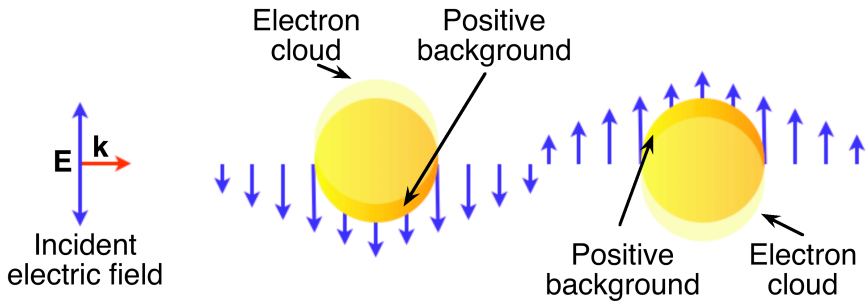

Figure 1.6: Schematic representation of the excitation of a LSPR in a metallic spherical nanoparticle under the influence of a linearly polarized electric field.

In order to describe the electromagnetic surface modes in the quasi-static limit, one needs to solve Laplace's equation using the appropriate boundary conditions. In this case, we consider a metallic spherical particle of radius R and characterized by a frequency-dependent dielectric function $\varepsilon_m(\omega)$ (see Figure 1.7). The particle is embedded in an infinite dielectric medium characterized by $\varepsilon_d(\omega)$. The solution of the problem by means of Laplace's equation leads to the following resonance condition for the fields, which is the equation describing the electromagnetic surface modes:

$$\varepsilon_m(\omega)l + \varepsilon_d(\omega)(l+1) = 0. \tag{1.29}$$

If the response of the metallic nanoparticle is expressed in terms of a Drude-like dielectric function without damping, $\varepsilon_m(\omega) = 1 - \omega_p^2/\omega^2$, and the embedding medium is vacuum, $\varepsilon_d(\omega) = 1$, then, the eigenfrequencies of the surface electromagnetic modes are:

$$\omega_l^{sph} = \sqrt{\frac{l}{2l+1}}\omega_p, \tag{1.30}$$

where l is the order of the spherical harmonic in which the deformations of the electron gas is decomposed due to the spherical symmetry of the problem. Thus, the frequency of the dipolar ($l = 1$) surface plasmon

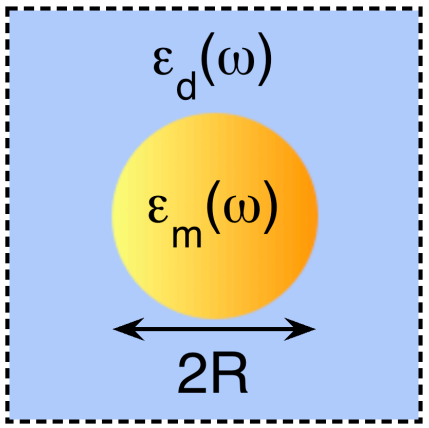

Figure 1.7: Schematic representation of a metallic spherical nanoparticle, characterized by $\varepsilon_m(\omega)$, embedded in a dielectric medium, characterized by $\varepsilon_d(\omega)$.

mode of a sphere in vacuum is given by:

$$\omega_{l=1}^{sph} = \omega_{dip}^{sph} = \frac{\omega_p}{\sqrt{3}}. \tag{1.31}$$

The dipolar mode is the most relevant one in the optical excitation of small spheres. An increase in the size of the sphere makes higher order modes more significant. In the limit of very large spheres ($R \to \infty$), the result for a flat surface is recovered ($\omega_{l\to\infty} = \omega_p/\sqrt{2} = \omega_{SP}$).

LSPRs also appear in the reciprocal situation of voids embedded in metallic media. In order to consider a spherical cavity embedded in a metallic medium, in the geometry depicted in Figure 1.7 we can consider that the sphere is now vacuum and the embedding medium is a metal. Thus, $\varepsilon_d(\omega) = 1$ is the dielectric constant characterizing the cavity and the response of the embedding metal is expressed using a Drude dielectric function $\varepsilon_m(\omega) = 1 - \omega_p^2/\omega^2$. In this situation, the frequencies of the electromagnetic modes are given by:

$$\omega_l^{cav} = \sqrt{\frac{l+1}{2l+1}}\omega_p, \tag{1.32}$$

and the corresponding dipolar mode of a cavity is:

$$\omega_{l=1}^{cav} = \omega_{dip}^{cav} = \sqrt{\frac{2}{3}}\omega_p. \tag{1.33}$$

From these results (see Eqs. (1.30) and (1.32)), an interesting summation rule can be inferred [42]:

$$(\omega_l^{sph})^2 + (\omega_l^{cav})^2 = \omega_p^2. \tag{1.34}$$

1.3.3.2 Other geometries

There is a big variety of metallic nanostructures sustaining LSPRs. As the complexity of the geometry increases, obtaining explicit expressions for the surface electromagnetic modes becomes increasingly difficult. Analytical and semi-analytical solutions have been obtained for the LSPRs in a big variety of nanostructures such as slabs [43], cylinders [44], edges [45], coupled spheres [46] and nanoparticle arrays [47]. However, when one needs to study the optical properties of metallic structures showing complex arbitrary geometries, computational approaches are necessary to solve Maxwell's equations. Some of the most common numerical methods used in the calculation of plasmon modes in complex structures are the Finite Difference Time Domain (FDTD) [48], the Discrete Dipole Approximation (DDA) [49] or the Boundary Element Methods (BEM) [50]. In this thesis, we will use the BEM method to calculate the optical response of the complex plasmonic systems under study, namely, linked metallic dimers. In this method, the boundary conditions are set up at a grid of points defining the surface elements which separate the different dielectric regions defining the particular geometry. Maxwell's equations are solved for each surface element in terms of the effective surface charges and currents self-consistently determined. Once the distribution of the charges and currents is obtained, the near-field and far-field properties can be obtained. Technical information on this method is found in Appendix A of this thesis.

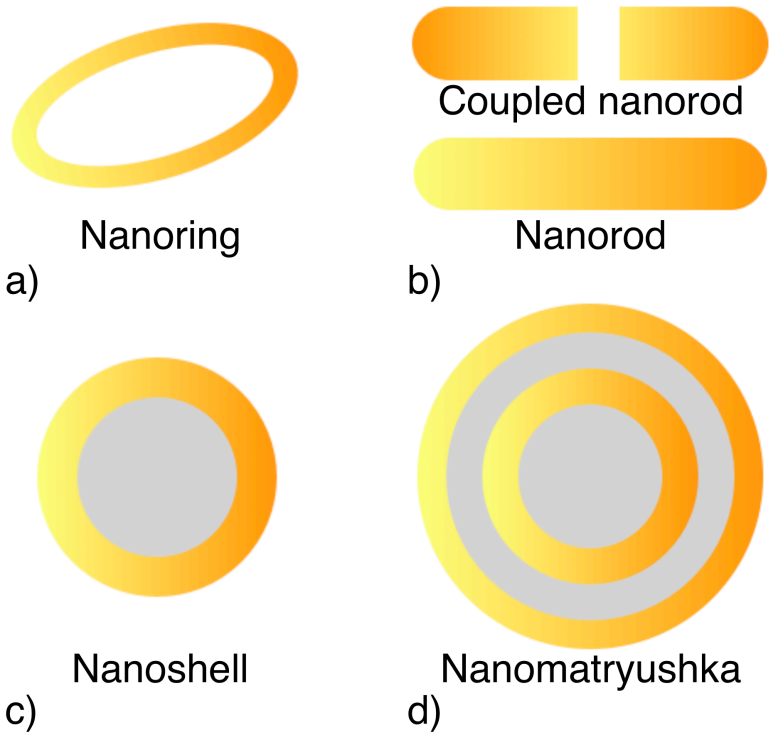

Figure 1.8: Examples of different metallic nanostructures supporting LSPRs. a) Nanorings, b) coupled nanorods (top) and single nanorods (bottom), c) nanoshells and d) nanomatryushkas.

With the help of current computational resources, the optical properties of a huge variety of metallic nanostructures showing complex geometries (see some examples in Figure 1.8) are explored. Among these nanostructures we can find nanorings [27], coupled nanorods and nanorods [31, 51], coupled nanoparticles [28], nanoshells and coupled nanoshells [29], which are structures composed of dielectric cores surrounded by metallic shells, nanomatryushkas [52], which are a succession of concentric dielectric core-metallic shells, nanostars [33], etc... Each structure shows particular optical properties of field localization and radiation rates.

1.3.3.3 LSPRs in complex geometries: hybridization model

In the last years, a hybridization model has been proposed to understand and explain the spectral distribution of the plasmonic modes in coupled nanostructures [54]. The hybridization model is an electromagnetic analog of the orbital molecular hybridization theory, and explains the resonances of complex nanostructures in terms of the well-known plasmonic modes supported by the basic entities forming them. This model has been very successful in understanding the behaviour of metallic nanostructures of increasing geometric complexity such as dimers, nanoshells, nanostars or nanomatryuskas. In this section, we consider the case of a metallic shell to illustrate how the hybridization picture works.

In the electrostatic approximation, the energy of the modes of a metallic shell can also be derived from classical electromagnetic theory. Considering the shell as the particular case of a spherical cavity, with radius R_{cav} and characterized by $\varepsilon_m = 1$, coupled to a metallic sphere in an embedding dielectric medium, with radius R_{sph} and also characterized by $\varepsilon_m = 1$ (see schematics in Figure 1.9), then the resonance condition of the electromagnetic surface modes is:

$$\varepsilon(\omega)^2 + \frac{\varepsilon(\omega)}{1-g_l}\Big[2g_l + \frac{l^2+(l+1)^2}{l(l+1)}\Big] + 1 = 0. \tag{1.35}$$

g_l is a geometric parameter defined as:

$$g_l = \Big(\frac{R_{cav}}{R_{sph}}\Big)^{2l+1}, \tag{1.36}$$

which gives the ratio between the radii of the cavity R_{cav} and the sphere R_{sph}. The frequencies of the plasmon modes of the coupled system are:

$$\omega_l^{\pm} = \frac{\omega_p}{\sqrt{2}}\Big[1 \pm \frac{1}{2l+1}\sqrt{1+4l(l+1)g_l}\Big]^{1/2}. \tag{1.37}$$

The energy of the dipolar mode ($l = 1$) is given by:

$$\omega_{l=1}^{\pm} = \omega_{dip}^{\pm} = \frac{\omega_p}{\sqrt{2}}\Big[1 \pm \frac{1}{3}\sqrt{1+8g_l}\Big]^{1/2}. \tag{1.38}$$

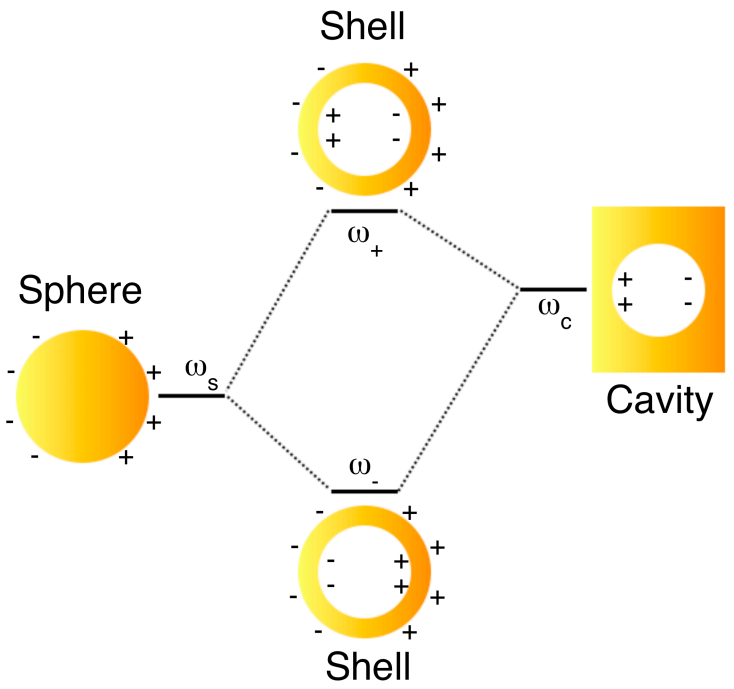

Figure 1.9: Schematic representation of the application of the hybridization model to describe the energy levels of the plasmonic modes of a metallic nanoshell as a result of the hybridization of the plasmon modes of a cavity and a sphere.

In the limit $R_{cav} \to 0$:

$$\lim_{R_{cav}\to 0} \omega_{dip}^{+} = \sqrt{\frac{2}{3}}\omega_p, \tag{1.39}$$

and:

$$\lim_{R_{cav}\to 0} \omega_{dip}^{-} = \sqrt{\frac{1}{3}}\omega_p, \tag{1.40}$$

which correspond to the energies of the dipolar modes of a metallic cavity and a metallic sphere, respectively.

In terms of the hybridization picture, Figure 1.9 shows the plasmon energy-level diagram of a shell arising from the coupling between the modes of the metallic cavity and the metallic sphere. The plasmon

modes of a sphere and a cavity are electromagnetic excitations which induce surface charges at the outer and inner interfaces. Due to the finite thickness of the metallic shell, the plasmon modes of the cavity and the sphere interact, resulting in the splitting of the LSPR into two new LSPR: the bonding plasmon ω_-, with lower energy, and the anti-bonding plasmon ω_+, with higher energy.

This hybridization model has also been applied succesfully to explain the plasmon modes of other systems such as nanoparticle dimers [55]. The success of this picture is mainly based on its simplicity and also on the intuitive way of explaining the complex nature of the electromagnetic surface modes of nanostructures.

1.4 The optical extinction spectrum

Along this thesis, we analyze the optical properties of plasmonic nanostructures mainly in terms of the optical extinction cross-section of the structures under study. In order to understand the physical meaning of this magnitude, we now introduce the basic concepts related to the phenomena of optical extinction, scattering and absorption.

When a particle is illuminated by a beam of light, part of the light is absorbed by the particle, and part of it is scattered in the form of new radiation. The amount of light scattered and absorbed by the particle, as well as the angular distribution of the scattered light, depend on the particular characteristics of the particle, i.e., its shape, size and material properties. Extinction is the attenuation of an electromagnetic wave by the phenomena of scattering and absorption taking place when it illuminates a particular structure. It can be shown [18] that the extinction of an electromagnetic wave after going through a particle only depends on the scattering in the forward direction, even though this phenomenon is an effect of the combination of the absorption in the particle and the

scattering by the particle in all directions.

The study of the scattering phenomena of an incoming electromagnetic radiation, incident in the direction $\mathbf{n}_0$ with polarization $\mathbf{e}_0$, involves the calculation of the scattering cross-section. A cross-section is a quantity with dimensions of area per unit solid angle. The differential scattering cross-section in a certain direction of space $\mathbf{n}$ indicates the power radiated in this direction $\mathbf{n}$ and polarization $\mathbf{e}$, per unit solid angle, per unit incident flux [4].

The general approach to the scattering problem consists in the following: considering an arbitrarily polarized monochromatic wave illuminating the particle, one needs to determine the electromagnetic field distribution to obtain the power radiated in all directions. In general, this is a very complex problem but, there is a particularly relevant case which is exactly soluble: the scattering of light by small spherical particles [14, 18]. Figure 1.10 shows a schematic representation of the absorption, scattering and extinction phenomena when incoming light with linearly polarized electric field $\mathbf{E}$ illuminates a spherical particle.

For small sphere with radius R (characterized by a dielectric function ε_m) embedded in a medium (characterized by ε_d), the electrostatic approximation is valid and the dipolar momentum induced by the presence of a quasistatic uniform electric field $\mathbf{E}_0$ can be expressed as:

$$\mathbf{p} = \varepsilon_d \alpha^{sph} \mathbf{E}_0, \tag{1.41}$$

where α^{sph} is the polarizability of the sphere defined as [18]:

$$\alpha^{sph} = 4\pi R^3 \frac{\varepsilon_m - \varepsilon_d}{\varepsilon_m + 2\varepsilon_d}. \tag{1.42}$$

In the electrostatic approximation, thus, a sphere can be considered an ideal dipole. We can replace the sphere by an ideal dipole with dipolar moment $\mathbf{p} = \varepsilon_d \alpha^{sph} \mathbf{E}_0$ to describe the radiation properties of the particle. Taking this into account, the scattering and absorption cross-sections,

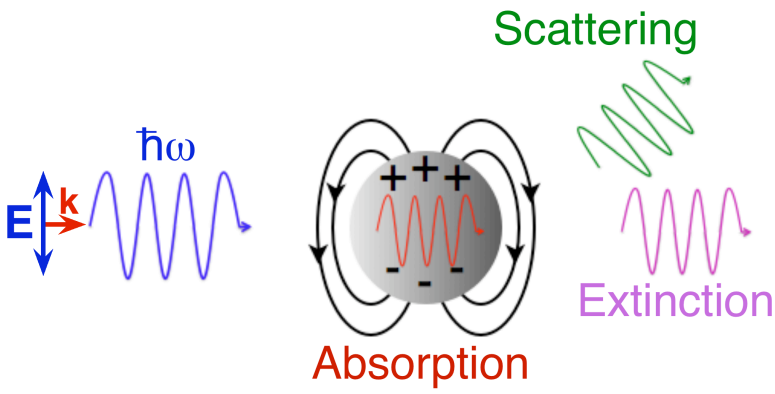

Figure 1.10: Schematic representation of the extinction, scattering and absorption phenomena by a metallic sphere. The incoming light is a plane wave with wave-vector **k** and linearly polarized electric field **E**, exciting the dipolar plasmon mode.

C_{sca} and C_{abs}, can be referred to this dipolar moment and, thus, to the polarizability of the sphere as:

$$C_{sca} = |\alpha^{sph}|^2 \frac{k^4}{6\pi} = \frac{8\pi}{3} k^4 R^6 \left| \frac{\varepsilon_m - \varepsilon_d}{\varepsilon_m + 2\varepsilon_d} \right|^2, \tag{1.43}$$

$$C_{abs} = kIm(\alpha^{sph}) = 4\pi k R^3 Im\left[\frac{\varepsilon_m - \varepsilon_d}{\varepsilon_m + 2\varepsilon_d} \right]. \tag{1.44}$$

For small particles absorption, which scales with R^3, dominates over scattering, which scales with R^6. Finally, once the scattering and the absorption cross-section are known, the extinction cross section can be obtained as the sum of both:

$$C_{ext} = C_{sca} + C_{abs}. \tag{1.45}$$

In Figure 1.11 the calculated normalized extinction, scattering and absorption cross-sections for silver spheres in vacuum are shown. In Figure 1.11 a) we consider a sphere with radius $R = 10$ nm, whereas in Figure 1.11 b) the sphere has $R = 25$ nm as radius. For the smaller particle, the absorption is the most important contribution to the extinction

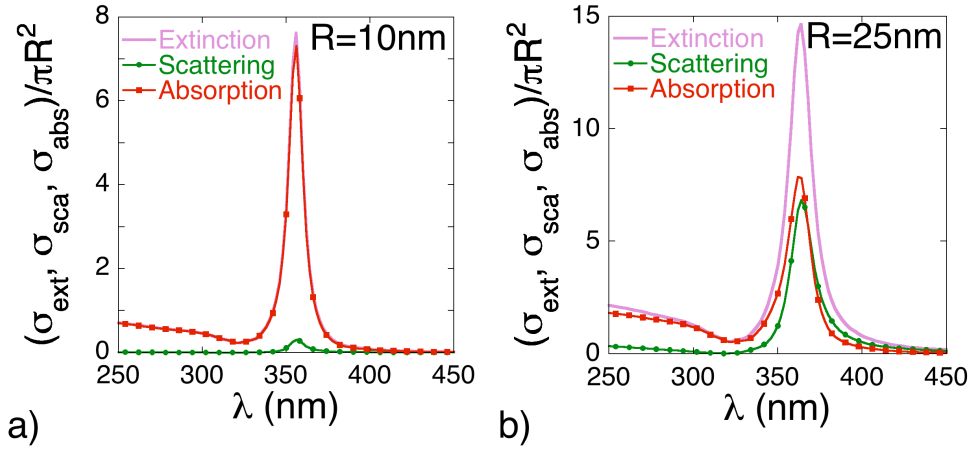

Figure 1.11: Calculated normalized extinction, scattering and absorption cross-section for silver spheres in vacuum with radii a) $R = 10$ nm and b) $R = 25$ nm.

process, being the scattering negligible, due to the scaling of C_{abs} and C_{sca} with R^3 and R^6, respectively. In contrast, when a bigger particle is considered, both contributions are equally important.

1.5 Connecting optical properties and electronic transport

Within the huge diversity of plasmonic nanoparticles, dimers have emerged as a canonical structure due to their important role in the understanding of more complex plasmonic structures. When two nanoparticles are placed next to each other forming a dimer, they no longer behave individually, but as a new interacting system in which the plasmonic modes of the individual nanoparticles interact and can be understood in terms of the hybridization of the plasmonic resonances of the constituent nanoparticles [55]. For very close particles, when there is no conduc-

tive path linking both parts of the dimer, the optical response is mainly governed by the Bonding Dimer Plasmon (BDP) resonance. This BDP mode, which arises from the hybridization of the dipolar modes ($l = 1$) of the individual nanoparticles, presents strongly localized charge densities of opposite sign and enormously enhanced local electromagnetic fields in the dimer cavity. In contrast, for touching particles, where a conductive path is established between both parts of the dimer, the optical response is governed by the Charge Transfer (CTP) mode, which allows electric current density through the cavity, involving an oscillating charge distribution of net charge at every individual nanoparticle [28]. We will introduce these plasmon modes in Chapter 2, before analyzing their connection to electronic transport and excitonic transitions.

In parallel to the development of plasmonic cavities, electronic transport through molecules has become a vibrant field in nanoscience due to its potential technological applications in nanoelectronics, connected to novel nanofabrication and nanomanipulation methods and improved current detection schemes. During the past decade, many fundamental advances in our understanding of molecular transport at DC or low AC frequencies have been achieved. Among this accomplishments we find the single-molecule transistor [56], the measurement of conductance in individual molecules [57], the visualization and resolution of the spectroscopy of metal-molecule-metal structures [58], single-molecule circuits [59], the plasmon-induced electric conduction in molecular devices [60] or the switching of conductance in molecular junctions [61]. In molecular electronics, it is clearly of significant importance to understand transport at GHz or higher frequencies. While there has been significant theoretical effort devoted to understand electron transport through molecular devices and quantum dots at elevated frequencies [62, 63, 64], standard electrical transport measurements cannot be performed in this regime due to the strong capacitive coupling between electrodes. In Chapter 3,

we study the dependence of the optical properties on the conductance in coupled dimers linked by a conductive path between both sides of the dimer nanostructure. We explore the connection between the optical response and the electronic transport processes taking place through the conductive linker.

Furthermore, there has been a growing interest in the interaction between plasmonic modes and molecular excitations, since the control of the coupling of molecular complexes to metallic structures is very important for the development of active plasmonics components dealing with optoelectronics signals [65, 66]. Among the broad range of potential applications of these systems we can find molecular switches, light harvesting structures or modulators [24, 67, 68]. In particular, it has been shown that in systems composed of metal nanoparticle-molecular complexes, the presence of molecules shifts the plasmon mode by changing the interation between the molecular and plasmonic resonances [24]. In Chapter 4, we study how the presence of an excitonic transition in the material linking a metallic dimer influences the optical response of the nanostructure. We also connect the spectral changes and the conduction properties of the excitonic linker.

Along the development of plasmonics, there have been many studies of the sensitivity of plasmonic systems to the embedding medium. These studies have been boosted by the potential use of plasmonic structures as sensors [69, 70]. This sensitivity has been found to be relevant for different types of nanostructures, such as nanorods, nanoshells or nanodisks and, more recently, significant advances have been reported in the sensing capability with the use of Fano resonances [71], due to their sharp spectral features which are more sensitive to the surrounding environment. In Chapter 5, we study the sensitivity of dimers linked by a conductive path to the embedding medium. We also propose a new paradigm for sensing application based on the intensity, rather than on the shift of the

plasmons.

All the topics developed in this thesis point out in the direction of a better understanding of the complex connection between transport properties through metallic structures and the optical properties. This connection promises novel and valuable information which could lead to a new way of characterizing transport at high frequencies.

CHAPTER 2

PLASMONIC RESONANCES IN NANOPARTICLE DIMERS: THE BDP AND CTP MODES

During the last decade, the emerging field of plasmonics has developed a growing interest in the optical properties of coupled metallic nanoparticles due to the potential applications of their localized plasmonic resonances [25, 26]. Among all the variety of existing nanostructures, different nanoparticle pairs, usually named dimers, with different shapes, sizes and materials, have been profoundly studied [28, 29, 31]. A dimer can be considered as a canonical structure which helps to understand the optical behaviour of other nanostructures with increasing complexity.

When the two parts of a dimer are closely located, a cavity is formed. Depending on how close the particles are situated, or whether they establish a conductive contact, two main plasmonic resonances can be distinguished: the Bonding Dimer Plasmon (BDP) mode and the Charge Transfer Plasmon (CTP) mode. In this chapter we explore the general features of these Localized Surface Plasmon Resonances (LSPRs), since they are deeply studied along this thesis in relation to the conduction

properties in the Plasmonic Cavity (PC).

2.1 Plasmonic dimers: from non-conductive to conductive regime

When two metallic nanoparticles are placed next to each other, they no longer behave as the original individual nanoparticles, but as a new structure that we name as dimer. This new nanostructure presents its own plasmon modes due to the coupling between the nanoparticles composing the dimer. The coupled modes differ from the original modes and can be intuitively understood in terms of the hybrization model [55].

In order to understand the behaviour of these coupled modes, we have studied the optical properties of a dimer consisting of two gold spherical nanoparticles with identical radii $R = 50$ nm. To this end, we have calculated the normalized optical extinction cross-section of different configurations of the dimer system, as well as the corresponding near-field distributions. The dimer is considered to be suspended in vacuum and the gold nanoparticles are characterized by frequency dependent dielectric functions $\varepsilon(\omega)$ taken from the literature [40].

We first explore the non-conductive situation, where there is a separation distance between the edges of the particles and there is no conductivity in the PC. Then, we consider the conductive regime, where a conductive path links both parts of the dimer.

2.1.1 Non-conductive regime: BDP mode

Figure 2.1 a) shows a schematic representation of the structure under consideration: a gold nanoparticle dimer suspended in vacuum and illuminated by a plane wave with linear polarization along the symmetry axis of the system, and wave-vector $\mathbf{k}$, perpendicular to the same

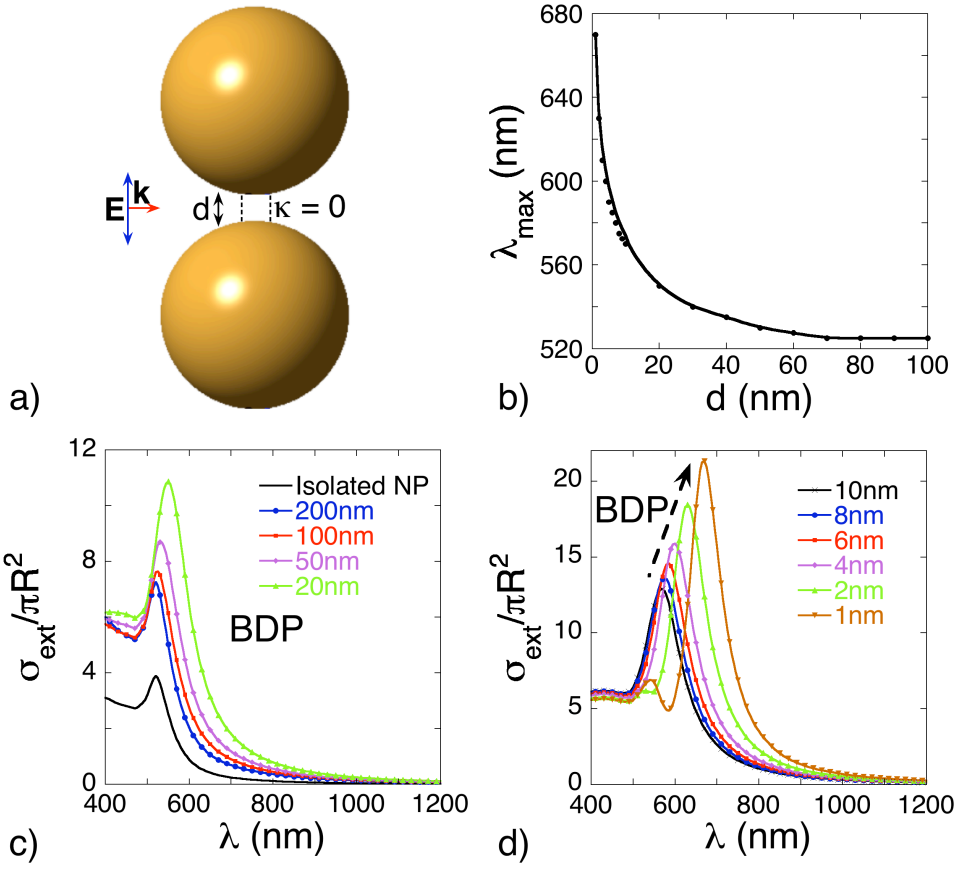

Figure 2.1: a) Schematic representation of a gold nanoparticle dimer with interparticle distance d between the surfaces of the particles. The radius of each particle is $R = 50$ nm and the incident light consists of a plane wave with wave-vector $\mathbf{k}$ and the electric field linearly polarized along the vertical symmetry axis of the system. The dashed lines indicate that there is no conductive path linking both parts of the dimer. b) Shift of the wavelength at which the calculated normalized optical extinction cross-section of the dimer is maximum as d is varied. The points correspond to the calculations in c) and d), while the line is the curve fitting of the points. c) and d) Calculated normalized optical extinction cross-section of the dimer as the interparticle distance d is varied, for long separation distances (c), and for short separation distances (d).

symmetry axis. The surfaces of the gold nanoparticles are separated by an interparticle distance d. The dashed lines included in the schematics indicate that, in the non-conductive regime, there is no conductive path filling the PC formed in the dimer. Once the geometric parameters and the constitutive materials are defined, the interparticle distance d is the parameter governing the evolution of the optical properties of the system, as observed in Figure 2.1 b). This figure shows the shift of the wavelength at which the calculated normalized optical extinction cross-section of the gold dimer is maximum as the interparticle distance d is varied. The points correspond to the calculations, while the line is the curve fitting of the points. As the nanoparticles are closer, forming a cavity between the surfaces of the nanoparticles, a clear red-shift of this maximum is observed, being this shift more pronounced as the separation is reduced. These results are consistent with previously reported studies on the optical response of plasmonic dimers in the nearly-touching and touching regimes [28].

Figure 2.1 b) also shows that the dependence of the shift on the interparticle distance presents an exponential-like behaviour. In the last years, this kind of decay of the plasmon shift of dimers as a function of the interparticle distance has been observed for several systems, such as elliptical and spherical nanoparticles or nanodiscs [72, 73, 74], when the polarization of the incident light is along the interparticle axis, as in this case (see Figure 2.1 a)). In parallel to these studies a plasmon ruler equation, proportional to $e^{-d/2R}$, was successfully proposed to determine the universal dependence of the coupling of plasmons on the interparticle distance [74]. Our results are in good agreement with this scaling decay.

In more detail, in Figures 2.1 c) and d) we observe the normalized optical extinction cross-section of the gold dimer as d is varied. In Figure 2.1 c), the cases with long interparticle distances are plotted, where the nanoparticles are separated by distances longer than several particle radii,

so that the coupling between them is very weak, together with the case of an isolated nanoparticle. We observe that the spectral position of the plasmon resonance of the isolated gold nanoparticle ($d \to \infty$), initially found at $\lambda = 520$ nm, is the same as for the case when the interparticle distance doubles the diameter of the individual particles ($d/2R = 2$). Thus, in this case, there is no coupling between the nanoparticles. As d is decreased, the plasmon resonance is slowly red-shifted towards longer wavelengths. This long-distance non-conductive regime is governed by the single particle bonding dipolar mode. Figure 2.1 d) shows the nearly-touching regime ($d/R < 0.2$), where the distance between the particles is small in comparison to the radius so that coupling between the nanoparticles becomes stronger, and where the increasing red-shift of the mode is observed as the nanoparticles get increasingly closer. Contrary to the case where the interparticle distance is longer, this nearly-touching regime is governed by the BDP mode, arising from the hybridization of the dipolar modes of the individual nanoparticles. For the cases of maximum proximity considered here, where $d = 2.0$ nm, 1.0 nm and 0.5 nm, a blue-shifted mode emergesamarcord72. This higher energy mode is the Bonding Quadrupolar Plasmon (BQP) mode, which arises from the hybridization of the quadrupolar modes of the individual nanoparticles.

In terms of the hybridization picture, the BDP mode is understood as the hybridization of the dipolar modes ($l = 1$) of the individual particles due to the coupling between the nanoparticles [55], as shown in Figure 2.2. Explicitly, the dipolar plasmon modes of the individual nanoparticles couple and form two collective modes: the bonding mode, with lower energy, and the anti-bonding mode, with higher energy. The bonding or BDP mode corresponnds to an electric charge distribution in the dimer which can be interpreted as two parallel dipoles. Thus, the BDP mode has a large dipolar moment and it couples very effectively to the incident light, being the predominant mode ruling the optical properties of

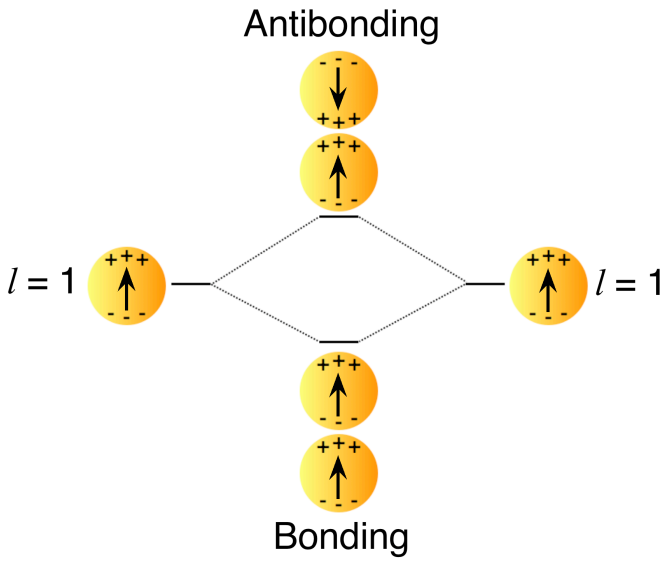

Figure 2.2: Hybridization model for a nanoparticle dimer showing the formation of the BDP mode from the combination of the $l = 1$ modes of the individual particles.

nanoparticle dimers. In contrast, for the anti-bonding mode the electric charge distribution in the dimer corresponds to two anti-parallel dipoles, therefore, it presents no net dipolar moment and it does not couple to light. This kind of mode is usually named as dark mode, contrary to the case of the highly radiative modes, usually referred to as bright modes due to their ability to couple to light. However, the anti-bonding mode can be excited by other means, for example, with an electron beam [75].

Similar to the dipolar modes, the hybridization picture can also be applied to higher order modes. It is the case of the lower energy mode emerging for small interparticle distances in Figure 2.1, which corresponds to the coupling of the quadrupolar modes ($l = 2$) of the individual nanoparticles and appears when the interparticle distance is very small and/or larger particles are considered. In the limit of nearly-touching nanoparticles, the coupling between the dipolar individual modes and

higher order modes occur, forming hybridized modes with mixed character.

All this hybridization of modes is characteristic of dimers illuminated by light with the electric field polarized along the symmetry axis of the system, as considered in this work. When the incident light presents the electric field with polarization perpendicular to the symmetry axis, the particles hardly couple and the mixing of the modes is not observed.

2.1.2 Conductive regime: CTP mode

In order to study the conductive regime, we connect physically the two nanoparticles forming the dimer by a junction modelled as a cylinder with length d and radius a, forming a linker which matches perfectly the spherical nanoparticles. This junction filling the PC opens a conductive path between both parts of the dimer with conductivity $\kappa(\omega)$. The conductivity is related to the dielectric function characterizing the junction by means of Eq. (1.8). Figure 2.3 a) shows a schematic representation of the structure under consideration: a gold nanoparticle dimer suspended in vacuum and illuminated by a plane wave with wave-vector $\mathbf{k}$ perpendicular to the symmetry axis of the system and with the electric field linearly polarized along the same symmetry axis.

In the conductive case, once the geometric parameters and the constitutive materials are defined, the radius a is the parameter governing the evolution of the optical properties of the system, as shown in Figure 2.3 b). We display the normalized optical extinction cross-section, over a large wavelength scale, of a gold dimer for different radii a of the junction, for a small distance between the surfaces of the particles $d = 1$ nm, so that the structure is highly coupled. Contrary to the non-conductive case, the BDP mode blue-shifts as the radius of the conductive path is wider. This blue-shift has been previously reported in touching dimers, where the conductive path is open by overlapping the particles [28, 76].

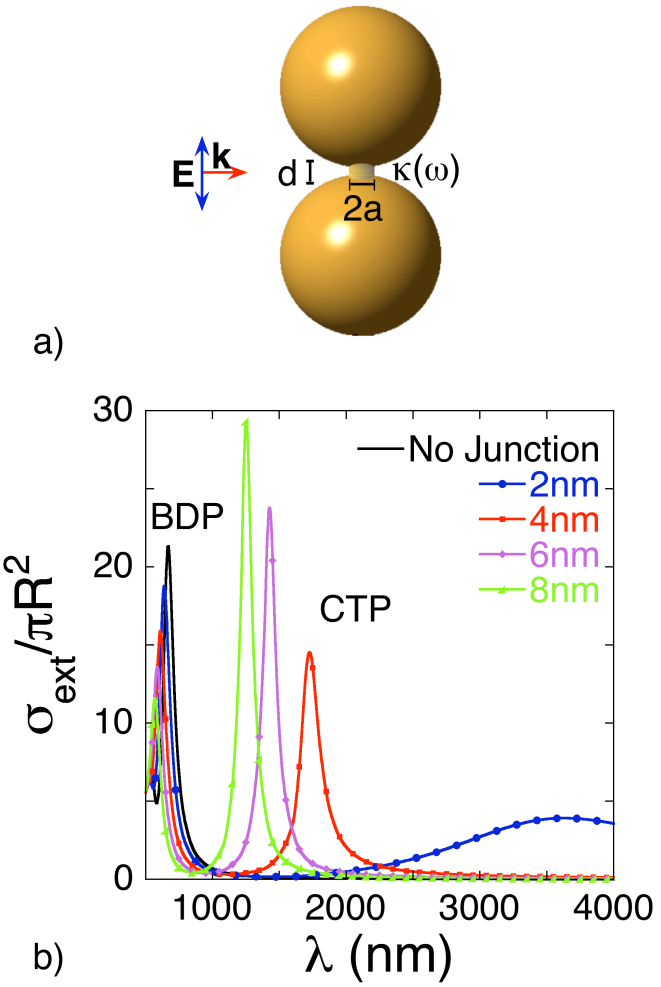

Figure 2.3: a) Schematic representation of a gold dimer with a conductive path connecting both nanoparticles. The interparticle distance between the surfaces of the particles is d, and a is the radius of the gold junction linking both parts of the dimer. The radius of each particle is $R = 50$ nm and the incident light is a plane wave with the electric field polarized along the vertical symmetry axis of the system. The gold junction opens up a conductive path between both parts of the dimer with conductivity $\kappa(\omega)$ b) Calculated normalized optical extinction cross-section, over a large wavelength scale, of a conductively connected dimer as the radius a of the junction is varied. The blue-shift of the BDP mode and the emergence of the CTP mode are observed.

A new mode at very long wavelegths emerges in the Near-InfraRed (NIR) range of the spectrum, also blue-shifting as the conductive path becomes wider and consistent with previous results in overlapping particles. This lower-energy mode is the so-called CTP mode and it has also been observed when both parts of a dimer overlap [28, 76].

The CTP mode can also be understood with the help of the hybridization picture, as illustrated in Figure 2.4. In this case, the CTP mode arises from the hybridization of the monopolar modes of the individual nanoparticles, resulting in a dipolar mode when considering the structure as a whole. The charge transfer through the conductive path allows the charge neutrality of the entire system, even though each individual nanoparticule present net charge of opposite sign. Note, that the monopolar modes for the individual nanoparticles are not real modes since, for the isolated nanoparticles, the principle of charge neutrality needs to be fulfilled.

In the conductive case, it is worth pointing out that, for the material forming the dimer and the junction with conductivity κ, the radius a governs the conductance of the conductive path. In previous studies on the emergence of the CTP [28, 76], there has not been an explicit study on the dependence on the conductance properties of the junction linking the dimer. Thus, in the following chapters, we develop a study on the optical properties of the BDP and CTP modes in the conductive regime and on how these optical properties are affected by the conductance of the conductive path of the dimer.

2.2 Near-field distributions

In order to complete the introduction of the BDP and the CTP modes, we address now their near-field distributions. Two particular cases have been chosen: the BDP mode in the non-conductive regime when the sys-

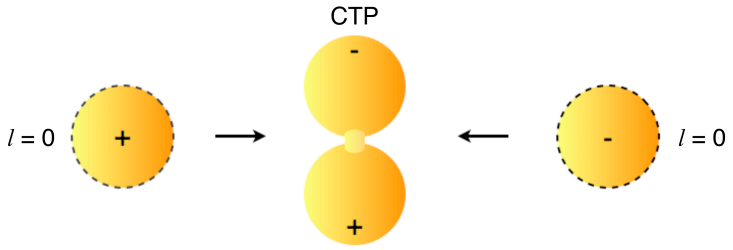

Figure 2.4: Model of the CTP mode understood as the hybridization of the monopolar modes ($l = 0$) of the individual nanoparticles. The black dashed lines indicate that the monopolar modes do not really exist for individual nanoparticles.

tem is highly coupled, and the CTP mode in the conductive regime with the same coupling strength. These near-field distributions are shown in Figure 2.5, where the modulus of the electric field is represented with a surface plot.

Figure 2.5 a) shows the surface plot of the modulus of the electric field for the BDP mode in the non-conductive regime when the interparticle distance is $d = 2$ nm, calculated at $\lambda = 630$ nm. The field is largely enhanced in the interparticle gap, showing a clear "hot-spot", due to the concentration of charges of opposite sign on the surfaces of both sides of the PC. Thus, the capacitance of the cavity is very large. This ability of the BDP mode of adjacent nanoparticles to focus light is very promising for Surfance Enhanced Raman Scattering (SERS) applications [77].

Figure 2.5 b) shows the surface plot of the modulus of the electric field for the CTP mode in the conductive regime where the interparticle distance is $d = 1$ nm and the radius of the linker is $a = 8$ nm, calculated at $\lambda = 1250$ nm. Contrary to the BDP, the electric field is not concentrated in the cavity since the charge transfer through the conductive path considerably diminishes the capacitance in the junction, allowing for the redistribution of the charge along the whole dimer. Thus, the field is

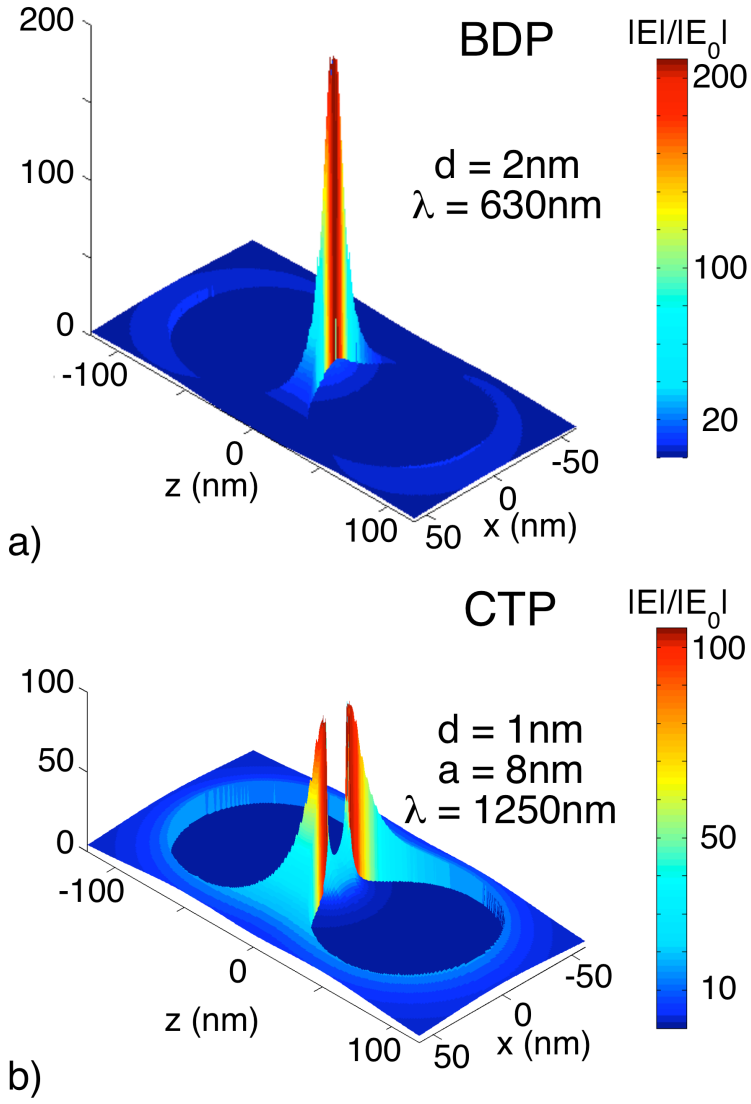

Figure 2.5: Surface plots showing the near-field distributions for the BDP and CTP modes of gold dimers in the $y = 0$ plane. The incident light consists of a plane wave with wave-vector along the x axis and the electric field linearly polarized along the z axis (see Figures 2.1 a) and 2.3 a)). a) BDP mode in the non-conductive regime when the interparticle distance is $d = 2$ nm, calculated at $\lambda = 630$ nm. b) CTP mode in the conductive regime when the interparticle distance is $d = 1$ nm and the radius of the linker is $a = 8$ nm, calculated at $\lambda = 1250$ nm.

expelled from the filled gap in this situation. We also observe that the field is homogeneously distributed all around the dimer, since the electric charge is not concentrated in the cavity, in contrast to the case of the BDP mode.

2.3 Summary

In this chapter we have introduced the two main resonances governing the optical response of highly coupled plasmonic dimers. When there is no conductive path between nanoparticles forming the dimer, the BDP mode is responsible for the spectral features. The BDP mode arises from the hybridization of the dipolar modes ($l = 1$) of the individual nanoparticles and presents huge field enhancement of the electric field and large capacitance in the cavity between the particles. When there is a conductive path linking both nanoparticles, the CTP mode emerges for long wavelength values. The CTP mode is understood as the hybridization of the monopolar modes ($l = 0$) of the individual particles (forbidden when there is no connection). For the CTP the local electric field around the nanoparticles presents a more homogeneous distribution, in comparison to the BDP. The field in this case is expelled from the linked region due to the reduced capacitance of the cavity, or its total suppression.

CHAPTER 3

ELECTRON TRANSPORT EFFECTS AND OPTICAL PLASMONIC SPECTROSCOPY

It has been recently shown, both experimentally and theoretically, that when two nanoparticles are very closely spaced, so that a conductive overlap between them is established, the associated optical spectra and local field enhancements can be dramatically modified [28, 29, 31, 76, 78, 79, 80, 81]. In addition to the Bonding Dimer Plasmon (BDP) mode, which is the main optical feature of close particles, we have already introduced in Chapter 2 that when a conduction path between the two parts of the dimer is opened, a Charge Transfer Plasmon (CTP) mode, involving charge transfer across the junction, emerges as an optical feature. Theoretical simulations showed that the energy of the CTP mode depends strongly on the touching profile [28]. This geometrical dependence is connected with the conductance established through the junction between the two particles. However, no explicit study had been performed on the dependance of the CTP on the conductance through the overlap between the two particles of the dimer.

In this chapter, we present a theoretical study of the optical prop-

erties of a Plasmonic Conductive Cavity (PCC) consisting of a strongly coupled (non-touching) nanoparticle dimer connected by a conductive bridge, focusing on the spectral signature of the system in relation to the conductance through the junction between the nanoparticles. This system can be viewed as a simple model of two nanoparticles linked by an ensemble of conductive molecules. In the following, we show how strongly the optical properties of the PCC depend on the conductance of the bridge.

3.1 Optical response of a conductive linker

Shape and size of the constituents are two key ingredients in the study of plasmonic systems. We therefore define the geometry of our system in the schematics in Figure 3.1 a). We consider an heterogeneous nanostructure composed of two nanoshells, acting as electrodes, with silica cores of radius $R_{int} = 45$ nm covered by gold shells of radius $R = 55$ nm, namely, the thickness of the gold shells is 10 nm. The conductive linker connecting the dimer is modelled as a solid cylinder perfectly matching the spherical shape of the electrodes. The linker is characterized by two parameters: the radius a and the length d, defined as the shortest interparticle distance between the nanoshells. In this study we consider the interparticle distance to be $d = 1$nm, so that the nanoshells are strongly coupled. The incident light is a plane wave with the electric field linearly polarized along the symmetry axis of the system and wave vector $\mathbf{k}$ perpendicular to the same symmetry axis.

The surrounding medium is another key feature influencing the plasmonic properties. In our case, the dimer is assumed to be suspended in vacuum and the materials composing the different parts of the system are characterized by local dielectric functions, $\varepsilon(\omega)$, taken from the literature, both for gold [40] and silica [39]. For the sake of simplicity, we have

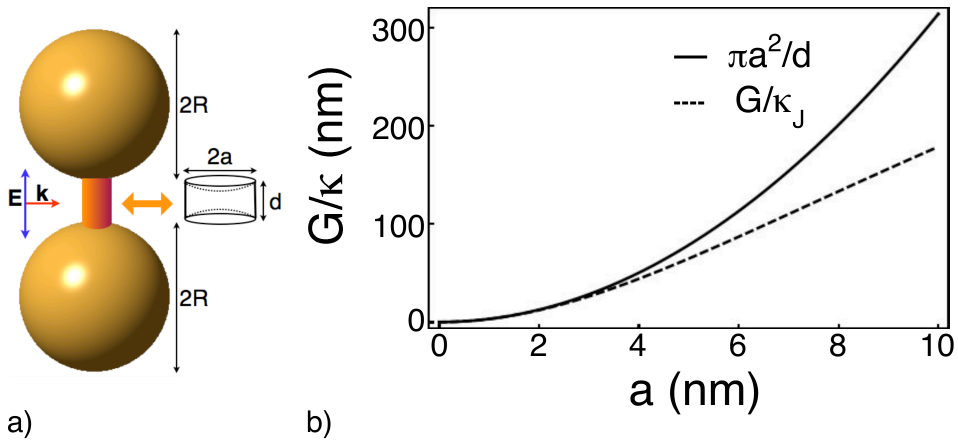

Figure 3.1: a) Schematic representation of a nanoparticle dimer connected by a cylindrical linker. The linker is zoomed so that its concave endings and geometrical parameters, radius a and length d, can be clearly appreciated ($d = 1$ nm and $R = 55$ nm). The incident light is a plane wave with linear polarization along the symmetry axis of the system and wave vector $\mathbf{k}$ is perpendicular to the same symmetry axis. b) Ratio conductance/conductivity for a perfect conductive cylinder with planar endings, where $G/\kappa = \pi a^2/d$ (solid line), and for a conductive linker with curved endings (dashed line), where the G/κ_J is given by Eq. (3.2).

first modelled the conductive linker as a pure conductor characterised by a DC conductivity κ_J, so that the corresponding frequency-dependent dielectric function $\varepsilon(\omega)$ can be expressed as:

$$\varepsilon(\omega) = 1 + i\frac{4\pi\kappa_J}{\omega}. \tag{3.1}$$

The conductivity of the linker κ_J is then related to its conductance G through geometric parameters. In our case, the consideration of the spherical connection between the linker and the particles leads to a mathematical expression for the ratio G/κ_J involving the parameters a, R and

d:

$$\frac{G}{\kappa_J} = \frac{G}{\kappa_J}(a, R, d) = \pi\Big\{\sqrt{R^2 - a^2} - R + (d/2 + R)\ln\left[1 + 2(R - \sqrt{R^2 - a^2})/d\right]\Big\}, \tag{3.2}$$

where R is the external radius of the nanoshell, a is the radius of the linker and d is the interparticle distance. In the limit of very thin linkers, $a << d$, the function $G/\kappa_J(a, R, d)$ (Eq. (3.2)) behaves as a conductive cylindrical wire with planar endings, and the expression becomes:

$$\lim_{a \ll d,R} \frac{G}{\kappa_J} = \frac{\pi a^2}{d}. \tag{3.3}$$

We should notice that the real part of $\varepsilon(\omega)$ is frequency independent (see Eq. (3.1)), since we have assumed the linker to be a pure conductor. In contrast, the imaginary contribution, which is related to energy losses, is the only part of the dielectric function affected by any possible change in the parameters. These changes in the imaginary part of $\varepsilon(\omega)$ can be related to the variation of DC conductivity κ_J, which is governed by variations in the geometry, variations in the conductance or a combination of both. Whereas in the limit of very thin linkers the conductance has a quadratic dependence with the radius of the linker, as shown in Eq. (3.3), a nearly linear trend is obtained in Eq. (3.2) when thicker linkers are considered. We can observe in Figure 3.1 b) that this implies that G/κ_J hass always smaller values than those given by the function of a wire, due to the effect of the curvature of the nanoshells. For the interparticle distance considered in the present work, $d = 1$nm, this implies a quadratic behaviour of G/κ_J up to radius $a \simeq 3$ nm, as appreciated in Figure 3.1.

In order to connect with the terminology for molecular conductances, we will vary κ_J so that the total conductance of the linker is equal to an integer number n of quantum units of conductance G_0, *i.e.*, $G = nG_0$, where $G_0 = 2e^2/h \approx 77.5\mu$S.

3.2 Optical signature of the BDP and CTP modes

We show the evolution of the calculated normalized optical extinction cross-section of the PCC in Figure 3.2 a) over a large wavelength scale as a function of the conductance through the junction. The peak around $\lambda \approx 840$ nm, also present when there is no junction linking the particles, is the hybridized dipolar BDP mode resulting from the capacitive coupling of the dipolar plasmon modes of the individual nanoshells [55], introduced in section 2.1.1. As the conductance of the junction is increased, the BDP mode blue-shifts and its width changes. For the largest conductance, a new plasmon mode, highly red-shifted and damped, appears around $\lambda \approx 2940$ nm. This emerging resonance is the CTP mode where, the net charge of the individual nanoshells will oscillate in time across the junction.

Figure 3.2 b) shows the local electric field distributions inside the junction and its surroundings for some of the plasmon resonances in Figure 3.2 a). When low conductance is considered, $G = 5G_0$ in the top panel, the electric field is still maximum at the junction, similarly to the case of an empty junction, allowing a significant capacitive coupling between the two nanoparticles. As the conductance is gradually increased, the local field is progressively expelled from the junction, reducing the capacitive coupling across the cavity. For intermediate values of conductance, $G = 62G_0$ in the central panel, it can clearly be observed that the local field across the molecular bridge has decreased dramatically. In this case, the capacitive coupling between the two nanoshells is reduced, resulting in a slight blue-shift of the BDP. We will refer to this blue-shifted BDP as the Screened BDP (SBDP) mode. The bottom panel shows the field distribution of the CTP mode for large conductance, $G = 1053G_0$, clearly revealing that the electric field outside the molecular bridge is also

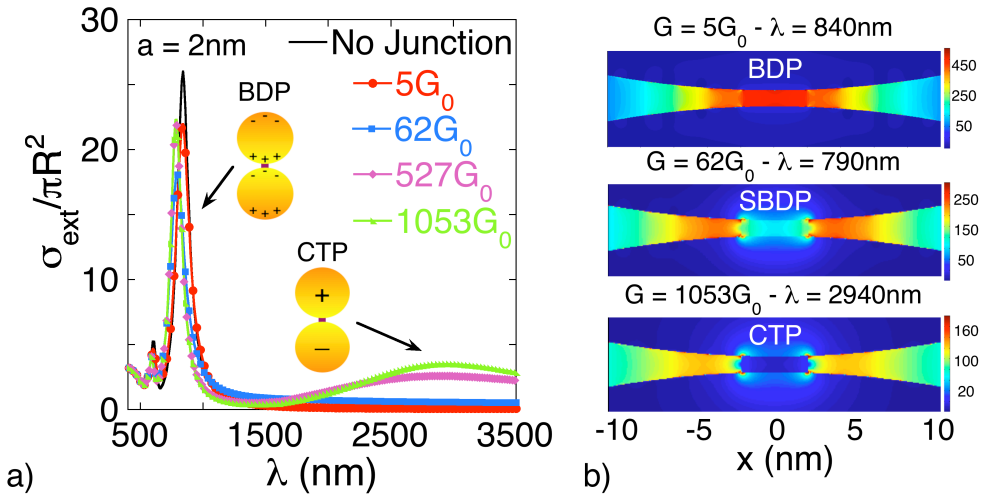

Figure 3.2: a) Calculated normalized optical extinction cross-section of a PCC with $a = 2$ nm as a function of conductance. Insets illustrate the charge distributions of the BDP and the CTP modes. b) Near-field distributions for some of the resonance wavelengths in a): BDP at $\lambda = 840$ nm (top), SBDP at $\lambda = 790$ nm (middle) and CTP at $\lambda = 2940$ nm (bottom).

strongly reduced and that inside the junction the field has been expelled. In this limit, the conductive junction acts as a short circuit, drastically reducing the potential difference between the two nanoparticles.

Now, we address in more detail the tendencies of the spectral features and near-field distributions of both the BDP and the CTP modes as optical fingerprints of the conductance of the junction. We consider separately two regimes in the next two subsections: the small and large conductance regimes.

3.2.1 Small conductance regime: from BDP to SBDP mode

Figure 3.3 shows the calculated normalized optical extinction cross-section of the PCC in the region of the spectrum around the BDP as the

conductance is increased for three different radii of the linker. For small values of the conductance, the energy of the BDP remains unaltered, with a monotonic increase in its linewidth with increasing conductance. For intermediate conductance, the BDP blue-shifts and the SBDP mode is formed. As the conductance becomes larger, the energy of the SBDP remains unchanged but its linewidth decreases. This behavior is found systematically for the three different sizes of the conductive junctions we have considered in Figures 3.3 a), b) and c), where $a = 1$ nm, 2 nm and 3 nm, respectively.

Figure 3.4 a) shows how the linewidth of the SBDP (Full Width at Half Maximum (FWHM)) depends on the conductivity of the junction κ_J for different sizes of the junction, with the conductivity of the junction is expressed in units of the conductivity of gold. This linewidth dependence on the conductance can be qualitatively understood in terms of the simple resistor model depicted in Figure 3.5 a), where the PCC is modelled as a serial combination of resistors, r_{Au} for the gold particles and $r_{junction}$ for the junction. The power dissipated in the junction W_J, when a potential V is applied, is calculated using Joule's law:

$$W_J = I^2 r_J = \frac{V^2 r_J}{(2r_{Au} + r_J)^2}, \tag{3.4}$$

where I is the electric current in our model circuit. For low junction conductance ($r_J >> r_{Au}$), the dissipation in the junction scales as $W_J \propto 1/r_J \propto \kappa_J \propto G$. In the low conductance limit, the dissipation in the junction and, hence the broadening of the SBDP, increases linearly with the conductivity of the junction κ_J and, thus with the conductance G. On the contrary, for large junction conductance ($r_J << r_{Au}$), the dissipation in the junction scales as $W_J \propto r_J \propto 1/\kappa_J \propto 1/G$, i.e., a further increase of junction conductivity κ_J, and consequently an increase of the conductance G, produces a decrease of the dissipation and hence, a reduction in the linewidth.

Figure 3.4 b) shows that the magnitude of the blue-shift increases

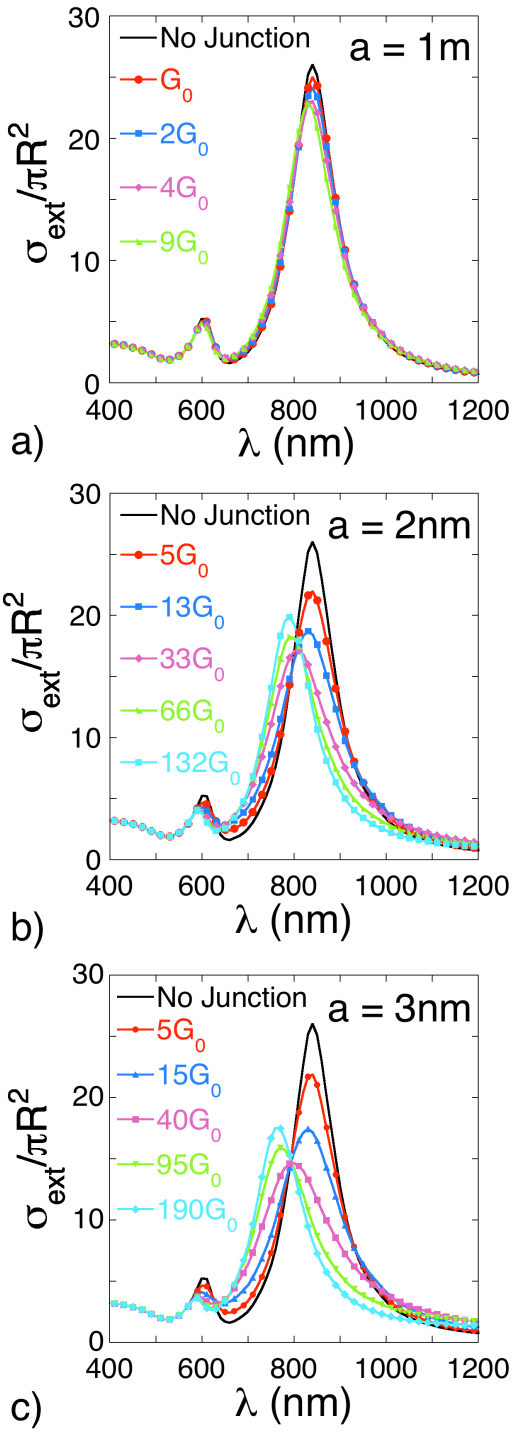

Figure 3.3: Calculated normalized optical extinction cross-section of a PCC as a function of conductance for different radii of the linker: a) $a = 1$ nm, b) $a = 2$ nm and c) $a = 3$ nm.

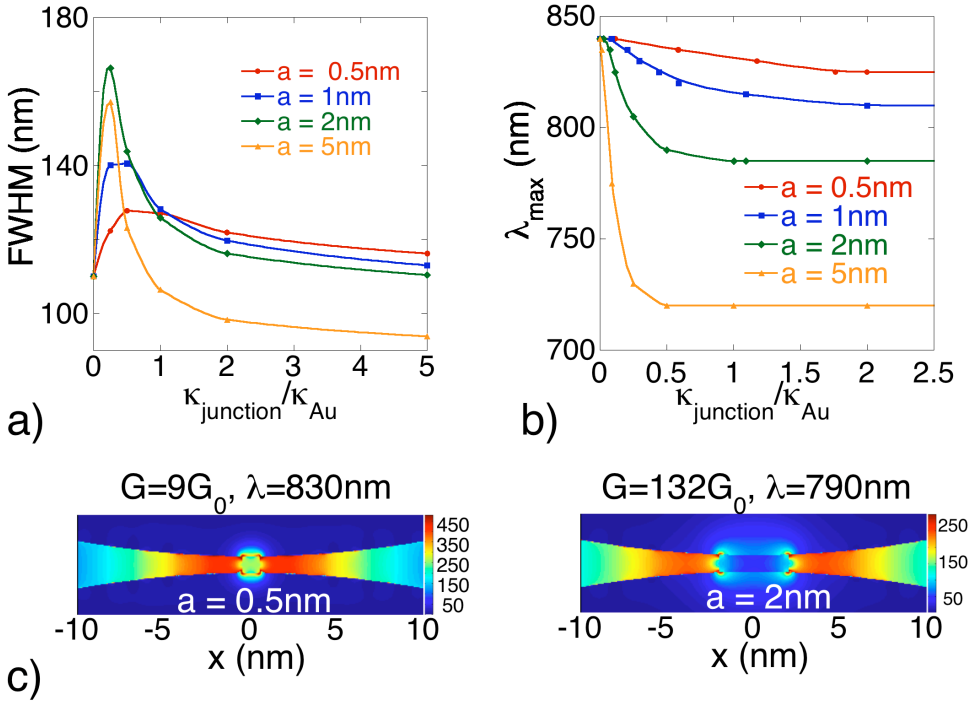

Figure 3.4: a) Evolution of the linewidth and b) blue-shift of the BDP as a function of conductivity for different radii of the PCC. c) Near-field distributions of the SBDP mode for $a = 0.5$ nm (*Left*) and $a = 2$ nm (*Right*).

with the increase of the radius a. In the absence of linker, a large Coulomb attraction between the two nearby sides of nanoparticles is present for the BDP mode, as illustrated in the top schematic plot of Figure 3.5 b). Once the SBDP mode has been formed, as illustrated in the bottom schematic plot, the Coulomb attraction is reduced, since the surface charge facing the junction is screened. This decrease in the capacitive coupling with increasing a can also be inferred from the near-field distributions in Figure 3.4 c), which show that wider junctions screen more surface charge, resulting in lower field enhancements in comparison to narrower junctions.

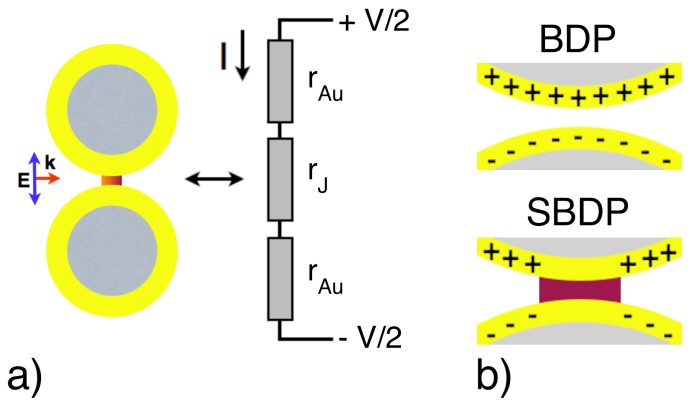

Figure 3.5: a) Resistor model describing the screening of the PCC. Each nanoparticle is represented by a resistor r_{Au}, and the conductive bridge by r_J. The voltage from the incident field is V. b) Schematic representation of the PCC illustrating the reduction of the capacitive coupling through the junction, which leads to the formation of the SBDP (bottom) from the BDP (top), as the conductance through the junction increases.

3.2.2 Large conductance regime: emergence of the CTP mode

In order to explore the spectral features of the CTP mode, Figures 3.6 a) and b) show the normalized optical extinction cross section as the conductance across the junction is dramatically increased for two different radii of the junction. In this limit, the dimer acts as a single nanostructure, rather than a coupled pair of nanoparticles. The plasmon frequencies in the large conductance regime remain fixed for the same geometry. The geometrical dependence is clearly observed in Figure 3.6 a), which shows a strong red-shift of the CTP mode for the narrow junction. Figures 3.6 a) and b) also show a significant decrease of the linewidth of the CTP mode as conductance is increased. This behaviour can be understood in terms of the reduced dissipation for large conductance, in agreement with the predictions of the simple resistor model, already

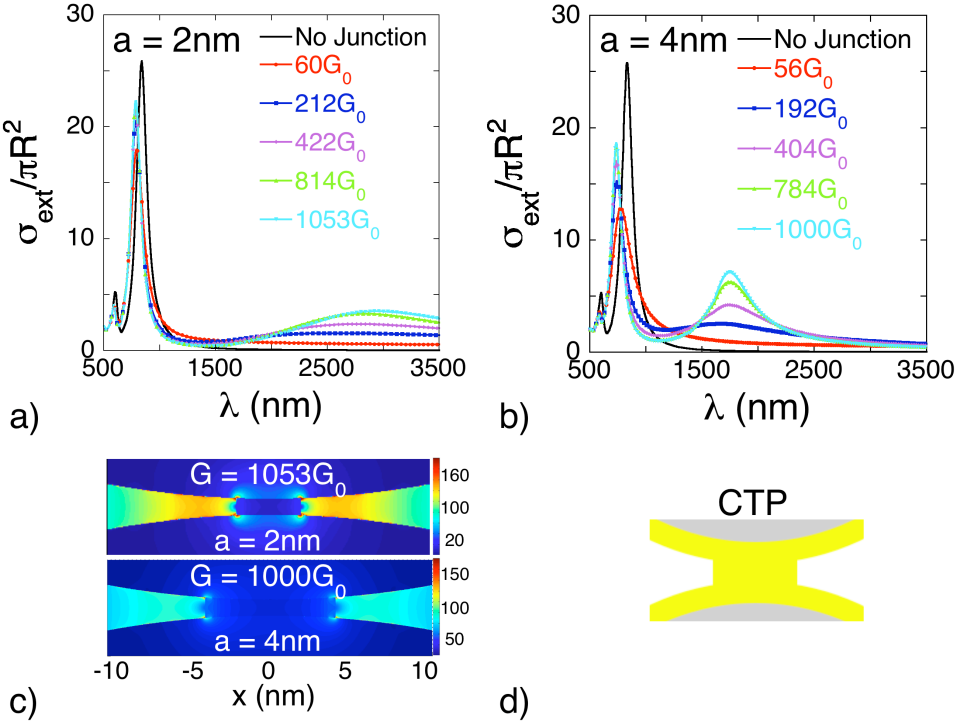

Figure 3.6: Calculated normalized optical extinction cross section of a PCC as a function of conductance for different radii of the junction. a) $a = 2$ nm and b) $a = 4$ nm. c) Near-field distributions for some of the resonances in a) and b): Top - $a = 2$ nm, $G = 1053G_0$, $\lambda = 2940$ nm and bottom - $a = 4$ nm, $G = 1000G_0$, $\lambda = 1750$ nm. d) Schematic representation of the PCC illustrating the reduction of the capacitive coupling through the junction for the CTP mode.

introduced to explain the linewidth dependance of the BDP mode (see Eq. (3.4)).

Figure 3.6 c) shows the near-field distributions associated to two of the spectra in a) and b). In particular, the near-field inside the junction and its surroundings is shown for two linkers with radii $a = 2$ nm and $a = 4$ nm in the large conductance regime. We observe that the field has been expelled from the PCC reducing the Coulomb attraction between the shells. This situation corresponds to the schematic plot shown in Figure 3.6 d).

3.2.3 Near-field distribution of the SBDP and CTP modes. Effect of the skin-depth.

The nature of the plasmon modes can be illustrated by observing the near-field associated to the resonances. For the nanoparticle dimer linked by a conductive junction, we have already shown in this section that the electric field is progressively expelled from the junction as the conductance is increased. For low conductance values the junction still acts as a perfect capacitive cavity, whereas for values of the conductance larger than a certain threshold value G_{SBDP}, the Coulomb attraction between the gold shells and the capacitance of the cavity is reduced, therefore the local field is progressively expelled from this region. An estimation of this threshold value of the conductance is derived in the next section. This decrease of the electric field in the PCC can be clearly observed in Figure 3.7, where the modulus of the near-field is represented in the plane defined by the propagating vector $\mathbf{k}$ of the incident plane wave and the axis of polarization of the electric field $\mathbf{E}$ (see schematics in Figure 3.7).

In order to observe the different charge distribution of the SBDP and CTP resonances, we compare the near-field distributions of these two modes also in Figure 3.7, where a conductive junction with radius

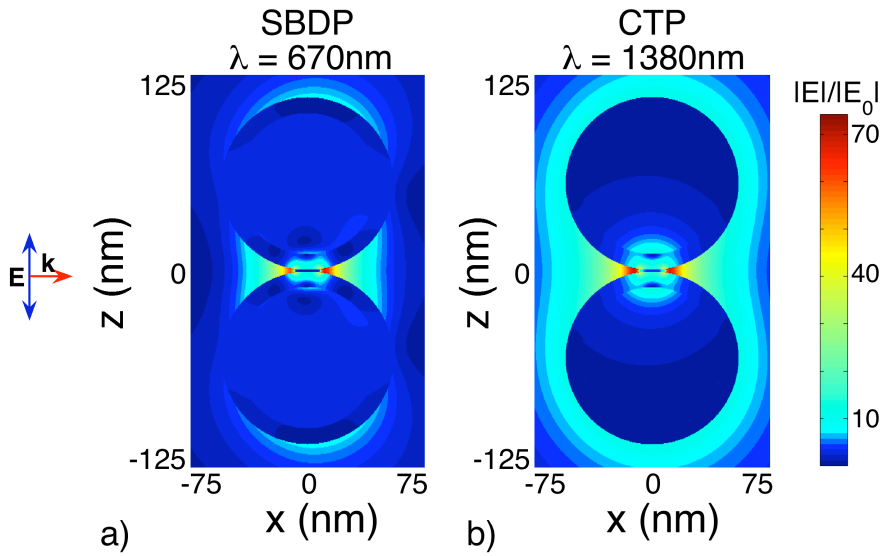

Figure 3.7: Near-field distribution of the SBDP and CTP modes for a nanoshell dimer linked by a conductive junction with radius $a = 8$ nm, conductivity $\kappa_J = 5\kappa_{Au}$ and conductance $G = 7229G_0$: a) SBDP at $\lambda = 670$ nm and b) CTP at $\lambda = 1380$ nm.

$a = 8$ nm and conductance $G = 7229G_0$ is considered: Figure 3.7 a) corresponds to the SBDP resonance at $\lambda = 670$ nm, and Figure 3.7 b) corresponds to the CTP resonance at $\lambda = 1380$ nm. In both cases, the local field is expelled from the junction and the near-field takes its highest values around the molecular junction, but some differences can be observed. For the SBDP mode, the distribution of the field corresponds to a dipole-dipole pattern, in connection with the BDP distribution. In this case, the surface charge is highly localized at the cavity, with charge of opposite sign at both sides of the cavity, observing dipolar electric field distributions and fulfilling charge neutrality in each nanoparticle, separately. In contrast, for the CTP mode, the near-field distribution has a quite uniform intensity distribution all around the dimer (see Figure 3.7 b), in agreement with the near-field patterns obtained for interpenetrat-

ing particles [28]. In this case, charge neutrality is fulfilled for the whole nanostructure, but each side of the dimer presents net-charge.

In relation to this behaviour of the electric field and, observing in Figure 3.7 its penetration into the gold shells, one can try to establish a connection between the reduction of the field and the skin depth. The skin depth δ is the parameter describing the ability of the electromagnetic field to penetrate into a material. In SI units this parameter is given by [82]:

$$\delta = \sqrt{\frac{2}{\mu_0 \omega \kappa}}, \tag{3.5}$$

where μ_0 is the magnetic permeability of free space, ω is the frequency of the incident field and κ is the DC conductivity. If we analyze the skin depth for the cases considered in Figure 3.7, where $\kappa = \kappa_J = 5\kappa_{Au}$ and its corresponding conductance $G = 7229G_0$, we obtain values of $\delta_{SBDP}(\lambda = 670 \text{ nm}) \approx 12$ nm for the SBDP mode and $\delta_{CTP}(\lambda = 1625$ nm) ≈ 17 nm for the CTP mode. These values of the skin depth are of the order of the size of the junction in this case, where $a = 8$ nm. However, in most of the situations considered along this chapter, mimicking feasible dimensions of molecular linkers, the conductance at the junction is much smaller. To illustrate better this concept, in Figure 3.8 we show the calculated optical extinction cross-section (a) and the modulus of the near-field in the junction (b), in the plane formed by the propagating vector **k** and the field (b) and along the x axis at the centre of the cavity (c), for a conductive junction with radius $a = 2$ nm. In Figure 3.8 a), the formation of the SBDP mode is observed as the conductance is increased. In this situation, the skin depth is reduced as the conductance increases, taking the following values: $G = 5G_0$ - $\delta(\lambda = 840 \text{ nm}) \approx 149$ nm, $G = 33G_0$ - $\delta(\lambda = 810 \text{ nm}) \approx 57$ nm and $G = 132G_0$ - $\delta(\lambda = 790$ nm)≈ 28 nm. These values of the skin depth are much larger than the dimensions of the nanometric junction. Thus, the skin depth allows the penetration of the field into the conductive junction. However, it is clear

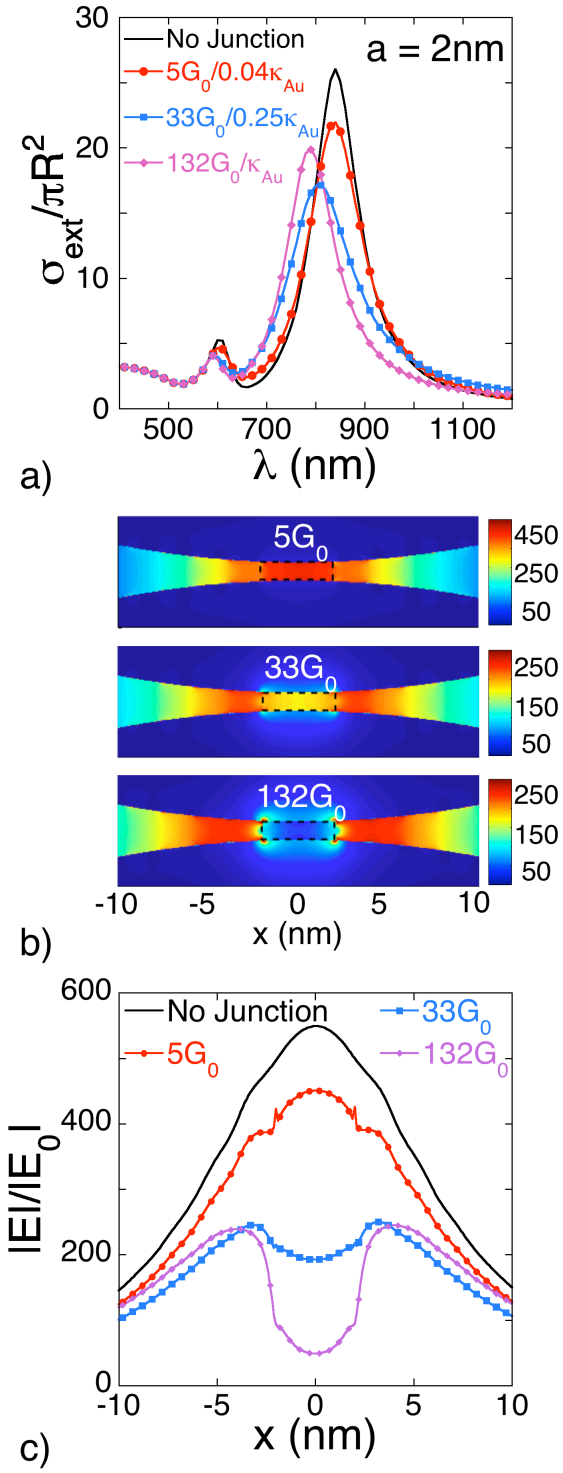

Figure 3.8: a) Calculated optical extinction cross-section for a nanoshell nanoparticle dimer linked by a conductive junction with radius $a = 2$ nm as the conductance G is increased. b) Near-field patterns inside the junction and its surroundings where the progressive expulsion of the field from the PCC is evident as conductance is increased. The space occupied by the junction is indicated by a rectangular shape plotted with a dashed black line. c) Modulus of the near-field inside the junction and its surroundings along the axis of propagation of the incident plane wave.

from Figures 3.8 b) and c) that the field is progressively reduced, even for small values of G. For all the above, one can conclude that it is the intrinsic nature of the conductance for the BDP and CTP modes in relation to the dimer the key aspect determining the spectral features of the system rather than the skin depth.

3.3 Connection between electronic transport processes and optical properties: time-scale approach

Both the SBDP and CTP plasmon modes involve oscillatory charge transport across the junction. To establish the connection between electronic transport and optical processes, we relate the time of the optical cycle t_{op}, corresponding to each plasmon resonances ω_{BDP} and ω_{CTP}, to the time of transport t_e of the electrons through the PCC, which is related to the conductivity. Before establishing the analytical connection between both aspects, it is helpful to illustrate the meaning of the excitation of resonant plasmonic modes, as shown in Figure 3.9. These schematics show that, for a complete optical cycle, the plasmon involves a full oscillation of the charge in a time period of t_{BDP}. More explicitly, if we consider, for instance, the BDP mode in Figure 3.9 a), we can establish a time $t = 0$ and the evolution of the charge density along the cycle. As a consequence of an external harmonic electric field, the electric charge density forms the BDP pattern which can be visualized at a time $t = t_{BDP}/4$. Then, the charge density continues its oscillation with reverse charge pattern in $t = 3t_{BDP}/4$. Finally, the dimer recovers the initial situation after the whole optical cycle $T = t_{BDP}$. If the electrons cannot move as fast as at least $1/4$ of this t_{BDP}, the charge transfer be-

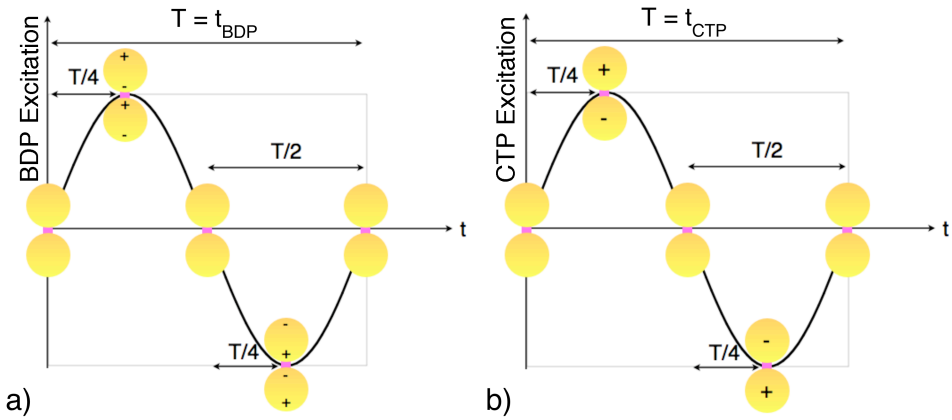

Figure 3.9: Schematic representation of the electric charge distributions of the BDP (a) and CTP (b) modes along an optical cycle T.

tween the cavities will not occur. Any transfer of charge through the cavity thus involve transport times which need to be faster than about 1/4 of the optical cycle, i.e., certain minimum conductance values as we describe in the following.

3.3.1 Conductance threshold for the BDP mode

As illustrated in Figure 3.5 b), the creation of the SBDP mode takes place when the junction allows electron transfer to occur fast enough as to neutralize partially the surface charge on the surfaces. In order to estimate the magnitude of the charge that needs to be transported in each cycle so that the SBDP mode starts evolving, we relate the optical time of the BDP mode t_{BDP} to the transport time of the electrons moving through the junction τ_{BDP}. The optical cycle time is given by:

$$t_{BDP} = \frac{2\pi}{\omega_{BDP}}. \tag{3.6}$$

The transport time is related to the charge and the current intensity through the junction as:

$$\tau_{BDP} = \frac{Q_{BDP}}{I}, \tag{3.7}$$

where Q_{BDP} is the electric charge associated with the BDP mode and I is the electric current. To estimate Q_{BDP} we note that, for the BDP mode, the electric field enhancement η in the junction is given by [83]:

$$\eta = \frac{2R + d}{d}, \tag{3.8}$$

and the local electric field in the junction is then given by:

$$E^{loc} = \frac{2R + d}{d} E^{ext}, \tag{3.9}$$

where E^{ext} is the external electric field. Since $d << 2R$, we can assume that:

$$E^{loc} = \frac{2R}{d} E^{ext}. \tag{3.10}$$

This local electric field corresponds to the surface charge density of the BDP mode σ_{BDP}:

$$\sigma_{BDP} = \frac{E^{loc}}{4\pi}. \tag{3.11}$$

For small junctions, as the ones considered in the present study, one can assume the surface charge density to be constant across the junction, resulting in a total charge given by:

$$Q_{BDP} = \pi a^2 \sigma_{BDP} = \pi a^2 \frac{E^{loc}}{4\pi}, \tag{3.12}$$

where Q_{BDP} is the total electric charge to be screened through the junction in each cycle. To estimate I, we take into account that the conductance of a wire can be easily related to the electric current via the current density j:

$$G = \kappa_J \frac{\pi a^2}{d} = \frac{j}{E^{loc}} \frac{\pi a^2}{d} = \frac{I}{E^{loc} d}. \tag{3.13}$$

Thus, the electric current through the junction is:

$$I = GE^{loc}d, \tag{3.14}$$

and finally, the time for this electron transport process is given by:

$$\tau_{BDP} = \frac{Q_{BDP}}{I} = \frac{a^2}{4Gd}. \tag{3.15}$$

For the SBDP to be formed, the time of electron transport must be shorter than about 1/4 of an optical cycle, as introduced in the previous section. The time of electron transport must fulfill:

$$\tau_{BDP} = \frac{a^2}{4Gd} \leq \frac{\pi}{2\omega_{BDP}}. \tag{3.16}$$

We thus obtain the threshold of conductance G_{SBDP} for the SBDP to start getting screened,

$$G_{SBDP} \geq \frac{\omega_{BDP}}{2\pi}\frac{a^2}{d}. \tag{3.17}$$

As discussed above and shown by Eq. (3.17), the formation of the SBDP mode depends on the geometry of the junction. This equation shows that, once the interparticle distance is fixed, wider junctions need larger conductance to develop the SBDP from the BDP mode, as already discussed in Figure 3.3. To test the validity of this estimation, Figure 3.10 shows the initial shift of the BDP with increasing conductance for different radii of the conductive linker in the low conductivity regime. A systematic trend is observed for all the cases: a range of low conductance where the BDP peak remains at the same spectral position (λ = 840 nm), followed by a blue-shift of the BDP, when the junction allows a conductance larger than G_{SBDP}, thus eventually developing the SBDP. The thresholds of conductance G_{SBDP} provided by Eq. (3.17) are marked with crosses for each radius of the junction in Figure 3.10, corroborating that the blue-shift of the resonance for the different radii occurs exactly for the threshold of conductance given by Eq. (3.17).

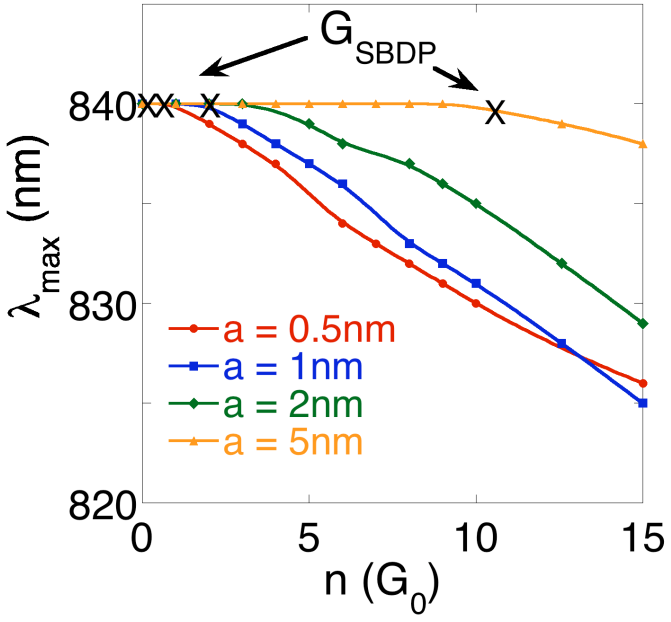

Figure 3.10: Blue-shift of the BDP mode for small values of the conductance. The crosses indicate the threshold values G_{SBDP} of conductance predicted by the time-scale approach (Eq. 3.17).

3.3.2 Conductance threshold for the CTP mode

Similar arguments can be applied to understand the conductance required to sustain the CTP mode. The CTP is fully formed, the electric charge is distributed in both nanoparticles and the total field across the junction is negligible (see schematic plot included in Figure 3.2 a) and the corresponding near-field distribution in Figure 3.7 b)). The optical cycle time t_{CTP} is in this case:

$$t_{CTP} = \frac{2\pi}{\omega_{CTP}}, \tag{3.18}$$

and the time of the electron transport t_{CTP} is given by:

$$\tau_{CTP} = \frac{Q_{CTP}}{I}. \tag{3.19}$$

In the case of the CTP, the total charge that needs to be transported in each cycle through the junction is:

$$Q_{CTP} = \frac{R_{ext}^2}{4} E^{ext}. \tag{3.20}$$

Since the field inside the junction is negligible, for the CTP the plasmon induced field in the junction is thus given by:

$$E^{loc} = -E^{ext}, \tag{3.21}$$

and the amplitude of the instantaneous local field is $2E^{ext}$. Having these arguments into account, the timescale for this charge transport is:

$$\tau_{CTP} = \frac{Q_{CTP}}{I} = \frac{R_{ext}^2}{4Gd} \frac{E^{ext}}{2E^{ext}}. \tag{3.22}$$

As for the SBDP, the CTP requires τ_{CTP} to be a fraction of the optical cycle time $t_{CTP} = \frac{\pi}{2\omega_{CTP}}$: $t_{CTP} \leq 1/4 t_{CTP}$. This leads to the following expression for the threshold of conductance:

$$G_{CTP} \geq \frac{\omega_{CTP}}{4\pi} \frac{R_{ext}^2}{d}. \tag{3.23}$$

This expression shows that the CTP is related to the conductance of the junction rather than its conductivity and that the CTP requires significantly larger conductances to be formed, in comparison to the SBDP. For the junction in Figure 3.11, with radius $a = 4$ nm, the estimation based on the comparison of time scales gives a threshold value (Eq.(3.23)) of $G_{CTP} \approx 370 G_0$. This result is in excellent agreement with the calculated optical extinction cross-sections, which show the emergence of the CTP mode at $\lambda = 1750$ nm around these values of G.

For the junctions in Figures 3.2 a) and 3.6 a), Eq. (3.23) predicts $G_{CTP} \approx 225 G_0$ and $G_{CTP} \approx 370 G_0$, respectively. These thresholds of conductance are also consistent with the corresponding fully developed CTP modes for $G = 263 G_0$ and $G = 404 G_0$ in those figures.

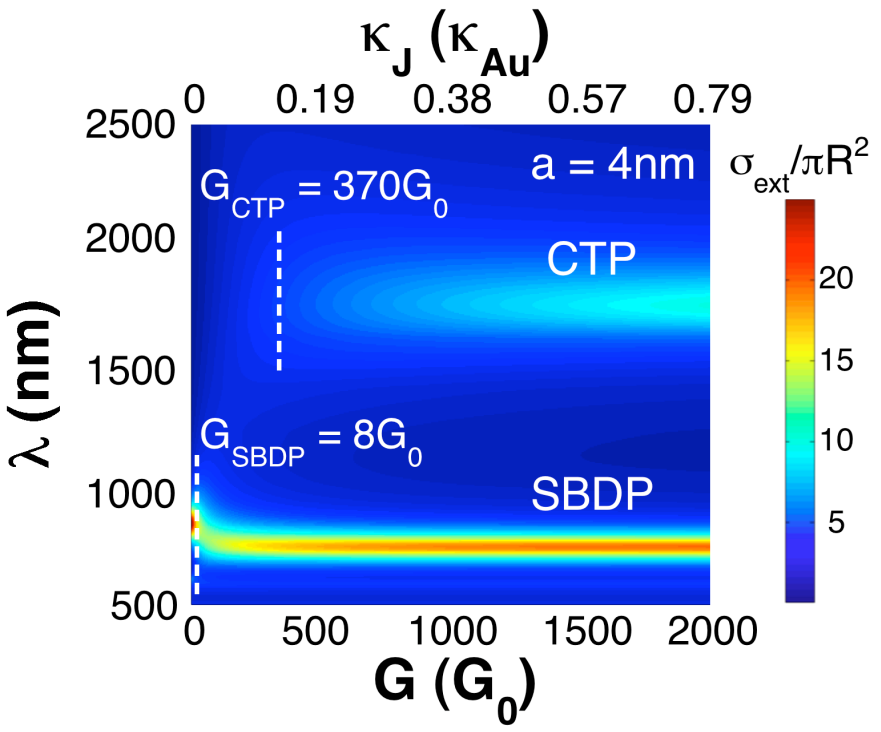

Figure 3.11: Calculated normalized optical extinction cross-section for a junction with radius $a = 4$ nm as conductance is increased. The threshold values of the BDP and CTP modes, $G_{SBDP} = 8G_0$ and $G_{CTP} = 370G_0$, are indicated by white dashed lines.

3.4 Spectral changes due to size and morphological changes in the linker

In the previous sections have we considered a physical situation where we change the material properties of the linker while keeping the geometrical features fixed. Now, in this section we explore the role of the morphology of the conductive linker. To this end, we first consider the effect of changing the size of the junction while its conductivity is fixed, thus a variation of conductance is produced. Second, we study the ge-

ometrical distribution of the current within the junction by varying the morphology of the linker.

3.4.1 Influence of the size of the linker

So far we have only considered the variation of conductance through the junction while its size remains unaltered. This corresponds to a physical situation where we change the nature of the linker while keeping the structural features fixed. We now maintain the conductivity fixed while the radius of the linker is varied, which corresponds to a physical situation where the material linking the nanoparticles is unchanged while the size is varied, thus producing the variation of the linker's conductance G. Figure 3.12 shows the colour maps of the calculated normalized optical extinction cross section to observe the evolution of the plasmonic resonances in a linked gold nanoparticle dimer with interparticle gap $d = 1$ nm, where the conductivity κ_J of the linkers is fixed and its radius a is varied. We observe that, under these conditions, the behaviour of both the BDP and the CTP modes differs from the previous case. For the BDP, it is still possible to observe the blue-shift of the resonance, but its intensity decreases as the junction becomes wider (without regaining intensity). In the case of the CTP (in the top part of the maps, for longer wavelength values), after the emergence of the resonance we observe a considerable blue-shift as the radius a is increased. However, in contrast to the BDP, this resonance becomes more intense as the junction becomes wider. We also notice that, while the BDP is present for any considered value of the conductance and radius, the CTP dies out for situations of low conductance and small radius. A similar behaviour has been previously reported in the literature for touching nanoparticle dimers and loaded antennas[28, 31, 84]. While for the touching nanoparticle dimers the optical response is governed by the interparticle distance [28], when considering loaded antennas, the size of the load and the free-carrier den-

sity at the cavity are the key ingredients controlling the optical response [31, 84]. In particular, these cases correspond to the colour map of Figure 3.12 b), where the conductivity κ_J of the junction is equal to the conductivity κ_{Au} of the gold shells acting as electrodes.

We can also understand this behaviour in terms of the excitation of the BDP and CTP modes. The BDP mode, arising from the hybridization of the dipolar terms of the individual particles (see schematics in Figure 3.2 a)), can exist for any value of the radius of the linker, loosing intensity as the junction becomes wider and wider due to the increase of conductance. In contrast, the CTP mode, arising from the excitation of the hybridized monopolar ($l = 0$) individual nanoshell modes (see schematics in Figure 3.2 a)), is not sustained neither when there is no physical connection between the particles nor when the conductance is below G_{CTP}. This mode becomes the prominent resonant mode when conductance is large enough, satisfying the ordinary sum rules for the modes excitation. Figure 3.12 also shows the threshold value, $G_{CTP} = 468G_0$, obtained from Eq. (3.23) (an arrow in Figure 3.12 a) since the G_{CTP} falls out of the limits of the graphics). In this case the threshold value, calculated for the saturated wavelength of the CTP, around $\lambda = 1390$ nm, points out that, the higher conductivity κ_J we consider for the junction, the narrower junctions can sustain the CTP resonance. This relation between the size and conductance of the junction and its conductivity was expected from Eq. (3.2), which also shows that for an increasing conductivity of the material, the amount of material needed to sustain conductance is reduced. Thus, these results help to establish a connection between the spectral changes in optical spectra and molecular conductance including aspects such as the size of molecular bridges.

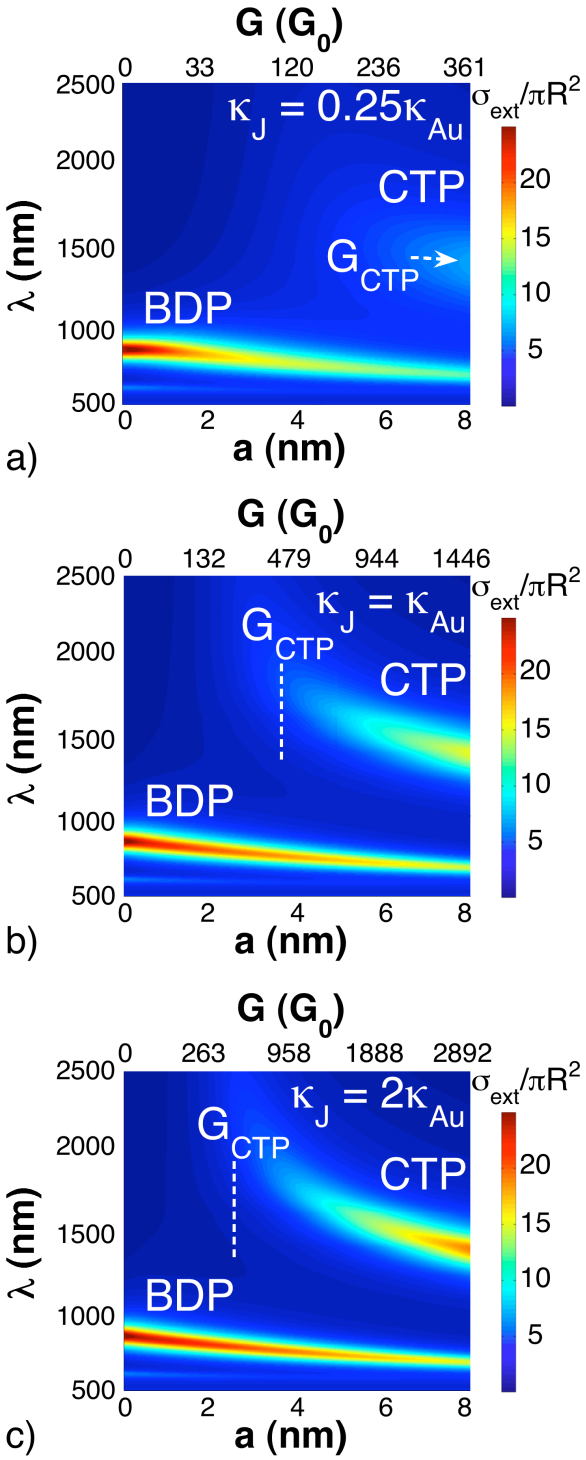

Figure 3.12: Colour maps of the calculated normalized optical extinction cross section showing the evolution of the plasmonic resonances BDP and CTP in a gold nanoparticle dimer with interparticle distance $d = 1$ nm linked by conductive molecular junctions with fixed conductivity κ_J while radius a is varied: a) $\kappa_J = 0.25\kappa_{Au}$, b) $\kappa_J = 1.09\kappa_{Au}$, c) $\kappa_J = 2\kappa_{Au}$. The vertical dashed white lines and the arrow in a) indicate the threshold of conductance of the CTP mode $G_{CTP} = 468G_0$.

3.4.2 Influence of the morphology: geometrical distribution of the electrical current within the linker

In order to explore the properties of the distribution of the electrical current through the junction, we study in this section how the optical response of the dimer is affected by morphological changes in the conductive junction. To this end, instead of a solid cylinder, we consider a hollow cylindrical shell, as depicted in the schematic representation in Figure 3.13. As for the solid case, the junction is characterized by its length d, corresponding to the interparticle gap. The junction is characterized by two parameters in this case: the internal and external radii of the conductive junction a_1 and a_2, respectively. To study how these two parameters affect the optical response we explore different situations. When we first fix the external radius a_2 and vary the internal radius a_1, varying the amount of material holding the current density.

As for the case of a solid junction, conductance and conductivity are related to each other via the geometric parameters:

$$\frac{G}{\kappa_J}(a_1, a_2, R, d) = \pi\Big\{\sqrt{R^2 - a_2^2} - \sqrt{R^2 - a_1^2} + (R + d/2)ln\Big[\frac{(R + d/2) - \sqrt{R^2 - a_2^2}}{(R + d/2) - \sqrt{R^2 - a_1^2}}\Big]\Big\}, \tag{3.24}$$

where a_1 and a_2 are the internal and external radii of the ring junction, R is the radius of the gold shell and d is the length of the junction. It is quite clear from Eq. (3.24) that Eq. (3.2) is recovered in the limit of small internal radius $a_1 \to 0$. Thus, in this hollow junction, the conductivity is given by:

$$\kappa_J = nG_0\Big\{\pi\Big\{\sqrt{R^2 - a_2^2} - \sqrt{R^2 - a_1^2} + (R + d/2)ln\Big[\frac{(R + d/2) - \sqrt{R^2 - a_2^2}}{(R + d/2) - \sqrt{R^2 - a_1^2}}\Big]\Big\}\Big\}^{-1}. \tag{3.25}$$

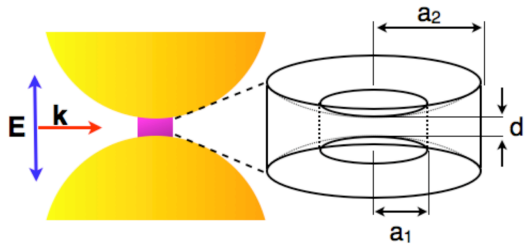

Figure 3.13: Schematic representation of a gold nanoshell dimer connected by a hollow conductive junction with ring-like shape. The junction is amplified so that its concave endings and geometrical parameters, internal radius a_1, external radius a_2, and length d, are clearly appreciated.

In Figure 3.14 a) we represent the calculated normalized optical extinction cross section for a gold nanoshell dimer linked by a conductive ring-like junction as the internal radius a_1 is increased, while the external radius and conductivity are fixed to $a_2 = 5$ nm and $\kappa_J = \kappa_{Au}$, respectively. This situation creates an increasingly thinner ring sustaining smaller conductance. The results are compared to the case of a solid molecular junction with the same radius and the same conductivity. For small values of a_1, even though we remove the central part of the cylinder, the spectrum of the solid junction does not vary noticeably. This behaviour suggests that the conduction through the molecular junction takes place mainly in the external region of the junction. This distribution of the current explains why the results of a solid junction are still reproduced when we remove wide central parts of the junction. In this case, the BDP mode red-shifts negligibly as the conductance decreases when considering thinner rings (with larger a_1), consistent with the behaviour of the BDP in solid junctions shown in Figure 3.12. The spectral position of the CTP, when fully formed (once the conductance value allows for its appearance), remains at the same spectral position for a fixed external radius, as the conductance is increased (decrease of

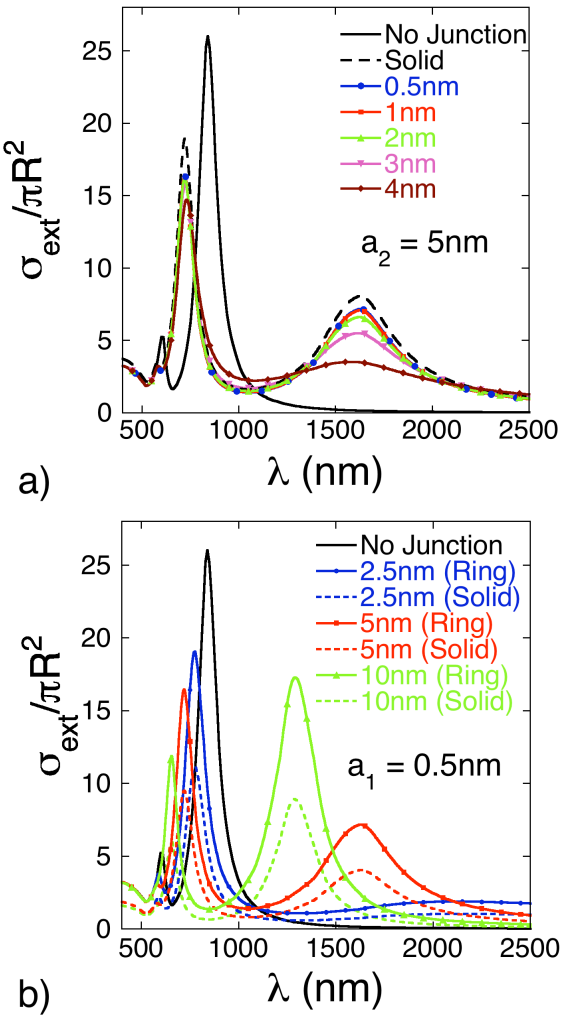

Figure 3.14: Calculated normalized optical extinction cross sections for a gold nanoshell dimer linked by a conductive cylindrical shell junction: a) The internal radius of the junction is varied from $a_1 = 0.5$ nm to $a_1 = 4$ nm., while the external radius is $a_2 = 5$ nm and the conductivity is $\kappa_J = \kappa_{Au}$. The dashed line represents the spectrum corresponding to a dimer connected by a solid junction with $a = 5$ nm. b) The external radius is varied from $a_2 = 2.5$ nm to $a_2 = 10$ nm (solid lines), while the internal radius is $a_1 = 0.5$ nm and the conductivity is $\kappa_J = \kappa_{Au}$. Dashed lines indicate the cases with solid junctions with the same external radii.

a_1), consistent with the behaviour shown for the CTP in Figure 3.11. We also observe in Figure 3.14 a) that the CTP excitation disappears when we consider a very narrow ring-like junction, an effect which can be explained due to the fact that the conductance of a ring-like junction with $a_1 = 4$ nm and $a_2 = 5$ nm is $G = 224G_0$, below the conductance threshold for the emergence of the CTP, as derived from Eq. (3.23).

In Figure 3.14 b) we represent the calculated normalized optical extinction cross section for a nanoshell dimer linked by a conductive ring-like junction as the external radius a_2 is increased. In this case the internal radius a_1 and conductivity κ_J are fixed so that every spectrum is comparable to the spectrum of a solid junction with the same external radius. If we compare every ring-like junction spectrum to its solid junction counterpart, we observe that the modes remain in the same position and the main effect of removing the central part of the junction is the increase of the intensity of the resonance. Considering the results shown in Figure 3.14 a), suggesting that the conduction between the nanoparticles occurs mainly out of the central part of the junction, we expect the spectra for thick ring-like junctions to be very similar to their solid counterparts. A small hollow cavity with $a_1 = 0.5$ nm hardly affects the conduction process through the junction. This can be observed in Figure 3.14 b), where the intensity of the BDP resonance decreases as the external radius is increased and the resonance is blue-shifted towards shorter wavelength values, exactly as in the case of solid junctions (see Figure 3.12). For the CTP resonance, its intensity is increased as the external radius is increased from 2.5 nm to 10 nm, and its peak position is blue-shifted, again consistent with the behaviour of a solid junction (see Figure 3.12).

3.5 Summary and remarks

In this chapter, we have studied theoretically the effect of the presence of a conductive bridge in the optical properties of a plasmonic cavity formed by a strongly coupled (non-touching) nanoparticle dimer. This system can be viewed as a first step to model two nanoparticles linked by an ensemble of molecules and study the interplay between optical and transport properties. Two plasmonic resonances are responsible for the main spectral features of the cavity: the BDP mode and the CTP mode. We have shown that the optical properties of the PCC depend strongly on the conductive and geometrical properties of the bridge. As the conductance is increased, the BDP mode blue-shifts and broadens, turning into a SBDP mode. For large conductance, a CTP mode emerges, becoming the prominent plasmon mode. We explain this behaviour in terms of a simple physical model which connects the time-scale of the optical process with the time-scale of the electron transport process. This relationship provides simple analytical expressions indicating the values of conductance where the SBDP mode develops and the CTP mode emerges.

It is worthwhile to point out the following remarks:

- A blue shift of the BDP mode and the emergence of a CTP mode as a function of the conductive overlap between two nanoparticles is an effect which has been previously reported in nanoparticle dimers and in cylindrical infrared gap antennas where metallic junctions bridge the gap [28, 29, 31, 76]. In these cases, the conductivity of the junctions is the same as the surrounding nanoparticles. In such a situation, the resulting plasmon modes are controlled only by the geometry of the junction. The results for the infrared antennas [31] are in excellent qualitative agreement with the present results. As the diameter and consequently the conductance of the junction is increased, the BDP blueshift and a low energy CTP appears

on the red side of the BDP for values of G_0 consistent with the conductivity of Au.

- The present calculation assumed a very simple frequency independent conductivity of the bridge between the two nanoparticles. This assumption was made to show that the optical response of the PCC is sensitive to the conductance of the junction. In a realistic situation, a frequency independent conductance cannot be assumed. For instance, if the junction consists of stacked molecules, one would expect that a tunneling or ballistic electron could induce both vibrational and low energy electronic excitations of the molecules. Such processes are likely to induce sharp resonances in the frequency dependent conductance. For metallic nanowire junctions, it is expectable that density of states effects and electron-electron interactions could also introduce a strong frequency dependence of the conductance.

- To experimentally probe situations where the junction conductance is expected to exhibit sharp resonances, the energy of the PCC plasmons across the conductance resonance would need to be tuned. Simply by changing the geometry of the structure, PCC resonances can be tuned across the visible region to the far infrared region of the spectrum. However, a more convenient approach for this tuning would be embedding the structure in a dielectric medium. Our calculations show that both the SBDP and CTP resonances are indeed highly tunable in this manner, and that both resonances readily can be shifted by more than 100 meV by simply changing their dielectric environment. This topic will be the object of Chapter 5.

- To take full advantage of the SBDP and CTP as fingerprints of electron transport processes at optical frequencies, it is possible to

optimize the PCC by using smaller diameter nanoparticles, plasmonic materials of lower conductivities, or plasmonic dimers with more redshifted plasmon modes. Such systems will present smaller threshold conductivities, and could thus be used to detect lower conductance values.

- The study of spectral changes in plasmonic nanocavities linked by conductive bridges such as molecules, nanotubes, and nanowires can be used to probe molecular conductance and electrical transport at visible frequencies, a regime not accessible through electrical measurements.

CHAPTER 4

OPTICAL AND TRANSPORT PROPERTIES OF EXCITONIC LINKERS

In parallel to the study of the optical properties of plasmonic systems, and the achievements in the field of molecular electronics, there has been a growing interest in the study of the interaction between plasmonic modes and molecular excitations. This interest has been fostered by the fact that the control of the coupling of molecular complexes to metallic structures is very important for the development of active plasmonics components dealing with optoelectronics signals [24, 65, 66, 67, 68, 85, 86]. The interaction between metallic nanoparticles and molecular complexes is mainly ruled by the Localized Surface Plasmon Resonances (LSPRs). These electromagnetic collective excitations couple to the optical excitonic transitions of molecules, consisting of electron-hole pairs created by the absorption of photons or the decay of plasmons. The coupling between electrons and plasmons creates mixed plasmon-exciton states, which are attractive due to their inherent interesting physical properties and also due to their broad range of potential applications, such as molecular switches, modulators or light harvesting structures

[24, 68, 87].

Along this chapter we present a theoretical study on the optical properties of a Plasmonic Cavity (PC), consisting of a strongly coupled nanoparticle dimer, linked by a material formed by conductive molecules which present an excitonic transition. This system can be viewed as a model of two nanoparticles connected by an ensemble of molecules, all of them characterized by the same excitonic transition. In the following, we show that the intrinsic nature of the linker, as well as its conductive properties, strongly affect the optical response of the Plasmon-Exciton Cavity (PEC).

4.1 Dielectric response of molecular linkers

As a means to simplify the computational efforts to calculate the optical response, in this chapter, instead of dimer composed of gold nanoshells, we consider simple gold spherical particles. The geometry of the system is depicted in Figure 4.1 a). The dimer consists of two gold nanoparticles of radii $R = 50$ nm with a minimum separation distance between them of $d = 1$ nm. No fundamental change is expected in relation to the previous consideration of a gold nanoshell dimer, apart from the different energy of the plasmonic resonances. The incident light is a plane-wave with the electric field linearly polarized along the longitudinal symmetry axis of the system and wave-vector $\mathbf{k}$ perpendicular to this symmetry axis.

As in previous chapters, the linker mimicking the ensemble of molecules is modelled as a cylinder with spherical endings which match perfectly the spherical surfaces of the nanoparticles (see Figure 4.1). Its geometric parameters are the radius a and length $d = 1$ nm. The frequency-dependent

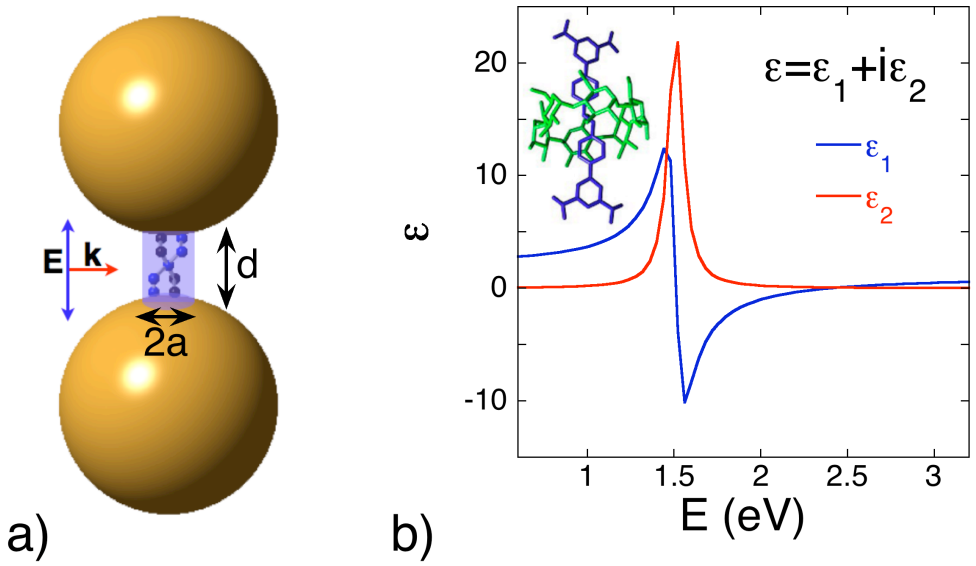

Figure 4.1: a) Schematic representation of a strongly-coupled gold nanoparticle dimer connected by a molecular linker modelled as a cylinder of radius a and length d. The radius of the gold nanoparticles is $R = 50$ nm and the minimum separation distance between their surfaces is $d = 1$ nm (proportionality is not realistic in this schematics). The incident electromagnetic signal is a plane-wave with polarization of the electric field $\mathbf{E}$ along the longitudinal symmetry axis of the system, and wave-vector $\mathbf{k}$ perpendicular to this symmetry axis. b) Real and imaginary parts of the dielectric function given by Eq. (4.1). The parameters correspond to rotaxane molecules in [24]: the energy of the excitonic transition is $E_{ex} = \hbar\omega_{ex} = 1.51$ eV ($\lambda_{ex} = 821$ nm), the damping factor $\gamma = 0.1$ eV and $f = 1.5$ as the reduced oscillator strength. A schematic representation of a rotaxane molecule is included.

dielectric function $\varepsilon(\omega)$ characterizing the gold particles is taken from the literature [40] and the whole system is considered to be suspended in vacuum.

Note that in this chapter, due to the usual energy-based nomenclature for excitonic transitions, we present all the results in terms of energy $E(eV)$ instead of the wavelength $\lambda(nm)$.

In order to characterize the dielectric response of the molecular linker, we use the Drude-Lorentz model to describe the presence of an optical interband transition in the junction and to establish its corresponding frequency-dependent dielectric function $\varepsilon(\omega)$. This model, widely used to study the optical properties of semiconductors, is able to describe the interaction between light and atoms or molecules charaterizing every atom or molecule through a resonant frequency ω_{ex}, corresponding to the frequency of the atomic or molecular transition. Thus, we assume that the linker is composed of identical molecules with a single molecular transition of energy $E_{ex} = \hbar\omega_{ex}$ characterizing them. According to the Drude-Lorentz model, the dielectric response function characterizing the linker is written as [34]:

$$\varepsilon(\omega) = 1 - \frac{f\omega_{ex}^2}{(\omega^2 - \omega_{ex}^2) + i\omega\gamma}, \tag{4.1}$$

where ω_{ex} is the natural oscillator frequency of the molecular transition, γ is the damping and f describes the reduced oscillator strength. In Figure 4.1 b), the real and imaginary parts of a Drude-Lorentz dielectric function are shown as functions of the energy. The parameters correspond to those of rotaxane molecules $E_{ex} = \hbar\omega_{ex} = 1.51$ eV ($\lambda_{ex} = 821$ nm), the damping factor $\gamma = 0.1$ eV [24] and $f = 1.5$ as the reduced oscillator strength. The dielectric response of a molecular linker clearly differs from that of a perfect conductor considered in Chapter 3. For the molecular linker, the real part of the dielectric function ε_1 takes both positive and negative values, contrary to the conductive junction, where

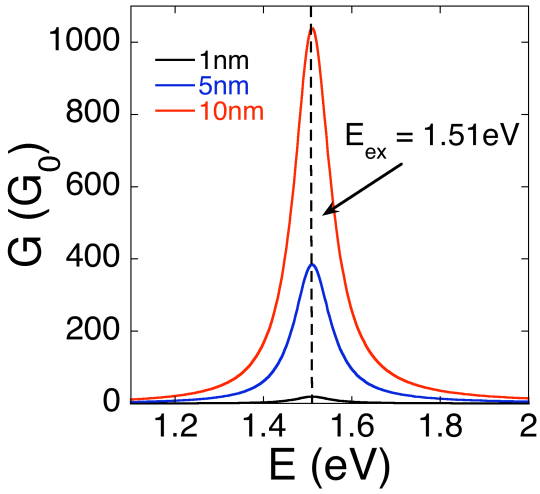

Figure 4.2: Resonant behaviour of the conductance G for molecular linkers of radii $a = 2$ nm, 4 nm and 6 nm with an excitonic transition of energy $E_{ex} = \hbar\omega_{ex} = 1.51$ eV ($\lambda_{ex} = 821$ nm), damping factor $\gamma = 0.1$ eV and $f = 1.5$ as the reduced oscillator strength, corresponding to rotaxane molecules [24].

$\varepsilon_1(\omega)$ is always positive. The imaginary part ε_2 for the molecular linker presents a resonant behaviour centred in $E = E_{ex} = \hbar\omega_{ex}$, in contrast to the conductive junction where its dependence is Drude-like. This affects the conductive properties of the molecular linker at these high frequencies, as shown in the following.

The conductivity $\kappa(\omega) = \kappa_1(\omega) + i\kappa_2(\omega)$ of the linker can be expressed in terms of $\varepsilon(\omega)$ via the following expression (see Eq. (1.8)):

$$\varepsilon(\omega) = 1 + i\frac{4\pi\kappa}{\omega}. \tag{4.2}$$

The conductance G associated to this molecular linker is related to the real part of the conductivity $\kappa_1(\omega)$ as follows:

$$G = \kappa_1(\omega)\pi\Big\{\sqrt{R^2 - a^2} - R + (d/2 + R)\ln\left[1 + 2(R - \sqrt{R^2 - a^2})/d\right]\Big\}, \tag{4.3}$$

where the analytically obtained geometrical factor is the same as the one used in Chapter 3, since we have considered the same cylinder with spherical endings to model the linker.

The consideration of a Drude-Lorentz dielectric response for the molecular linker implies the resonant behaviour of its conductance, as shown in Figure 4.2. In this particular case, we assume that the transition frequency is that of rotaxane molecules, as in Figure 4.1 b). We observe that the conductance G behaves as a lorentzian function located at the transition energy of the molecule E_{ex}, taken from the real part of the conductivity $\kappa_1(\omega)$. Figure 4.2 also shows that, for a given energy of the excitonic transition, the conductance of the molecular linker is increased as wider junctions are considered.

4.2 Influence of the size of molecular linkers

We begin analyzing the behaviour of the system when the radius of the linker is varied for a particular type of molecular junction, i.e., the case when we consider an increasing ensemble of molecules connecting both nanoparticles of the dimer, all of them with the same transition energy.

We explore two cases mimicking two different molecules: first rotaxane-like molecules [24], and second J-aggregate-like molecules [66]. Apart from the difference in the energy of the molecular transition, we consider for both cases very different values of the reduced oscillator strength f, which turns into remarkable differences in the optical response of connected dimers, as we detail below.

4.2.1 Optical response of rotaxane-like molecular linkers

Figure 4.3 a) shows the variation of the calculated normalized optical extinction cross-section of a nanoparticle dimer connected by a molecular linker of rotaxane-like molecules with the following parameters: $E_{ex} = \hbar\omega_{ex} = 1.51$ eV ($\lambda_{ex} = 821$ nm), $\gamma = 0.1$ eV [24], and $f = 1.5$. As a reference, in Figure 4.3 b) we also show a similar case where, instead of an excitonic molecular linker filling the PEC, a metallic linker of gold is considered. In the case of the excitonic molecular linker, the optical response of the nanostructure is mainly governed by three resonant modes (Figure 4.3 a)), whereas for the gold linker the Bonding Dimer Plasmon (BDP) and the Charge Transfer Plasmon (CTP) are the main modes observed in the spectrum (Figure 4.3 b)).

It is well known that, when the plasmonic cavity of a dimer is filled by a metallic load, there is a transfer of spectral weight between the BDP and the CTP modes [28, 31] (see also Figure 2.3). The BDP, arising from the hybridization of the dipolar modes ($l = 1$) of the individual nanoparticles, is the dominant mode in the disconnected situation, when there is no conductive path between both parts of the dimer, and also when narrow linkers are considered. Figure 4.3 b) shows that the BDP blue-shifts towards higher energies as the linker is wider (the conductance of the linker is thus increased). In contrast, the CTP mode, not allowed in the non-conductive situation, and arising from the hybridization of the monopolar modes ($l = 0$) of the individual nanoparticles, emerges as the conductive path between both parts of the dimer becomes wider. The CTP presents a dramatic blue-shift towards higher energy ranges as the radius of the linker is increased (implying an increase of the conductance). In addition to the BDP and CTP modes, a Bonding Quadrupolar Plasmon (BQP) mode is also observed as a small spectral feature around $E_{BQP} = 2.30$ eV ($\lambda_{BQP} = 540$ nm). This BQP mode, arising from

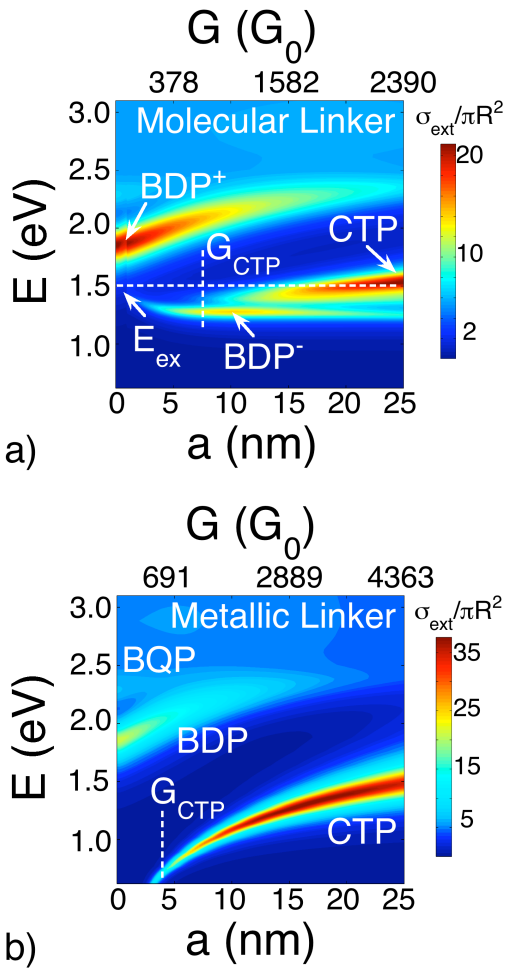

Figure 4.3: a) Calculated normalized optical extinction cross-section of a gold nanoparticle dimer bridged by a molecular linker with excitonic character as the radius of the linker is varied. The energy of the excitonic transition is $E_{ex} = 1.51$ eV, indicated by the horizontal, white, dashed line. The vertical, white, dashed line indicate the size of the linker corresponding to the threshold value of conductance $G_{CTP} = 672G_0$ for the emergence of the CTP mode. The points indicated by BDP^+, BDP^- and CTP correspond to the near-field distributions, plotted in Figure 4.4, of these modes. b) Calculated normalized optical extinction cross-section of a gold nanoparticle dimer bridged by a metallic (gold) linker. The vertical, white, dashed line indicate the size of the linker corresponding to the threshold value of conductance $G_{CTP} = 656G_0$ for the emergence of the CTP mode.

the hybridization of the quadrupolar modes ($l = 2$) of the individual nanoparticles, looses intensity as the conductance of the plasmonic cavity increases as well.

In the case of the molecular linker, Figure 4.3 a) shows that the BDP and BQP modes, found at $E_{BQP} = 1.85$ eV ($\lambda_{BDP} = 670$ nm) and $E_{BQP} = 2.30$ eV ($\lambda_{BQP} = 540$ nm), respectively, in the absence of linker, also blue-shift and loose intensity progressively as a is increased. However, when we observe the Near-InfraRed (NIR) range of the spectrum, two resonant modes appear, in contrast to the presence of only the CTP resonance in the case of the metallic linker (Figure 4.3 b)).

From the near-field maps associated to the resonances in Figure 4.4, which will be commented in detail later, it can be checked that the most red-shifted resonance of the PEC, around $E \approx 1.29$ eV ($\lambda \approx 960$ nm), sustains a BDP-like nature and it is named as BDP^{-}. The higher energy mode, initially found around $E \approx 1.85$ eV ($\lambda \approx 670$ nm), also presents a BDP-like nature and it is named as BDP^{+}. In contrast, the resonance in-between, around $E \approx 1.52$ eV ($\lambda \approx 815$ nm), sustains a clear CTP-like nature. This mixing of the different plasmonic resonances gives rise to a more complex optical response of the molecular linker, in comparison to the response of the metallic linker. The splitting of the BDP mode, which does not appear in the metallic case, can be understood in terms of the coupling of the excitons to the plasmonic cavity modes of the nanostructure. Another difference between the response of both linkers is that, for the molecular linker, the CTP mode does not emerge as a blue-shift from the NIR range of the spectrum, but it appears approximately at the transition energy E_{ex} of the exciton. Consequently, these results show that the consideration of a more complex nature characterizing the optical response of the linker in the PEC strongly affects the behaviour of the plasmonic cavity modes.

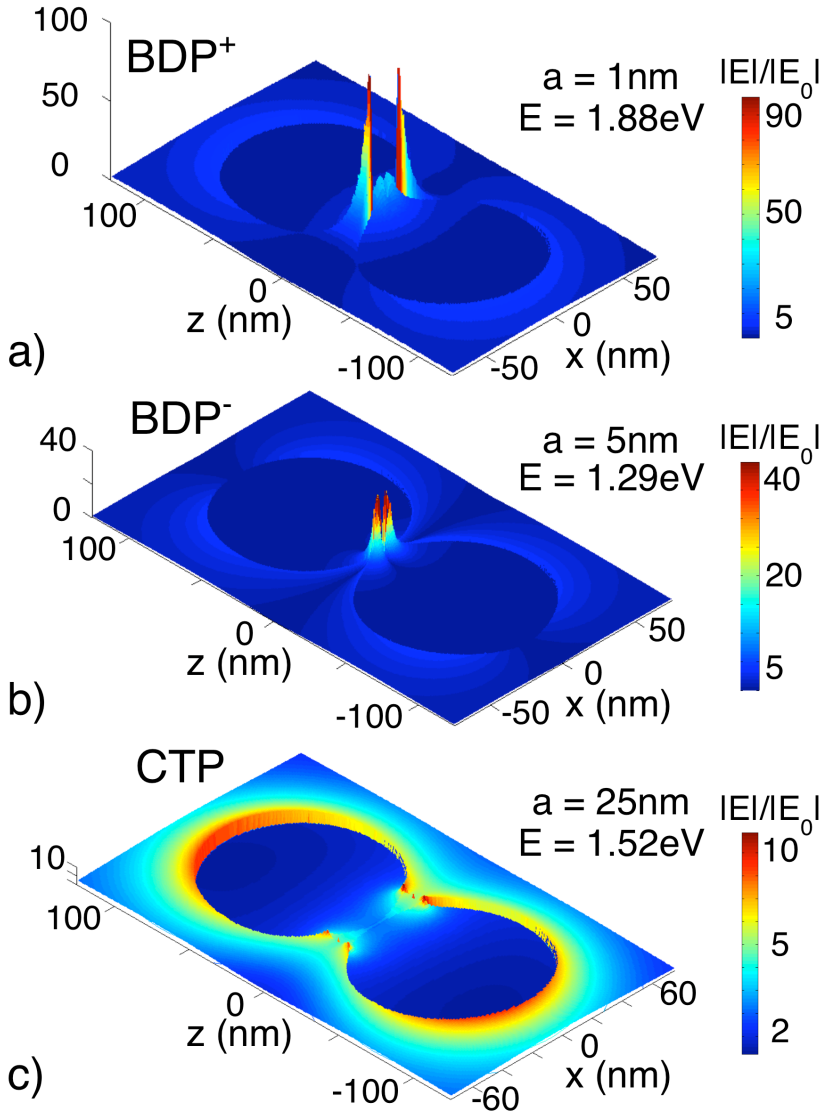

Figure 4.4: Near-field distributions of a gold nanoparticle dimer connected by a molecular linker. Each surface plot corresponds to the peaks marked as BDP^{+}, BDP^{-} and CTP in Figure 4.3 a). The maps represent the electric field in the plane defined by the wave-vector $\mathbf{k}$ and the incoming electric field $\mathbf{E}$ (see Figure 4.1 a)). a) BDP-like mode with $a = 1$ nm and $E = 1.88$ eV, b) BDP-like mode with $a = 5$ nm and $E = 1.29$ eV and c) CTP-like mode with $a = 25$ nm and $E = 1.52$ eV.

4.2.1.1 Near-field distributions

In order to explore more deeply the nature of these mixed states, we plot in Figure 4.4 three representative cases of the distribution of the intensity of the electric field in dimers connected by molecular linkers. The cases correspond to the peaks marked as BDP^+, BDP^- and CTP in Figure 4.3 a). The surface plots represent the electric field in the plane defined by the wave-vector **k** and the direction of polarization of the incoming electric field **E** (see Figure 4.1 a)). Figures 4.4 a), b) and c) correspond to dimers bridged by molecular linkers with radii $a = 1$ nm, 5 nm and 25 nm at the energies $E = 1.88$ eV, 1.29 eV and 1.52 eV, respectively. The maps corresponding to peaks BDP^+ and BDP^- resemble the dipolar BDP pattern, with the characteristic hot spot in the gap between both nanoparticles due to the huge field-enhancement. For peak BDP^+ it is more concentrated in the outer part of the PEC, but for peak BDP^- it is more focused in the centre. Furthermore, the dipolar distributions of the individual particles are oriented in a different way, for peak BDP^+ it looks more like in the conventional BDP, but for peak BDP^- the individual dipoles are oriented in the transverse direction (perpendicular to the axis of the linker). This behaviour suggests the interaction with higher order modes, as will be shown later. In contrast, peak CTP clearly corresponds to a CTP pattern: the field is homogeneously distributed all around the structure due to the spread of the surface charge density along the particles, showing that the structure behaves as a dipole considering the dimer as a whole.

4.2.1.2 Threshold of conductance for the CTP mode in PECs

We have shown in Chapter 3 that, when a dimer is conductively connected there is a threshold of conductance, given by $G_{CTP} = \omega_{CTP} R^2/4\pi d$ (Eq. 3.23), quantifying the minimum of conductance in the Plasmon Conductive Cavity (PCC) for the CTP mode to emerge. For the gold

linker, with $R = 50$ nm and $d = 1$ nm, the CTP mode saturates for very large conductance, around $E_{CTP} = 1.49$ eV ($\lambda_{CTP} = 835$ nm), leading to a threshold value of $G_{CTP} \approx 656G_0$, in good agreement with our estimations (see the vertical, white, dashed line included in Figure 4.3 b)). Since the PEC also presents a conductive behaviour, we can apply the same arguments in the case of dimers connected by molecular linkers. For the rotaxane-like molecules under consideration in Figure 4.3 a), the CTP mode saturates around $E_{CTP} = 1.52$ eV ($\lambda_{CTP} = 815$ nm), leading to $G_{CTP} \approx 672G_0$. This threshold value, indicated by a vertical, white, dashed line in Figure 4.3 a), is also in good agreement with the emergence of the CTP mode, corroborating that the time-scale considerations discussed in Chapter 3, which relate the conductance of the junction to the optical properties, are still valid for molecular linkers.

4.2.2 Optical response of J-aggregate-like molecular linkers

In order to explore the optical response of other type of molecules and to establish a comparison with the case of rotaxane molecules, we consider the parameters characterizing a molecular linker which correspond to J-aggregate-like molecules. In this case, the transition energy is $E_{ex} = 1.79$ eV ($\lambda_{ex} = 693$ nm), the damping factor is $\gamma = 0.052$ eV, and the reduced oscillator strength factor is $f = 0.02$ [66]. Thus, the molecular transition for J-aggregates presents higher energy than that of rotaxane molecules, and the values for both the damping and the reduced oscillator strength are very different in comparison to the values for rotaxanes. These parameters lead to the behaviour of the conductance shown in Figure 4.5 a). It is clear, when comparing Figures 4.5 a) and 4.2, that the conductive capacity of the J-aggregate-like molecules under consideration is much weaker than for rotaxane. This difference has consequences in the optical response.

Figure 4.5 b) shows the calculated normalized optical extinction cross-section of a gold nanoparticle dimer bridged by a J-aggregate-like molecular linker as the radius of the linker is varied. As for the rotaxane-like molecular linker (see Figure 4.3), the BDP mode also splits into two modes. In this case, the magnitude of the blue-shift is not as large as for the rotaxane. We also observe that, the CTP mode in-between the two BDP coupled modes does not emerge, even though we have increased the radius of the linker up to $a = 32$ nm. This can be explained as a result of the low conductivity of the linker, several orders of magnitude below the conductivity of the rotaxane and gold. We have shown in Chapter 3 that the CTP mode needs really large conductance to be sustained, a condition which is not fulfilled by the low conductance of the molecule under consideration in this section.

4.3 Role of the excitonic frequency and conductance of molecular linkers

In order to understand the splitting of the modes, and the differences in the optical response for different molecular linkers, we explore the effect of changing the excitonic frequency ω_{ex} and the conductance of the ensemble of molecules connecting both parts of the dimer for a given size of the linker. We have considered the response of the molecule in two different ways, which affect the dielectric response of the molecular linker as shown in Figure 4.6. In the first approach, the energy of the excitonic transition $E_{ex} = \hbar\omega_{ex}$ describing the molecules is varied, as well as the reduced oscillator strength f, so that the product $f\omega_{ex}^2$ in Eq. (4.1) is constant. In this manner, shown in Figure 4.6 a), as we consider lower energies of the transition E_{ex}, the oscillator strength increases. The centre of the lorentzian function describing the conductance in the cavity shifts while its maximum does not vary. In this way, the intensity

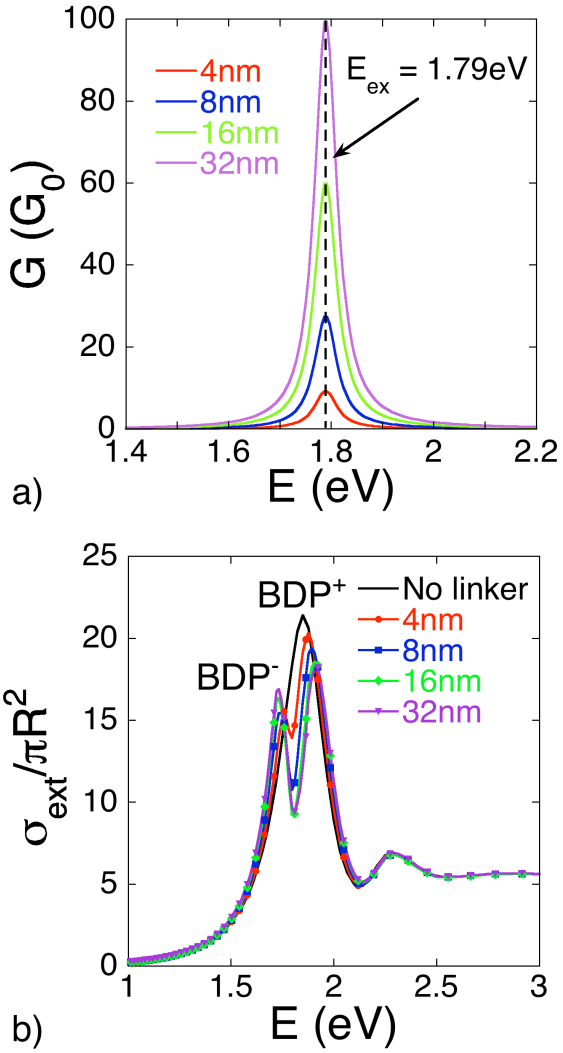

Figure 4.5: a) Resonant behaviour of the conductance G for molecular linkers of radii $a = 4$ nm, 8 nm, 16 nm and 32 nm with an excitonic transition of energy $E_{ex} = \hbar\omega_{ex} = 1.79$ eV ($\lambda_{ex} = 693$ nm) corresponding to J-aggregates [66]. b) Calculated normalized optical extinction cross-section of a gold nanoparticle dimer bridged by a molecular linker as the radius of the linker is varied. The rest of the geometrical parameters are the same as in Figure 4.1. The parameters characterizing the dielectric response of the linker are the same as in a).

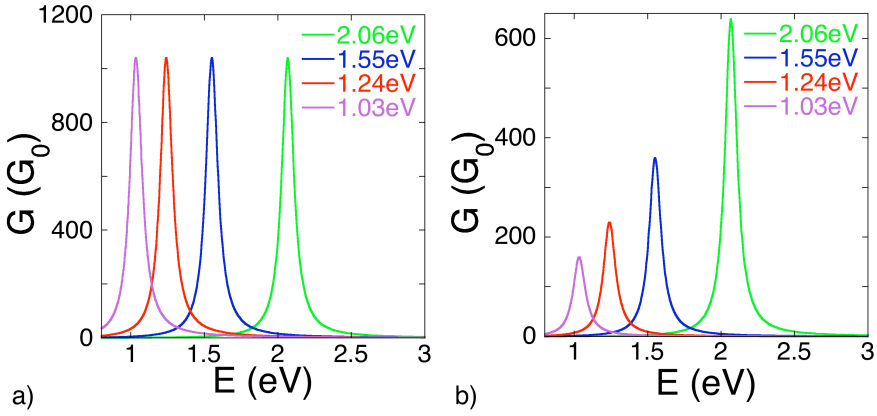

Figure 4.6: Evolution of conductance of molecular linkers with fixed radii, $a = 10$ nm, and varying E_{ex}. a) The reduced oscillator strength is varied so that $f\omega_{ex}^2$ =Const. b) The reduced oscillator strength is fixed $f = 0.5$.

of the maximum of the conductance remains unaltered, so that we explore situations with large values of G. The second approach consists of varying the energy of the molecular transition while the reduced oscillator strength is kept constant. Figure 4.6 b) shows the evolution of the conductance for different excitonic transition energies E_{ex} and reduced oscillator strength $f = 0.5$. In this case, the consideration of molecular transitions with lower energy, not only implies the shift of the centre of the lorentzian function describing G, but also the reduction of the intensity of the maximum of conductance.

4.3.1 Variation of the transition frequency and the reduced oscillator strength

Figure 4.7 shows the calculated normalized optical extinction cross-section of a gold nanoparticle dimer bridged by a molecular linker as the energy and the reduced oscillator strength characterizing the optical transition in the cavity is varied for a given radius. In this case, four

radii have been considered, a = 1 nm, 5 nm, 10 nm and 15 nm. Even for the thinest linker, we observe that the BDP and the BQP resonances split into two branches, BDP^+, BDP^-, BQP^+ and BQP^-, showing an anti-crossing behaviour centred in the point of intersection of the energy-line of the exciton and the BDP and BQP energy-lines. The situation is more clear in the case of the BDP than in the BQP due to the higher intensity of the peaks of the BDP mode. In Figure 4.7, we can observe that the energy of one of the branches, E^+_{BDP}, is above the energy of the plasmon cavity mode, while the energy of the other branch, E^-_{BDP}, is below the corresponding plasmon energy. Fig. 4.7 also shows that, as the linker becomes wider (from a) to d), a = 1 nm - a = 15 nm), the energy splitting between the energies E^- and E^+ of the coupled modes becomes larger. This energy splitting between the coupled modes is the Rabi splitting, $\hbar\Omega_R$, which governs the coupling of atomic or molecular excitations in a cavity to the cavity modes and which has been deeply studied in the field of atomic physics [88, 89]. In the cases under consideration here, the Rabi splitting is of the order of hundreds of meV.

In order to show this behaviour in more detail, we have plotted in Figure 4.8 a) some particular cases extracted from Figure 4.7, where the radius of the molecular linker is a = 10 nm. For the case with lowest transition energy, E_{ex} = 1.24 eV (top panel), the low-energy plexcitons, BDP^- and BQP^-, can be appreciated in the lower energy range of the spectrum, while the high-energy plexciton BDP^+ is the main spectral feature in the higher energy range. As E_{ex} is increased, both the BDP^- and BQP^- blue-shift towards higher energies, becoming the BDP^- plexciton the predominant mode. In parallel, the BDP^+ slightly blue-shifts while loosing intensity. Figure 4.8 b) shows the anti-crossing behaviour of the high-energy BDP^+ and low-energy BDP^- plexcitons in Figure 4.8 a).

It is well known that, when an atom or molecule is located in a

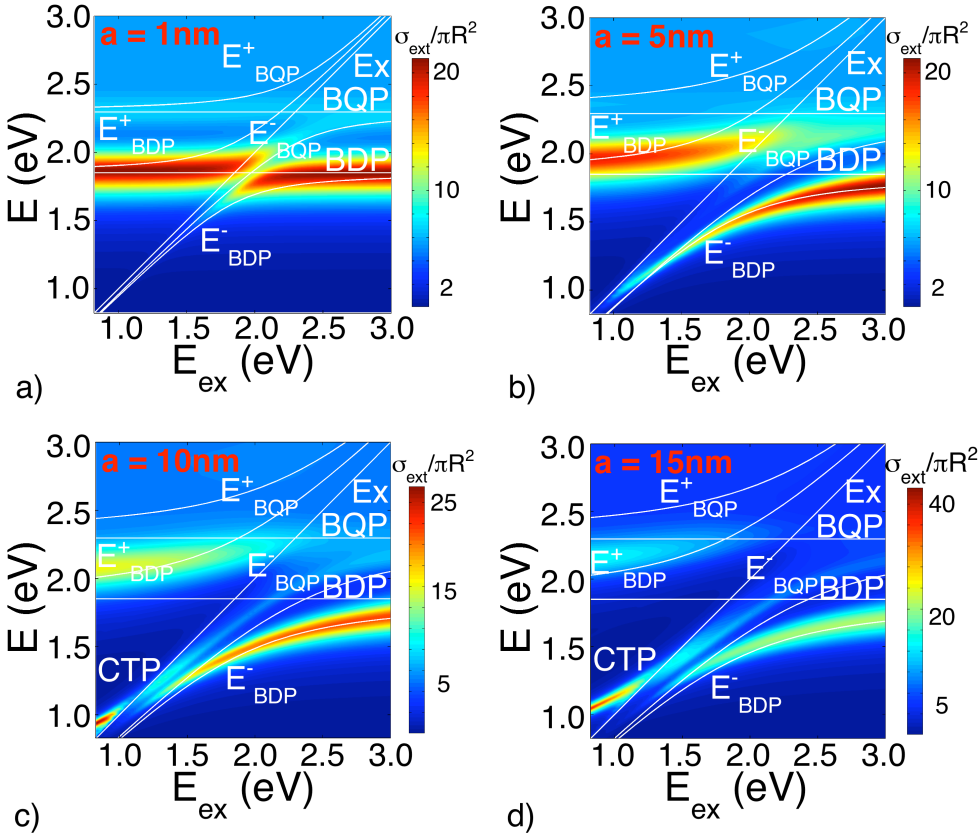

Figure 4.7: Calculated normalized optical extinction cross-section of a gold nanoparticle dimer bridged by a molecular linker, with length $d = 1$ nm and fixed radius a, as the energy and the oscillator strength of the optical transition in the cavity are varied. a) $a = 1$ nm, b) $a = 5$ nm, c) $a = 10$ nm and d) $a = 15$ nm. The white solid lines included indicate the following: Ex is the exciton energy-line, BDP and BQP are the energy-lines of the dipolar and quadrupolar bonding plasmon modes when there is no linker; E^+_{BDP}, E^-_{BDP}, E^+_{BQP} and E^-_{BQP} indicate the plexciton modes derived from Eq. (4.4) arising from the coupling of the exciton to the BDP and BQP modes.

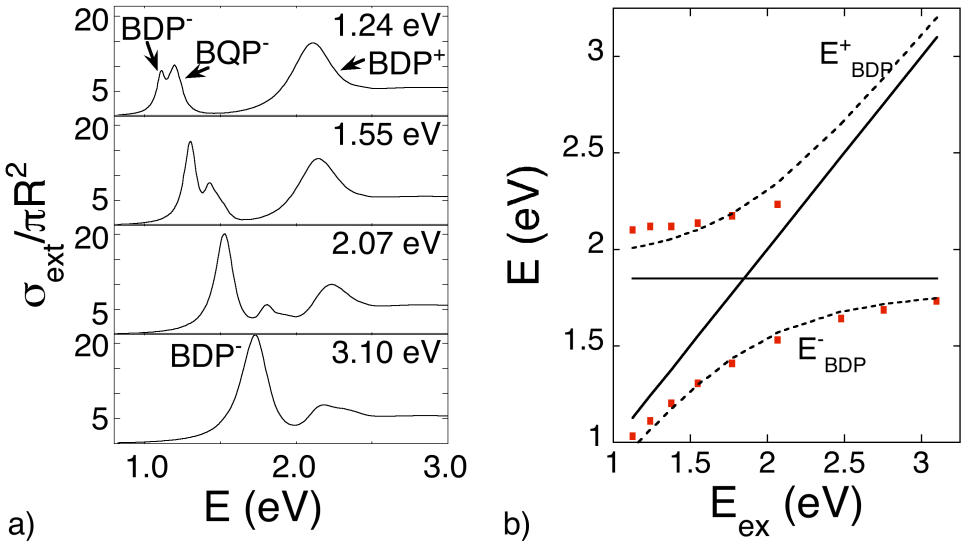

Figure 4.8: a) Calculated normalized optical extinction cross-section of a gold nanoparticle dimer bridged by a molecular linker with length $d = 1$ nm and fixed radius $a = 10$ nm, as the energy and the oscillator strength of the optical transition in the cavity are varied. b) Anti-crossing behaviour of the BDP^+ and $BDP-$ plexciton modes. The red squares indicate the maxima of the modes in a) and the dashed lines included indicate the energies of the BDP^+ plexciton (E^+_{BDP}) and the BDP^- (E^-_{BDP}) derived from Eq. (4.4).

cavity, the resonances of the cavity split. In this particular system, the resonances of the plasmon cavity, BDP and BQP, couple to the excitons characterizing the molecules linking both parts of the dimer. From now on, we will refer to this coupled modes as plexcitons. E^-_{BDP} and E^+_{BDP} are the lower and higher energy plexcitons arising from the coupling between the BDP mode and the exciton, and E^-_{BQP} and E^+_{BQP} are the lower and higher energy plexcitons arising from the coupling between the BQP mode and the exciton. This coupling of the plasmonic cavity modes to the excitons in the cavity has been interpreted in terms of two coupled

oscillators [85]. The allowed energy of the coupled mode is given by:

$$E^{\pm} = \frac{E_P + E_{ex}}{2} \pm \left[\left(\frac{\hbar\Omega_R}{2} \right)^2 + \frac{1}{4}(E_P - E_{ex})^2 \right]^{1/2}, \tag{4.4}$$

where E_P and E_{ex} are the energies of the plasmonic modes (BDP or BQP) and the exciton, respectively, and $\hbar\Omega_R$ is the Rabi splitting. A more detailed derivation of Eq. (4.4) is presented in Appendix B. The magnitude of the Rabi splitting is obtained from our calculations when $E_P = E_{ex}$. The results of this approximation presented in Eq. (4.4) are shown in Figure 4.7 as white lines superimposed on the electrodynamical calculation, obtaining a good agreement. In addition to the coupling giving rise to the plexcitons, Figure 4.7 also shows an intense interaction between the coupled modes of the BDP and the BQP, which increases as the linker becomes wider.

In Figures 4.7 c) and d), where $a = 10$ nm and 15 nm, respectively, we observe the emergence of the CTP mode, in contrast to the cases with $a =$ 1 nm and 5 nm, where the CTP does not appear. In both cases, the CTP mode interacts with the exciton and the lower energy BDP^- and BQP^-, as it emerges. The emergence of the CTP mode can also be understood once more in terms of the conductance threshold G_{CTP} obtained from time-scale arguments (see Eq. 3.23). We have described that for very large conductance, the CTP mode saturates around $E_{CTP} = 1.52$ eV, leading to a threshold value of the conductance $G_{CTP} \approx 672G_0$. For molecular linkers with radii $a = 1$ nm, the maximum of conductance, occurring at $\omega = \omega_{ex}$, is $G(a = 1 \text{ nm}) \approx 6G_0 << G_{CTP}$, therefore a much lower value than the conductance threshold. For molecular linkers with radii $a = 5$ nm, the maximum of conductance is $G(a = 5 \text{ nm})$ $\approx 122G_0 << G_{CTP}$, again below the conductance threshold. In contrast, when $a = 10$ nm and $a = 15$ nm, the maxima of the conductance of the linker are $G(a = 10 \text{ nm}) \approx 1000G_0 > G_{CTP}$ and $G(a = 15 \text{ nm})$ $\approx 1500G_0 > G_{CTP}$, respectively. Thus, for the cases with wider linkers, the conductance of the PEC is large enough for the CTP mode to emerge,

as corroborated by Figures 4.7 c) and d).

4.3.2 Variation of the transition frequency

As stated in the beginning of this section, the second way of varying the dielectric response of the molecular linker consists in the variation of the frequency of the energy of the molecular transition, while the reduced oscillator strength remains unaltered. The consequences in the values of conductance of the PEC have been shown in Figure 4.6 b). Figure 4.9 shows the calculated normalized optical extinction cross-section of a gold nanoparticle dimer bridged by a molecular linker, as the energy of the optical transition in the cavity E_{ex} is varied for a given radius, and the reduced oscillator strength is kept constant $f = 0.5$. As in Figure 4.7, four radii have been considered, $a = 1$ nm, 5 nm, 10 nm and 15 nm, in order to compare exactly both cases.

Figure 4.9 shows that, as expected, the plasmonic cavity modes split into two plexcitonic branches due to the coupling between the plasmon cavity modes and the molecular transitions. As observed in Figure 4.7, the E^{+}_{BDP} and the E^{+}_{BQP} are the high energy plexcitons arising from the coupling of the BDP and BQP modes to the exciton. The E^{-}_{BDP} and E^{-}_{BQP} are the low energy plexcitons arising from the coupling of the BDP and BQP modes to the exciton. These coupled modes show the same anti-crossing behaviour observed in the previous case. In both cases, the magnitude of the Rabi splitting is also similar. However, there is a remarkable difference in relation to the emergence of the CTP mode.

For the cases of narrow linkers in Figures 4.9 a) and b), with $a = 1$ nm and $a = 5$ nm, respectively, we do not observe the emergence of the CTP mode. In these cases, the maximum of the conductance takes place when the energy of the molecular transition is the largest in the range we have considered, as in Figures 4.7 a) and b). For $a = 1$ nm and $a = 5$ nm, the maxima of the conductance are $G = 8G_0$ and $G = 159G_0$, respec-

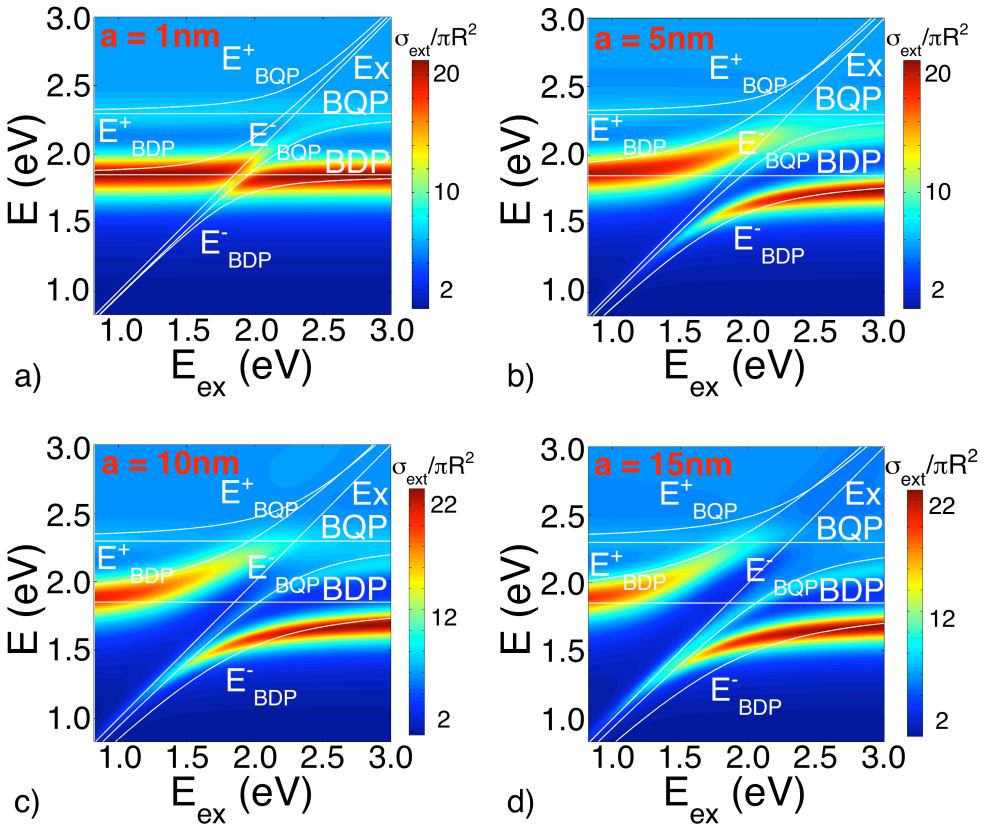

Figure 4.9: Calculated normalized optical extinction cross-section of a gold nanoparticle dimer bridged by a molecular linker, with length $d = 1$ nm and fixed radius a, as the energy of the exciton is varied and the reduced oscillator strength of the molecular transition is constant $f = 0.5$. a) $a = 1$ nm, b) $a = 5$ nm, c) $a = 10$ nm and d) $a = 15$ nm. The white solid lines included indicate the following: Ex is the exciton energy-line, BDP and BQP are the energy-lines of the dipolar and quadrupolar bonding plasmon modes when there is no linker; E^+_{BDP}, E^-_{BDP}, E^+_{BQP} and E^-_{BQP} indicate the plexciton modes derived from Eq. (4.4) arising from the coupling of the exciton to the BDP and BQP modes.

tively, much lower than the conductance threshold G_{CTP}. In contrast to Figures 4.7 c) and d), for the cases with wider linkers in Figure 4.9 c) and d), with $a = 10$ nm and $a = 15$ nm, respectively, we do not observe the emergence of the CTP mode. The conductance is therefore the key aspect. For $a = 10$ nm, the maximum of the conductance is $G = 429G_0$ for the largest transition energy. For $a = 15$ nm, the maximum of the conductance is $G = 663G_0$ for the largest transition energy. In both cases, the conductance of the PEC is below the conductance threshold G_{CTP}, thus explaining why the CTP mode is not present at all in this description of the molecular response.

4.3.3 Rabi splitting

We finish the study on the optical response of dimers connected by PECs with an analysis of the Rabi splitting for the gold dimer system.

As already stated, the Rabi splitting is a consequence of the coupling of the original plasmonic cavity modes modes and the molecular transition of the linker. The magnitude of the Rabi splitting $\hbar\Omega_R$ is obtained from the electrodynamical calculations when the energy of the molecular transition coincides with the energy of the plasmonic cavity mode. Figure 4.10 a) shows the calculated normalized optical extinction cross-section of a gold nanoparticle dimer bridged by a molecular linker, with length $d = 1$ nm and radius $a = 5$ nm, when $E_{ex} = E_{BDP} = 1.85$ eV, as the reduced oscillator strength f is varied. The difference in energy between the two peaks of the E^+_{BDP} and E^-_{BDP} is the Rabi splitting. Figure 4.10 b) shows the evolution of the magnitude of $\hbar\Omega_R$ for the BDP plexciton as f is varied. In this gold nanoparticle system connected by PEC, the magnitude of the Rabi splitting is in the range of meV, as for other similar systems of plasmonic structures-molecular complexes [85]. The Rabi splitting increases as f is also increased, showing a trend of saturation as $f \approx 1$. Analogously, Figure 4.10 c) shows the evolution of the Rabi

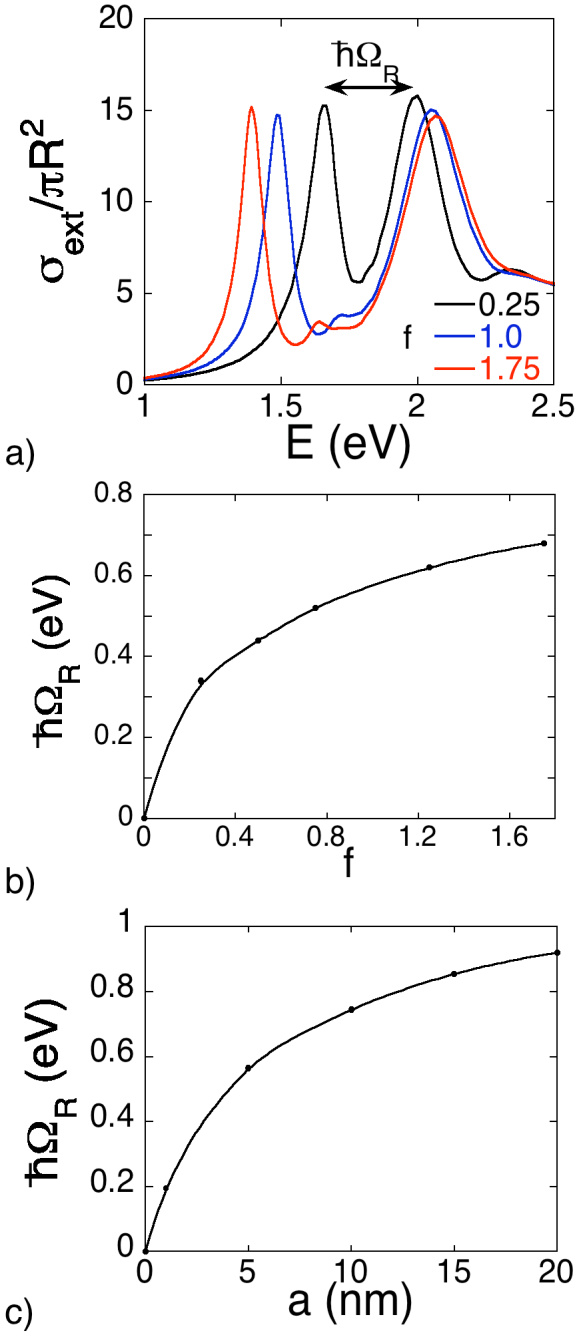

Figure 4.10: a) Calculated normalized optical extinction cross-section of a gold nanoparticle dimer bridged by a molecular linker, with length $d = 1$ nm and radius $a = 5$ nm, when $E_{ex} = E_{BDP} = 1.85$ eV, as the reduced oscillator strength f of the molecular transition is varied. The arrow indicate the Rabi splitting for one of the cases. b) Evolution of the Rabi splitting for the BDP plexciton as the reduced oscillator strength f is varied. The magnitude is obtained from the calculations in a). c) Evolution of the Rabi splitting for the BDP plexciton as the radius of the molecular linker a is varied, where $f\omega_{ex}^2$ =Const., corresponding to the cases in Figure 4.7.

splitting for the BDP plexciton as the radius of the molecular linker a is varied, where $f\omega_{ex}^2$ =Const., corresponding to the cases in Figure 4.7. In this case, the Rabi splitting increases rapidly as the radius of the molecular linkers grows, but for wider linkers, with $a > 10$ nm, a tendency to saturation is also observed.

4.4 Summary

In this chapter we have studied theoretically the effect of the presence of a conductive linker with an excitonic transition in the optical properties of a plasmonic cavity formed by a strongly coupled (non-touching) nanoparticle dimer. This system can be viewed as a model of two nanoparticles linked by an ensemble of molecules, all of them with the same excitonic transition. The transport process through the linker is more complex than in the case of the conductive linker studied in Chapter 3, due to the resonant behaviour of the conductance derived from the presence of the exciton.The consideration of a conductive bridge linking the dimer with a more complex dielectric response changes dramatically the optical properties of the connected nanostructure. We have shown that the plasmonic cavity modes, the BDP and BQP, couple to the excitons of the molecular transition giving rise to plasmon-exciton states, called plexcitons. The coupled plexciton modes exhibit an anticrossing behaviour with two branches, centred in the intersection between the plasmonic mode and the exciton energy-lines. A simple model of two coupled oscillators explains this anti-crossing behaviour. It has also been shown that the emergence of the CTP mode depends strongly on the conductance through the PEC and that the threshold value of the conductance derived from the time-scale approach is still valid for dimers linked by molecular junctions.

CHAPTER 5

SENSING IN PLASMONIC CAVITIES

The use of metallic nanoparticles as ultrasensitive sensors has turned into one of the most promising applications of plasmonics [69, 90, 91, 92]. As already stated in Chapter 1, the spectral position of the Localized Surface Plasmon Resonance (LSPR) of a metallic nanostructure depends on the size and shape of the plasmonic nanoparticles forming the system, on the dielectric response of the constituent materials and also on the dielectric environment. When the dielectric constant characterizing the embedding medium is varied, the spectral position of the LSPR changes, fostering studies based on the high sensitivity of the spectral signature of the LSPR to the environment. In these works [69, 70, 93], a red-shift of the plasmon resonance was observed as the refractive index n of the surrounding medium is increased (thus increasing the real part of the dielectric function), as well as an increase of its intensity. This behaviour was found to be systematic for different types of nanostructures, such as nanorods, nanoshells, nanodisks [70] or nanorings [93], with different degrees of sensitivity depending on the produced shifts.

Lately, the use of Fano resonances has been proposed for LSPR sensing [71, 94, 95]. The Fano interference is a long known phenomenon

which has been studied in atomic and condensed matter physics [96, 97]. It was introduced in the context of absorption spectra when there is an interference of a discrete state with a continuum giving rise to a sharp peak in the excitation spectra [98]. A Fano-like interference is a phenomenon occurring when the energy transition between an initial and a final state has two paths, and these paths interfere. Classical analogs to Fano-like interferences have been recently studied [99, 100] in the framework of coupled harmonic oscillators, and, in particular, the Fano-like phenomenon has attracted much attention in relation with plasmonic systems [101, 102]. The proposal of the Fano-like plasmonic resonances for LSPR sensing is mainly based on their characteristic narrow shape, which makes the relative shift of a resonance with respect to its width more pronounced.

In this chapter, we conclude our study of conductive linkers connecting plasmonic systems with an analysis of their potential use for LSPR sensing. We begin exploring the shift-based LSPR sensing. We also propose a new paradigm for sensing with the use of plasmon-exciton systems where the LSPR sensing is based on the changes in intensity of the spectral peaks, rather than on the shifts of the resonances.

5.1 Shift-based sensing

In this section, we analyze the sensitivity of the plasmonic systems studied along this thesis to the dielectric environment. In order to introduce the shift-based LSPR sensing, we begin exploring the sensitivity of the LSPR of a gold spherical nanoparticle to changes in the dielectric embedding medium. We continue with the study of LSPR sensing in dimers connected by Plasmon Conductive Cavities (PCCs) and in dimers connected by Plasmon Exciton Cavities (PECs).

Figure 5.1 shows the sensitivity of a gold spherical nanoparticle

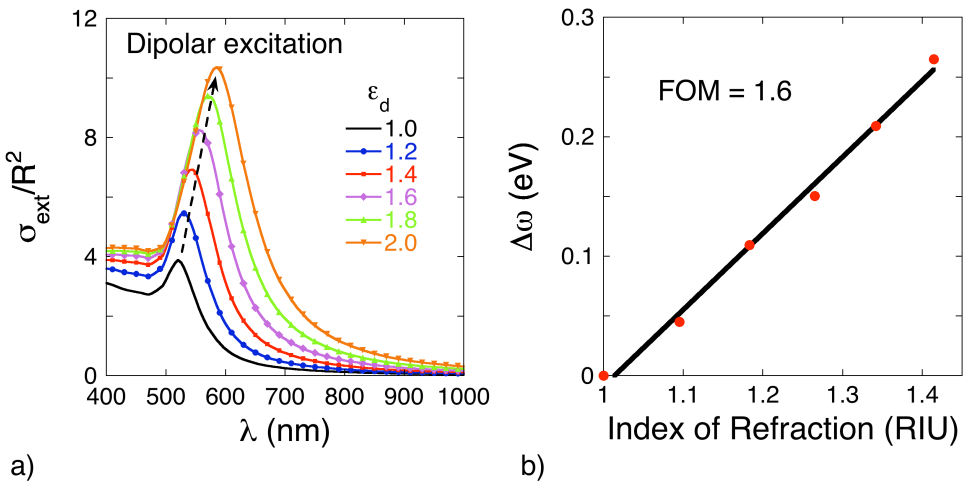

Figure 5.1: a) Calculated normalized optical extinction cross-section of a gold spherical nanoparticle with radius $R = 50$ nm for embedding media characterized by different ε_d. b) Linear plot of the shifts of the LSPRs in a) *vs.* the index of refraction of the embedding medium. The FOM value of the gold nanoparticles is also included.

with radius $R = 50$ nm to the embedding medium. In Figure 5.1 a) the calculated normalized optical extinction cross-section is plotted for varying values of the dielectric constant ε_d of the medium surrounding the sphere. The LSPR is red-shifted and its intensity increases as $\varepsilon_d = n^2$ is increased.

The efficiency of plasmonic systems as sensors is usually estimated by the Figure Of Merit (FOM). This parameter is defined as [69]:

$$FOM = \frac{m(eVRIU^{-1})}{fwhm(eV)}, \tag{5.1}$$

where m is the linear regression slope for the refractive index dependence, which indicates the ratio of the plasmon energy shift to the change in refractive index of the embedding medium, and $fwhm$ is the full width at half maximum of the resonance. Figure 5.1 b) shows the linear plot of the shifts of the LSPRs for the gold nanoparticle vs the index of refraction

of the embedding medium, n. The slope given by the linear regression is $m = 0.64$ eV/RIU, and the $fwhm = 0.39$ eV. Thus the FOM parameter for the LSPR of the gold nanoparticle is FOM= 1.6.

From the definition of the FOM value (see Eq. 5.1), one can deduce its value is increased due to large shifts of the LSPR, due to narrow LSPR, or a combination of both effects. For individual nanoparticles, the highest value obtained for the FOM so far is 5.4 for a sharply pointed gold nanostar [3]. A combination of asymmetric particles giving Fano profiles can improve these figures of merit [94]. As examples of the efficiency as sensors of Fano resonances, some estimated values for the FOM parameter of Fano resonances are 8.3 in a non-concentric disk-ring nanostructure [103], and 5.7 in a planar heptamer cluster (six nanoparticles forming a ring with another nanoparticle in the middle) [71].

5.1.1 Shift-based LSPR sensing in PCCs

In this section we study the sensitivity to the embedding medium of a nanoparticle dimer connected by a conductive linker, with the same geometry as the a system analyzed in Chapter 3. In this case, the dimer consists of two adjacent gold nanoshells, with radii $R = 55$ nm and separated by an interparticle distance $d = 1$ nm, connected by a conductive linker forming a Plasmon Conductive Cavity (PCC) (see schematics in Figure 3.1 a)).

Two different PCCs have been considered. Figure 5.2 a) shows the calculated normalized optical extinction cross-section for a dimer bridged by a conductive junction, with radius $a = 2$ nm and conductance $G = 527G_0$, for varying values of the dielectric constant of the embedding medium ε_d. In Figure 5.2 b), we plot the analog case for a wider conductive linker with radius $a = 5$ nm and conductance $G = 352G_0$. Both situations are representative of the conductively linked dimer system since the Bonding Dimer Plasmon (BDP) mode is screened, developing the

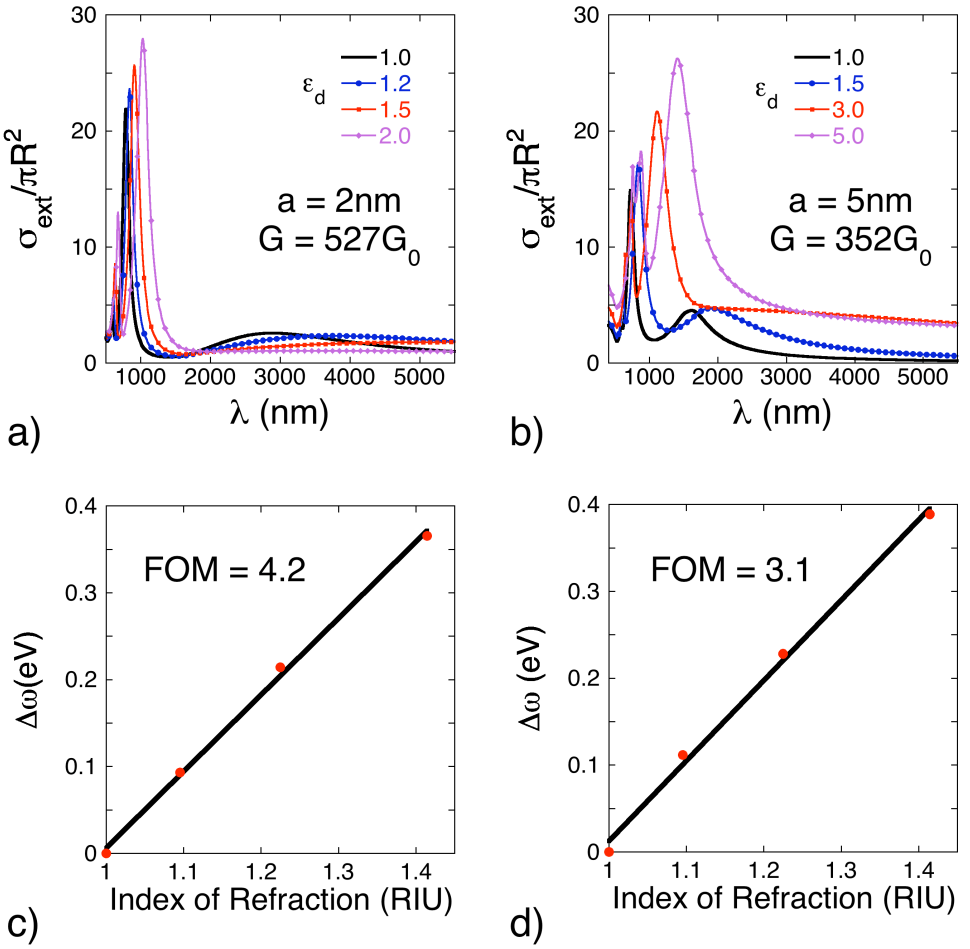

Figure 5.2: Sensitivity of a nanoparticle dimer connected by a conductive linker to the embedding medium. a) Calculated normalized optical extinction cross section for a nanoparticle dimer connected by a conductive linker with radius $a = 2$ nm and conductance $G = 527G_0$. b) Calculated normalized optical extinction cross section for a nanoparticle dimer connected by a conductive linker with radius $a = 5$ nm and conductance $G = 352G_0$. c) and d) Linear plots of the BDP shifts vs. refractive index of the embedding medium for the linker parameters in a) and b), respectively.

Screened Bonding Dimer Plasmon (SBDP) mode, and the Charge Transfer Plasmon (CTP) mode has also emerged, due to the large conductance considered. These two different conductive linkers also present different widths of the SBDP peaks and different values of conductance through the linker, which affect their sensitivity to the embedding medium, as we show in the following.

In both cases, the SBDP mode is redshifted with the refractive index n ($\varepsilon_d = n^2$) and its intensity is increased, as for the case of the isolated gold naoparticle. In contrast, the CTP mode is just slightly redshifted before vanishing. Geometry is an important factor since, for wider junctions, the CTP resonance survives for larger values of the dielectric function.

Figure 5.2 c) and d) show the linear plots of the shifts of the SBDP mode as a function of the refractive index of the embedding medium, for $a = 2$ nm and $G = 527G_0$ in c), and for $a = 5$ nm and $G = 352G_0$ in d). In the case of the $a = 2$ nm conductive linker, the slope given by the linear regression is $m = 0.88$ eV/RIU, the $fwhm = 0.21$ eV and the resulting FOM parameter for the SBDP resonance is FOM= 4.2. For the linker with radius $a = 5$ nm, the slope of the linear regression is $m = 0.93$ eV/RIU and its $fwhm = 0.30$eV, resulting in FOM= 3.1.

In spite of the fact that the CTP mode in the cases under consideration is very damped, we have also estimated its FOM value for the case in Figure 5.2 b). The slope of the linear regression is $m = 0.49$ and $fwhm = 0.43$, thus resulting in FOM = 1.1.

The FOM values for the SBDP resonance of the dimer are significantly larger than those of the isolated nanoparticle. This is not the case when we consider the CTP resonance, mainly due to the elevated $fwhm$ value of the considered case. The FOM values for the SBDP mode also show that the system with narrower conductive linker but higher conductance is more sensitive to changes in the embedding medium and, therefore, a better candidate for applications in LSPR sensing.

5.1.2 Shift-based LSPR sensing in PECs

Similarly to the case of dimers connected by PCCs, in this section we analyze the shift-based LSPR sensing for dimers connected by Plasmon-Exciton Cavities (PECs). In this kind of system, we have already explained in Chapter 4 that the BDP resonant mode splits into two plasmon-exciton modes, that we name as plexcitons, due to the coupling between the plasmon cavity resonances and the excitons. One of the modes, the E^{+}_{BDP} presents higher energy than the non-coupled BDP mode, while the E^{-}_{BDP} presents lower energy. In order to study the properties of this system for LSPR sensing we have analyzed the sensitivity to the embedding medium in a case where both plexciton modes have similar intensity. In particular, we have considered the case of a molecular linker with radius $a = 5$ nm and with an excitonic transition of energy $E_{ex} = \hbar\omega_{ex} = 2.07$ eV, corresponding to $\lambda_{ex} = 600$ nm (see also Figure 4.7 b)). This case is representative of a linked dimer, with an excitonic transition in the visible region of the spectrum, where the plexcitons present similar spectral weight.

In Figure 5.3 a) we have plotted the evolution of the calculated normalized optical extinction cross section as the dielectric constant $\varepsilon_d = n^2$ of the surrounding medium is varied. The behaviour of the low energy E^{-}_{BDP} plexciton mode is very similar to the previously studied systems, the mode red-shifts and its intensity increases. The behaviour of the high energy E^{+}_{BDP} plexciton mode is completely analogue. However, the E^{+}_{BDP} also couples to the E^{-}_{BQP}, which is the plexciton arising form the coupling of the quadrupolar plasmon cavity mode and the exciton (see Figure 4.7 b)). This mixing makes the shift of the modes appear unclear, therefore we have only considered the case of the E^{-}_{BDP} plexciton for LSPR sensing.

Figure 5.3 b) shows the linear plot of the E^{-}_{BDP} shifts vs. the refractive index of the embedding medium. The slope of the linear regression

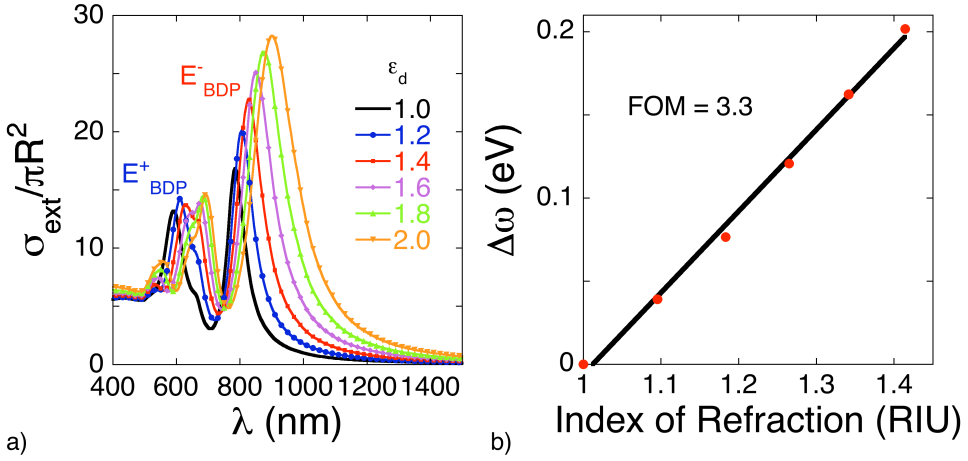

Figure 5.3: Sensitivity of a nanoparticle dimer connected by a molecular linker to the embedding medium. The parameters of the linker are the radius $a = 5$ nm and the transition energy $E_{ex} = 2.07$ eV ($\lambda_{ex} = 600$ nm). a) Evolution of the calculated normalized optical extinction cross section as the dielectric constant ε_d of the surrounding medium is varied. b) Linear plot of the E^-_{BDP} shifts vs. refractive index of the embedding medium.

is $m = 0.49$ and $fwhm = 0.15$. With this parameters, the value of the FOM parameter for the E^-_{BDP} mode is FOM $= 3.3$. This value is in-between the FOM values that we have estimated for the two considered cases of the dimer connected by conductive linkers.

5.2 Intensity-based LSPR sensing

In this section, we propose a new concept for LSPR sensing. We introduce a new paradigm, where the tuning of the plasmonic resonances in terms of their sensitivity to the embedding medium is not based on shifts, but on changes in the intensity of the resonances. To this end, we consider the same dimer as previously, connected by a molecular linker with an excitonic transition in the material forming the junction. In this

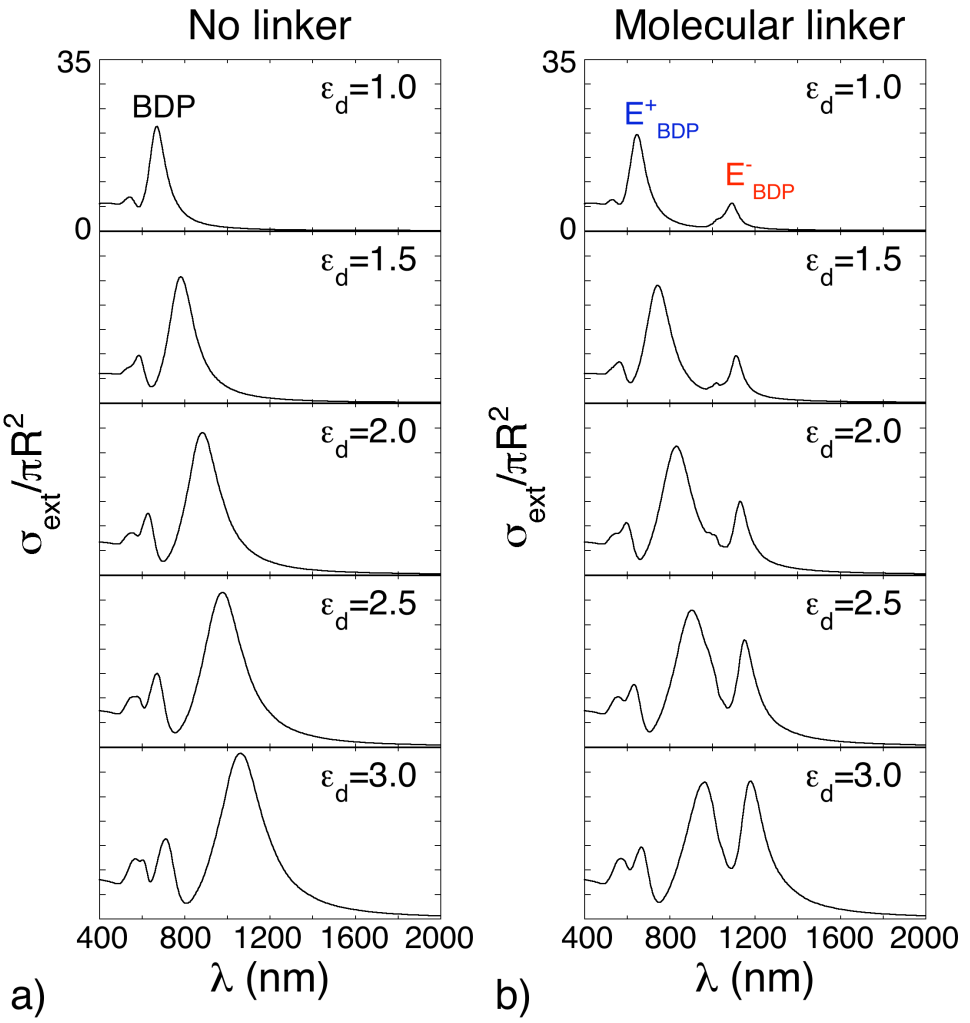

Figure 5.4: Calculated normalized optical extinction cross-section of a gold nanoparticle dimer with a separation distance $d = 1$ nm, as the dielectric embedding constant ε_d is varied. a) Disconnected dimer and b) Dimer bridged by a molecular linker with length $d = 1$ nm and radius $a = 3$ nm. The energy of the optical transition of the molecule is $E_{ex} = 1.24$ eV, corresponding to $\lambda_{ex} = 1000$ nm.

system, the plexcitonic resonances present very different intensities depending on the energy of the excitonic transition under consideration, as we have shown in Chapter 4. As we show in the following, when the intensity of the plexcitons is very different, the sensitivity to the embedding medium can be exploited in a different way in relation to the standard shift-based LSPR sensing.

Figure 5.4 shows the calculated normalized optical extinction cross-section of a gold nanoparticle dimer with a separation distance between the particles $d = 1$ nm, as the dielectric embedding medium is changed. In Fig. 5.4 a) we consider the non-connected situation, while in Figure 5.4 b) the particles are bridged by a molecular linker with radius $a = 3$ nm, characterized by an excitonic transition with energy $E_{ex} = 1.24$ eV, corresponding to $\lambda_{ex} = 1000$ nm. In the disconnected dimer, the BDP mode, which is the plasmonic resonance governing the optical spectrum, red-shifts and gains intensity as the dielectric constant of the embedding medium is increased. This behaviour shown in Figure 5.4 a) coincides with the behaviour of the isolated nanoparticle and the connected dimers considered along this chapter, and also with other nanostructures under similar conditions, and it is the basis of LSPR sensing [69]. Similarly, the high-energy E^{+}_{BDP} plexciton in Figure 5.4 b) also blue-shifts and gains intensity. In contrast, the low-energy E^{-}_{BDP} plexciton hardly red-shifts as the surrounding dielectric constant ε_d is increased, indicating that this is not an adequate resonant mode for shift-based LSPR sensing.

However, when we pay attention to the intensity of the plexcitons we observe that the intensity of the E^{-}_{BDP} plexciton changes dramatically. Whereas in the case where the dimer is in vacumm ($\varepsilon_d = 1.0$) the E^{-}_{BDP} plexciton is a small spectral feature in comparison to the E^{+}_{BDP} plexciton, when $\varepsilon_d = 3.0$ the intensity of the low-energy plexciton has even exceeded the intensity of the high-energy plexciton. This indicates that the sensitivity of the E^{-}_{BDP} plexciton can be exploited in an alternative

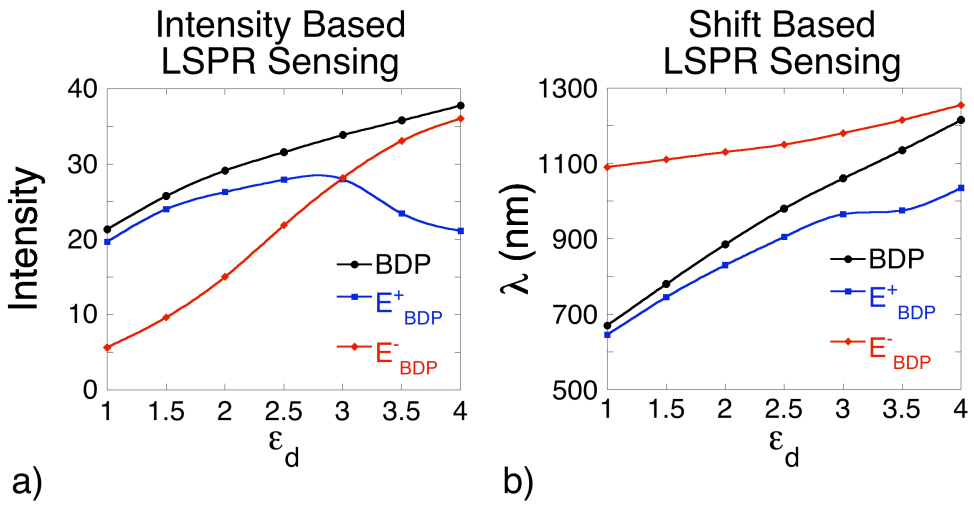

Figure 5.5: a) Variation of the intensity of the BDP, E^+_{BDP} and E^-_{BDP} modes in Figure 5.4 as a function of the dielectric constant of the embedding medium. b) Shift of the BDP, E^+_{BDP} and E^-_{BDP} modes in Figure 5.4 as a function of the dielectric constant of the embedding medium.

way.

In order to compare the changes in the intensity and the shifts, in Figure 5.5 we plot the changes in the intensity (a) and the shift (b) of the BDP (black), E^+_{BDP} (blue) and E^-_{BDP} (red) modes as the dielectric constant of the embedding medium ε_d is varied. The low-energy E^-_{BDP} plexciton mode, which is a minor spectral feature when the embedding medium is vacuum, hardly red-shifts as the surrounding dielectric constant ε_d is increased. In terms of the definition of the FOM parameter (Eq. 5.1), this means that the ratio between the shift of the resonance and its $fwhm$ is very small. In contrast, the other modes in Figure 5.5 b), the BDP and the E^+_{BDP}, present a considerable shift. However, by increasing ε_d, the E^-_{BDP} plexciton becomes a spectral feature as strong as the the E^+_{BDP} mode in terms of intensity, as shown in Figure 5.5 a). In fact, for very large values of ε_d, the intensity of E^-_{BDP} has exceeded the

intensity of E^{+}_{BDP}, since the magnitude increases in one order of magnitude. The E^{+}_{BDP} plexciton mode also increases slowly in intensity until the E^{-}_{BDP} gains enough spectral weight to become more intense than the E^{+}_{BDP}. Then, it looses intensity, indicating an inversion of the strongest mode as a consequence of the variation of the dielectric constant. We propose that this large increase in the intensity of the resonance can be used for LSPR sensing based on the variation of the intensity of the peaks, which is a novel way to probe the environment and thus, a new sensing scheme.

5.3 Summary

In this chapter we have studied the potential use of dimers connected by conductive and molecular linkers in LSPR sensing. We have explored the efficiency of these nanostructures as sensors and estimated the FOM parameters. The largest FOM value we have found is 4.2 for the SBDP mode in PCCs with large conductance through the linker, which highly improves the efficiency of the isolated nanoparticle. We have also exploited the particular behaviour of the plexciton modes of dimers connected by molecular linkers to propose a new paradigm for sensing based on changes in the intensity and emergence of plexcitonic resonances.

CONCLUSIONS

We have presented in this thesis a set of theoretical contributions to improve the understanding of the interaction between the optical properties of plasmonic nanostructures and electronic transport.

In order to explore this relation between the fields of plasmonics and nanoelectronics, we have studied the optical response of a plasmonic dimer where both parts of the nanostructure are connected by an ensemble of molecules. Both particles forming the dimer are closely spaced creating a cavity, so that the nanostructure is highly coupled. The ensemble of molecules is geometrically modelled as a cylindrical linker connecting the surfaces of the dimer in the region of maximum proximity. In order to analyze different approaches to the nature of the molecular linker, the dielectric response of its constituent material has been characterized using different models for the dielectric function.

We have shown in Chapter 2 that, when there is a conductive path connecting a nanostructure, two plasmonic resonances are mainly responsible for the optical response: the Bonding Dimer Plasmon (BDP) mode and the Charge Transfer Plasmon (CTP) mode. The BDP mode, which arises from the hybridization of the dipolar ($l = 1$) modes of the individual nanoparticles, and which is also present when the nanostructure is dis-

connected, blue-shifts and looses partially its intensity as the conductive path becomes wider. The CTP mode, which arises from the hybridization of the monopolar ($l = 0$) modes of the individual nanoparticles, and which is not present when the nanostructure is disconnected, emerges in the long-wavelength range of the optical spectrum, blue-shifting and gaining intensity as the size of the conductive path is increased. This behaviour confirms that there is a dependance of the optical response on the electronic transport through the conductive path connecting the nanostructure.

As a means to explore the relationship between the transport properties and the spectral behaviour of conductively connected plasmonic cavities, in Chapter 3 we have modelled the junction as a pure conductive linker, so that the conductance through the plasmonic cavity can be tuned. For a linker with fixed size, the BDP mode blue-shifts and looses intensity as the conductance is increased, becoming an Screened BDP mode (SBDP). The SBDP is a resonant plasmonic mode where the electric field, originally highly concentrated in the cavity, is progressively expelled from the linker, thus reducing its capacitance. The CTP mode needs very large values of conductance to emerge and, once fully formed, remains in the same spectral position as the conductance increases. We have used simple physical models to explain the evolution of the modes, and we have also considered how the size and morphology of the linker influences the optical response. Finally, by virtue of a time-scale approach, we have related the optical cycle of the plasmonic resonances to the transport time of the electrons at the electric current through the conductive linker. Thus, we have derived analytical expressions providing the thresholds of conductance for the transport properties to determine the optical response, namely, the screening of the BDP into the SBDP mode, and for the emergence of the CTP mode.

In order to consider a more realistic response of the molecular linker

connecting the dimer, in Chapter 4 we have considered that the material of the conductive linker connecting the dimer presents an excitonic transition. The consideration of a more complex dielectric response of the linker, where the conductance shows a resonant behaviour, strongly affects the optical response of the connected nanostructure. The plasmon modes of the cavity, the BDP and the Bonding Quadrupolar Plasmon (BQP), which arises from the hybridization of the quadrupolar modes ($l = 2$) of the individual nanoparticles, couple with the excitons, splitting each mode into plasmon-exciton states, named as plexcitons. The plexcitons present an anti-crossing behaviour centred in the point of intersection of the energy-line of the exciton and the energy-lines of the cavity modes. The energies of the plexcitons can be derived from a simple model of two coupled oscillators. The CTP mode emerges when the molecular linker is conductive enough. The expression for the threshold of conductance for the CTP mode, derived from time-scale arguments in Chapter 3, is confirmed to be valid.

Finally, in Chapter 5 we have explored the sensitivity of the nanoparticle dimers connected by conductive and molecular linkers to the embedding medium. This sensitivity has been previously used for Localized Surface Plasmon Resonance (LSPR) sensing, based on the shifts of the LSPRs as the dielectric environment is changed. The efficiencies of the connected dimers are expressed in terms of the Figure Of Merit (FOM) parameter, which gives the ratio of the spectral shifts per refractive index unit change. The largest value of the FOM parameter we have found is 4.2 for Plasmon Conductive Cavities (PCCs), where the conductance through the junction is very large. Due to the behaviour of plexcitonic modes when the dielectric constant of the embedding medium varies, a new paradigm for LSPR sensing is proposed. In this new model, the sensitivity of the LSPR to the environment is focused on changes in the intensity of the resonances, rather than in the spectral shifts.

We believe that this kind of studies contribute to a better understanding of the connection between transport properties and optical properties of plasmonic nanostructures. These results can improve our basic knowledge about the optics of these nanostructures with potential applications in active devices, sensors, or to probe molecular conductance and transport at high-frequencies, a regime which is inaccessible through standard electrical measurements.

APPENDIX A

BOUNDARY ELEMENT METHOD (BEM)

Maxwell's and Poisson's equations can be analytically solved using different sets of coordinates and expansions for simple geometries such as spheres, spheroids or infinite cylinders. However, when more complicated geometries are considered, numerical methods are necessary to determine the solutions of the equations, matching the boundary conditions over the interfaces which define the system and separate the different media. Among the common techniques used to perform the calculations, we can find the Finite Difference Time Domain method (FDTD) [48], the Discrete Dipole Approximation (DDA) [49] or the Boundary Element Method (BEM) [50], which is the numerical technique used along this thesis.

BEM [50, 104] expresses Maxwell's equations in terms of induced surface charge densities and currents. Namely, the three-dimensional problem consisting of the calculation of the electric and magnetic fields in the volume, $\mathbf{E}$ and $\mathbf{H}$, respectively, becomes a two-dimensional problem of surface integral equations, where a self-consistent set of induced surface charges σ_j and currents h_j are determined for every interface. This set of charges and currents satisfies the boundary conditions and couples to

the incident field so that the optical response can take place.

More explicitly, if we write the electric and magnetic fields in terms of the scalar and vector potentials as $\mathbf{E} = \frac{i\omega}{c}\mathbf{A} - \nabla\phi$ and $\mathbf{H} = \nabla \times \mathbf{A}$, where $\varepsilon = \varepsilon(\mathbf{r}, \omega)$ is the dielectric function and Lorentz's gauge $\nabla \cdot \mathbf{A} - \frac{i\omega}{c}\varepsilon\phi = 0$ has been considered, then, Maxwell's equations can be written in Gaussian units as follows [4]:

$$\begin{aligned}(\nabla^2 + k^2\varepsilon)\phi &= -4\pi(\rho/\varepsilon + \sigma_s) \\ (\nabla^2 + k^2\varepsilon)\mathbf{A} &= -\frac{4\pi}{c}(\mathbf{j} + \mathbf{m}),\end{aligned} \tag{A.1}$$

where $k = \omega/c$, $\sigma_s = \frac{1}{4\pi}\mathbf{D} \cdot \nabla(\frac{1}{\varepsilon})$ is the induced charge density on the surface separating the media, $\mathbf{m} = -\frac{i\omega}{4\pi}\phi\nabla\varepsilon$ is the induced current density on the same surface and, ρ and $\mathbf{j}$ are the external charge density and current, respectively. Having written Maxwell's equations in this manner, it can be clearly appreciated that the sources of the fields are, on the one hand, the external perturbations ρ and $\mathbf{j}$, and, on the other hand, the induced charges and currents on the interface, σ_s and $\mathbf{m}$. Consequently, the fields are the result of the propagation of these sources by means of the corresponding Green function $G_j = G_j(r) = \exp(ik_j r)/r$, where $k_j = k\sqrt{\varepsilon_j(\omega)}$).

Explicitly, the scalar and vector potentials inside medium j can be expressed, using matrix notation, as:

$$\begin{aligned}\begin{bmatrix} \phi(\mathbf{r}) \\ \mathbf{A}(\mathbf{r}) \end{bmatrix} = \int d\mathbf{r}' G_j(\mid \mathbf{r} - \mathbf{r}' \mid) \begin{bmatrix} \rho(\mathbf{r}')/\varepsilon(\mathbf{r}', \omega) \\ \mathbf{j}(r')/c \end{bmatrix} \\ + \int_S d\mathbf{s} G_j(\mid \mathbf{r} - \mathbf{s} \mid) \begin{bmatrix} \sigma_j(\mathbf{s}) \\ \mathbf{h}_j(\mathbf{s}) \end{bmatrix}.\end{aligned} \tag{A.2}$$

All the relevant elements involved in the solution of Maxwell's equations are depicted in Fig. A.1. For the sake of simplicity, a system with a single boundary is considered, where the surface separates two different media characterized by their corresponding dielectric functions ε_j, where

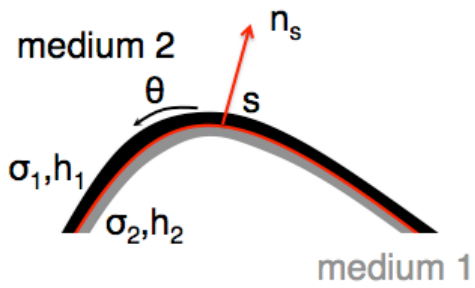

Figure A.1: Schematic representation of the elements involved in the solution of Maxwell's equations using BEM method in the presence of arbitrarily shaped sharp interfaces. In this case, the interface separating medium 1 and medium 2 is represented by a red line. $\mathbf{n}_s$ is the normal vector to the interface at a given point $\mathbf{s}$ of the interface, directed towards medium 2.

the subscripts $j = 1, 2$ refer to the media 1 and 2, respectively. The consideration of the ordinary boundary conditions for the electric and magnetic fields leads to the following set of equations:

$$G_1\sigma_1 - G_2\sigma_2 = -(\varphi_1 - \varphi_2) \tag{A.3}$$

$$G_1\mathbf{h}_1 - G_2\mathbf{h}_2 = -(\mathbf{g}_1 - \mathbf{g}_2), \tag{A.4}$$

which refer to the continuity of the parallel component of the electric field and the normal component of the magnetic field. The continuity of the parallel component of the magnetic field and the normal component of the electric displacement lead to the following relations:

$$H_1\mathbf{h}_1 - H_2\mathbf{h}_2 + p\mathbf{n}_s G_1\sigma_1 = -\mathbf{q}_1 + \mathbf{q}_2 - p\mathbf{n}_s\varphi_1 \tag{A.5}$$

$$\begin{aligned}\frac{1}{ik}(\varepsilon_1 H_1\sigma_1 - \varepsilon_2 H_2\sigma_2) - \varepsilon_1\mathbf{n}_s G_1\cdot\mathbf{h}_1 + \varepsilon_2\mathbf{n}_s G_2\cdot\mathbf{h}_2 \\ = \varepsilon_1\big(\mathbf{n}_s\cdot\mathbf{g}_1 - \frac{f_1}{ik}\big) - \varepsilon_2\big(\mathbf{n}_s\cdot\mathbf{g}_2 - \frac{f_2}{ik}\big).\end{aligned} \tag{A.6}$$

In these equations

$$\begin{bmatrix}\varphi_j(\mathbf{s}) \\ f_j(\mathbf{s})\end{bmatrix} = \int d\mathbf{r}\begin{bmatrix}1 \\ \mathbf{n}_s\cdot\nabla_s\end{bmatrix} G_j(\mid \mathbf{s}-\mathbf{r}\mid)\frac{\rho(\mathbf{r})}{\varepsilon(\mathbf{r},\omega)}, \tag{A.7}$$

and

$$\begin{bmatrix} \mathbf{g}_j(\mathbf{s}) \\ \mathbf{q}_j(\mathbf{s}) \end{bmatrix} = \frac{1}{c} \int d\mathbf{r} \begin{bmatrix} 1 \\ \mathbf{n}_s \cdot \nabla_s \end{bmatrix} G_j(\mid \mathbf{s} - \mathbf{r} \mid)\mathbf{j}(\mathbf{r}), \tag{A.8}$$

where $H_j(\mathbf{s} - \mathbf{s}') = \mathbf{n}_s \cdot \nabla_s G_j(\mid \mathbf{s} - \mathbf{r} \mid)\mathbf{j}(\mathbf{r}) \pm 2\pi\delta(\mathbf{s} - \mathbf{s}')$, with positive sign for $j = 1$ and negative sign for $j = 2$, $p = ik(\varepsilon_2\varepsilon_1)$ and $\mathbf{n}_s$ is chosen to be directed towards medium 2.

If the surface integrals are discretised using N points, then, Eq. (A.3) to (A.6) become a set of $8N$ linear equations which can be numerically solved through algebraic matrix inversion techniques. Once the surface charges σ_j and currents $\mathbf{h}_j$ are determined, the scalar and vector potential can be calculated as well using Eq. (A.2). Finally, the electric and magnetic fields can be determined from the potentials, as usual:

$$\mathbf{E} = \frac{i\omega}{c}\mathbf{A} - \nabla\phi, \tag{A.9}$$

$$\mathbf{H} = \nabla \times \mathbf{A}. \tag{A.10}$$

Notice that the consideration of frequency-dependent dielectric functions characterizing the media which define the system and the sharpness of the boundaries separating the media, are the only assumptions which have been made.

APPENDIX B

COUPLING BETWEEN ELECTRONIC EXCITATIONS AND OPTICAL MODES: VACUUM RABI SPLITTING

The coupled system consisting of an optical cavity with atoms inside often presents a more complex behaviour in comparison to the individual behaviours of either the cavity or the atoms. In particular, it has been long known that, when a collection of atoms is placed inside a cavity, the transmission resonances of the cavity split. This energy splitting, usually named as Rabi splittting, has been considered as the manifestation of the quantum nature of the electromagnetic field, and it attracted much attention a few years ago in the field of quantum optics due to its importance in the understanding of phenomena such as optical bistability and laser action [89]. However, later studies using classical models showed that the resonances of an empty-cavity can also split due to the effects of linear absorption and dispersion, resulting this splitting totally identical to the vacuum Rabi splitting calculated from a quantum electrodynamics perspective [105].

Taking into account that the atoms or molecules inside a cavity can

be viewed as electronic excitations, the physics of this system can be easily understood in terms of coupled oscillators. In this appendix we use a quantum oscillator model to derive a mathematical expression for the vacuum Rabi splitting [106], where we consider a system of N quantum-mechanical harmonic oscillators representing the electronic excitations coupled to an optical mode, which is referred to as the zero oscillator, ignoring dissipation effects in either oscillator.

The hamiltonian of a collection of N harmonic oscillators, each of them coupled to the oscillator representing the cavity mode, the zero oscillator, is given by [106]:

$$H = \frac{p_0^2}{2} + \frac{\omega_0^2}{2}x_0^2 + \frac{1}{2}\sum_{i=1}^{N}(p_i^2 + \omega_1^2 x_i^2) - \alpha\sum_{i=1}^{N} x_0 x_i, \tag{B.1}$$

where p_0 and x_0 are the momentum and the position of the zero oscillator, p_i and x_i are the momentum and the position of the i oscillator, and ω_0 and ω_1 are the frequencies of the cavity mode and the electronic transitions, respectively. The term proportional to α represents the interaction between the cavity mode and the electronic oscillations. This Hamiltonian can be expressed in terms of the creation and annihilation operators, a^+ and a, as:

$$H = \hbar\omega_0 a_0^+ a_0 + \sum_{i=1}^{N}\hbar\omega_1 a_i^+ a_i - \frac{\hbar\alpha'}{2}\sum_{i=1}^{N}(a_0^+ a_i + a_i^+ a_0) + C_0, \tag{B.2}$$

where $\alpha' = \alpha/\sqrt{\omega_0\omega_1}$, $C_0 = \hbar/2(\omega_0 + N\omega_1)$.

In order to obtain the spectrum, a linear transformation diagonalizing the Hamiltonian H_{osc} can be found:

$$H_{osc} = \sum_{i=1}^{N}\hbar\Omega_i b_i^+ b_i \tag{B.3}$$

$$b_i = \sum_j A_{ij} a_j \tag{B.4}$$

where the energy is measured relative to C_0. Then, using the relation $[b, H_{osc}] = \hbar\Omega_n b_n$, it is obtained that there are $N-1$ degenerate frequencies $\Omega = \omega_1$ and two non-degenerate frequencies given by:

$$\Omega_{\pm} = \frac{(\omega_0 + \omega_1)}{2} \pm \frac{1}{2}\sqrt{(\omega_0 - \omega_1)^2 + \alpha'^2 N}, \tag{B.5}$$

so that, the Rabi frequency at resonance ($\omega_0 = \omega_1$), is given by:

$$\Delta\Omega = \sqrt{(\alpha')^2 N} = \frac{\alpha}{\omega_1}\sqrt{N}, \tag{B.6}$$

which is proportional to the number N of oscillators in our system. Thus, simply by multiplying Eq. (B.5) by $\hbar$, we obtain the equation we use in Chapter 4 for the splitting of the modes (see Eq. (4.4)):

$$E_{\pm} = \frac{E_{SP} + E_{ex}}{2} \pm \Big[\Big(\frac{\hbar\Omega_R}{2}\Big)^2 + \frac{1}{4}(E_{SP} - E_{ex})^2\Big]^{1/2}. \tag{B.7}$$

BIBLIOGRAPHY

1. Y. Imry, *Introduction to Mesoscopic Physics*, Oxford University Press, 1997.

2. U. Leonhardt, "News & Views: Invisibility cup", *Nat. Photonics* **1**, 207 (2007).

3. N.J. Halas, S. Lal, W.S. Chang, S. Link and P. Nordlander, "Plasmons in strongly coupled metallic nanostructures", *Chem. Rev.* **111**, 3913 (2011).

4. J. D. Jackson, *Classical Electrodynamics, 3rd Ed.*, John Wiley & Sons, Inc., New York, 1999.

5. P.A. Tipler and R.A. Llewellyn, *Modern Physics, 3rd Ed.*, W.H. Freeman and Company, New York, 1999.

6. G. Binning, H. Rohrer. Ch. Gerber and E. Weibel, "Surface studies by scanning tunneling microscopy", *Phys. Rev. Lett.* **49**, 57 (1982).

7. P.N. Prasad, *Nanophotonics*, John Wiley & Sons, Inc., New York, 2004.

8. P. Guardia, J. Pérez-Juste, A. Labarta, X. Batlle and L.M. Liz-Marzán, "Heating rate influence on the synthesis of iron oxide nanoparticles: the case of decanoic acid", *Chem. Comm.* **46**, 6108, (2010).

9. J. Hwang, M. Pototschnig, R. Lettow, G. Zumofen, A. Renn, S. Götzinger and V. Sandoghdar, "A single-molecule optical transistor", *Nature* **460**, 08134, (2009).

10. J. Renger, R. Quidant and L. Novotny, "Enhanced nonlinear response from metal surfaces", *Opt. Express* **19**, 1777, (2011).

11. R. Sapienza, M. Leonetti, L.S. Froufe-Pérez, J.F. Galisteo-López, C. Conti and C. López, "Optical amplification enhancement in photonic crystals", *Phys. Rev. A* **83**, 023801, (2011).

12. T. Vo-Dinh, B.M. Cullum and D. Stokes, "Nanosensors and biochips: frontiers in biomolecular diagnostics", *Sensors and Actuators B* **74**, 2, (2001).

13. S.A. Maier, *Plasmonics*, Springer, New York, 2007.

14. G. Mie, "Contributions to the optics of turbid media, particularly of colloidal metal solutions", *Ann. Phys.* **25**, 377 (1908).

15. R.H. Ritchie, "Plasma losses by fast electrons in thin films", *Phys. Rev.* **106**, 874 (1957).

16. C.J. Powell and J.B. Swan, "Effect of oxidation on the characteristic loss spectra of Aluminum and Magnesium", *Phys. Rev.* **118**, 640 (1960).

17. H. Raether, *Surface-Plasmons on Smooth and Rough Surfaces and on Gratings*, Springer, New York, 1988.

18. C.F. Bohren and D.R. Huffman, *Absorption and Scattering of Light by Small Particles*, John Wiley & Sons, Inc., New York, 1983.

19. N.J. Halas,"Plasmonics: An emerging field fostered by Nano Letters", *Nano Lett.* **10**, 3816, (2010).

20. A.D. McFarland and R.P. Van Duyne, "Single silver nanoparticles as real-time optical sensors with Zeptomole sensitivity", *Nano Lett.* **3**, 1057, (2003).

21. H. Xu, J. Aizpurua, M. Käll and P. Apell, "Electromagnetic contributions to single-molecule sensitivity in surface-enhanced Raman scattering", *Phys. Rev. E* **62**, 4318 (2000).

22. M.R. Choi, K.J. Stanton-Maxey, J.K. Stanley, C.S. Levin, R. Bardhan, D. Akin, S. Badve, J. Sturgis, J.P. Robinson, R. Bashir, N.J. Halas and S.E. Clare,"A cellular Trojan horse for delivery of therapeutic nanoparticles into tumors", *Nano Lett.* **7**, 3759, (2007).

23. H. Atwater and A. Polman,"Plasmonics for improved photovoltaic devices", *Nat. Materials* **9**, 207, (2010).

24. Y.B. Zheng, Y. Yang, L. Jensen, L. Fang, B.K. Juluri, A.H. Flood, P.S. Weiss, J.F. Stoddart and T.J. Huang, "Active molecular plasmonics: controlling plasmon resonances with molecular switches", *Nano Lett.* **9**, 819 (2009).

25. M. Pelton, J. Aizpurua and G. W. Bryant, "Metal-nanoparticle plasmonics", *Laser & Photon. Rev.* **2**, 136-159 (2008).

26. S. Lal, S. Link and N. J. Halas, "Nano-optics from sensing to waveguiding", *Nature Photonics* **1**, 641 (2007).

27. J. Aizpurua, P. Hanarp, D.S. Sutherland, M. Käll, G.W. Bryant and F. J. García de Abajo, "Optical properties of gold nanorings", *Phys. Rev. Lett.* **90**, 057401 (2003).

28. I. Romero, J. Aizpurua, F. J. García de Abajo and G. W. Bryant, "Plasmons in nearly touching metallic nanoparticles: singular response in the limit of touching dimers", *Opt. Express* **14**, 9988 (2006).

29. J.B. Lassiter, J. Aizpurua, L.I. Hernández, D.W. Brandl, I. Romero, S. Lal, J.H. Hafner, P. Nordlander and N.J. Halas, "Close encounters between two nanoshells", *Nano Lett.* **8**, 1212 (2008).

30. M.W. Knight and N.J. Halas, "Nanoshells to nanoeggs to nanocups: optical properties of reduced symmetry core-shell nanoparticles beyond the quasistatic limit", *New. J. Phys.* **10**, 105006 (2008).

31. M. Schnell, A. García-Etxarri, A. Huber, K. Crozier, J. Aizpurua and R. Hillenbrand, "Controlling the near-field oscillations of loaded plasmonic nanoatennas", *Nat. Photonics* **3**, 287 (2009).

32. H. Wei, A. Reyes-Coronado, P. Nordlander, J. Aizpurua and H. Xu, "Multipolar plasmon resonances in individual Ag nanorice", *ACSNano* **4**, 2649 (2010).

33. C.L. Nehl, H. Liao and J.H. Hafner, "Optical properties of star-shaped gold nanoparticles", *Nano Lett.* **6**, 683 (2006).

34. M. Dressel and G. Grüner, *Electrodinamics of Solids*, Cambridge University Press, U.K., 2002.

35. C. Kittel, *Introduction to Solid State Physics, 8th Ed.*, John Wiley & Sons, Inc., New York, 2005.

36. A. Rivacoba, N. Zabala and J. Aizpurua, "Image potential in scanning transmission electron microscopy", *Prog. Surf. Sci.* **65**, 1 (2000).

37. J. Lindhard, "Image potential in scanning transmission electron microscopy", *KGL. dansk. Vid. Scls. Mat. Fys. Medd.* **28** (8), (1954).

38. N.D. Mermin, "Lindhard dielectric function in the relaxation-time approximation", *Phys. Rev. B* **1**, 2362 (1970).

39. E.D. Palik, *Handbook of optical constants*, Academic Press, Inc. (1985).

40. P.B. Johnson and R.W. Christy, "Optical constants of the noble metals", *Phys. Rev. B*, **6**, 4370 (1972).

41. A.V. Zayats and I.I. Smolyaninov, "Near-field photonics: surface plasmon polaritons and localized surface plasmons", *J. Opt. A: Pure Appl. Opt.* **5** 16 (2003).

42. S.P. Apell, P.M. Echenique and R.H. Ritchie, "Sum rules for surface plasmon frequencies", *Ultramicroscopy* **65**, 53 (1996).

43. K.L. Kliewer and R. Fuchs, "Collective electronic motion in a metallic slab", *Phys. Rev.* **157**, 498 (1967).

44. C.A. Pfeiffer, E.N. Economou and K.L. Ngai "Surface polaritons in a circularly interface: surface plasmons", *Phys. Rev. B* **10**, 3038 (1974).

45. L.C. Davis, "Electrostatic edge modes of a dielectric wedge", *Phys. Rev. B* **14**, 5523 (1976).

46. R. Ruppin, "Surface modes of two spheres", *Phys. Rev. B* **26**, 3440 (1982).

47. F.J. García-Vidal, J.M. Pitarke and J.B. Pendry, "Effective medium theory of the optical properties of aligned carbon nanotubes", *Phys. Rev. Lett.* **78**, 4289 (1997).

48. A. Taflove, "Application of the finite-difference time-domain method to sinusoidal steady-state electromagnetic-penetration problems", *Electromagnetic Compatibility, IEEE Transaction on* **EMC-22**, 191 (1980).

49. E.M. Purcell and C.R. Pennypacker, "Scattering and absorption of light by nonspherical dielectric grains", *Astro. J.* **186**, 705 (1973).

50. F.J. García de Abajo and A. Howie, "Relativistic electron energy loss and electron-induced photon emission in inhomogeneus dielectrics", *Phys. Rev. Lett.* **80**, 5180 (1998).

51. S. Link, M.B. Mohamed and M.A. El-Sayed, "Simulation of the optical absorption spectra of gold nanorods as a function of their aspect ratio and the effect of the medium dielectric constant", *J. Phys. Chem. B* **103**, 3073 (1999).

52. C. Radloff and N.J. Halas, "Plasmonic properties of concentric nanoshells", *Nano Lett.* **4**, 1323 (2004).

53. C.L. Nehl, N.K. Grady, G.P. Goodrich, F. Tam, N.J. Halas and J.H. Hafner, "Scattering spectra of single gold nanoshells", *Nano Lett.* **4**, 2355 (2004).

54. E. Prodan, C. Radloff, N.J. Halas and P. Nordlander, "A hybridization model for the plasmon response of complex nanostructures", **302**, 419 (2003).

55. P. Nordlander, C. Oubre, E. Prodan, K. Li and M. I. Stockman, "Plasmon hybridization in nanoparticle dimers", *Nano Lett.* **4**, 899 (2004).

56. H. Park, J. Park, A.K.L. Lim, E.H. Anderson, A.P. Alivisatos and P.L. McEuen,"Nanomechanical oscillations in a single-C_{60} transistor", *Nature* **407**, 57, (2000).

57. T. Dadosh, Y. Gordin, R. Krahne, I. Khivrich, D. Mahalu, V. Frydman, J. Sperling, A. Yacoby and I. Bar-Joseph, "Measurements of the conductance of single conjugated molecules", *Nature* **436**, 677, (2005).

58. G. V. Nazin, X. H. Qiu and W. Ho"Visualization and spectroscopy of a metal-molecule-metal bridge", *Science* **302**, 77, (2003).

59. L. Venkataraman, J.E. Klare, I.W. Tam, C. Nuckolls, M.S. Hybertsen and M.L. Steigerwald,"Single-molecule circuits with well-defined molecular conductance", *Nano Letters* **6**, 458, (2006).

60. P. Banerjee, D. Conklin, S. Nanayakkara, T.H. Park, M. J. Therien, and D. A. Bonnell, "Plasmon-induced electrical conduction in molecular devices", *ACS Nano* **4**, 1019, (2010).

61. J. Liao, J.S. Agustsson, S. Wu, C. Schonenberger, M. Calame, Y. Leroux, M. Mayor, O. Jeannin, Y.-F. Ran, S.-X. Liu, and S. Decurtins, "Cyclic conductance switching in networks of redox-active molecular junctions", *Nano Letters* **10**, 759, (2010).

62. P. Hyldgaard, "Density-functional theory of nonequilibrium tunneling", *Phys. Rev. B* **78**, 165109 (2008).

63. B. Wu and J.C. Cao, "Noise of Kondo dot with ac gate: Floquet-Green's function and noncrossing approximation approach" *Phys. Rev. B* **81**, 085327 (2010).

64. M. Heyl and S. Kehrein, "Nonequilibrium steady state in a periodically driven Kondo model", *Phys. Rev. B* **81**, 144301 (2010).

65. G.A. Wurtz, P.R. Evans, W. Hendren, R. Atkinson, W. Dyckson, R.J. Pollard and A.V. Zayats, "Molecular plasmonics with tunable exciton-plasmon coupling strength in J-aggregate hybridized Au nanorod assemblies", *Nano Lett.* **7**, 1297 (2007).

66. N.T. Fofang, T. Park, O. Neumann, N.A. Mirin, P. Nordlander and N.J. Halas, "Plexciton nanoparticles: plasmon-exciton coupling in nanoshell-J-aggregates complexes", *Nano Lett.* **8**, 3481 (2008).

67. P. Andrew and W.L. Barnes, "Energy transfer across a metal film mediated by surface plasmon polaritons", *Science* **306**, 1002 (2004).

68. E. Hendry, F.J. García-Vidal, L. Martín-Moreno, J. Gómez Rivas, M. Bonn, A.P. Hibbins and M.J. Lockyear, "Optical control over surface-plasmon-polariton-assisted THz transmission through a slit aperture", *Phys. Rev. Lett.* **100**, 123901 (2008).

69. L.J. Sherry, S.H. Chang, G.C. Schatz and R.P. Van Duyne, "Localized surface plasmon resonance spectroscopy of single silver nanocubes", *Nano Lett.*, **5** 2034 (2005).

70. M. Miller and A. Lazarides, "Sensitivity of metal nanoparticle plasmon resonance band position to the dielectric environment as observed in scattering", *J. Opt. A* **8**, 239 (2006).

71. J.B. Lassiter, H. Sobhani, J.A. Fan, J. Kundu, F. Capasso, P. Nordlander and N.J. Halas, "Fano resonances in plasmonic nanoclusters: geometrical and chemical tunability", *Nano Lett.* **10**, 3184 (2010).

72. K.H. Su, Q.H. Wei, X. Zhang, J.J. Mock, D.R. Smith and S. Schultz, "Interparticle coupling effects on plasmon resonances of nanogold particles", *Nano Lett.* **3**, 1087 (2003).

73. B.M. Reinhard, M. Siu, H. Agarwal, A.P. Alisavatos and J. Liphardt, "Calibration of dynamic molecular rulers based on plasmon coupling between gold nanoparticles", *Nano Lett.* **5**, 2246 (2005).

74. P.K. Jain, W. Huang and M.A. El-Sayed, "On the universal scaling behavior of the distance decay of plasmon coupling in metal nanoparticle pairs: a plasmon ruler equation", *Nano Lett.* **7**, 2080 (2007).

75. N. Zabala, A. Rivacoba and P.M. Echenique, "Coupling effects in the excitations by an external electron beam near close particles", *Phys. Rev. B* **56**, 7623 (1997).

76. T. Atay, J.H. Song and A.V. Nurmikko, "Strongly interacting plasmon nanoparticle pairs: from dipole-dipole interaction to conductively coupled regime", *Nano Lett.* **4**, 1627-1631 (2004).

77. D.R. Ward, N.J. Halas, J.W. Ciszek, J.M. Tour, Y.Wu, P. Nordlander and D. Natelson, "Simultaneous measurements of electronic conduction and Raman response in molecular junctions", *Nano Lett.* **8**, 919 (2008).

78. M. Danckwerts and L. Novotny, "Optical frequency mixing at coupled gold nanoparticles", *Phys. Rev. Lett.* **98**, 026104 (2007).

79. J. Zuloaga and P. Nordlander, "Quantum description of the plasmon resonances of a nanoparticle dimer", *Nano Lett.* **9**, 887-891 (2009).

80. S.Jan van der Molen, J. Liao, T. Kudernac, J.S. Agustsson, L. Bernard, M. Calame, B. J. van Wees, B. L. Fernga and C. Schönenberger, "Light-controlled conductance switching of ordered metal-molecule-metal devices", *Nano Lett.* **9**, 76-80 (2009).

81. Y.F. Chau, Y.J. Lin and D. P. Tsai, "Enhanced surface plasmon resonance based on the silver nanoshells connected by the nanobars", *Opt. Express* **18**, 3510-3518 (2010).

82. M. Fox, *Optical Properties of Solids*, Oxford University Press Inc., New York, USA, 2001.

83. H. Xu, E.J. Bjerneld, J. Aizpurua, P. Apell, L. Gunnarsson, S. Petronis, B. Kasemo, C. Larsson, F. Höök and M. Käll, "Interparticle coupling effects in surface-enhanced Raman scattering", *Proc. SPIE* **4258**, 35 (2001).

84. N. Large, M. Abb, J. Aizpurua, and O. L. Muskens, "Photoconductively loaded plasmonic nanoantenna as building block for ultracompact optical switches", *Nano Lett.* **10**, 1741 (2010).

85. D.E. Gómez, K.C. Vernon, P. Mulvaney and T.J. Davis, "Surface plasmon mediated strong exciton-photon coupling in semiconductor nanocrystals", *Nano Lett.* **10** 274 (2010).

86. J. Dintinger, S. Klein and T.W. Ebbesen, "Molecule-surface plasmon interactions in hole arrays: enhanced absorption, refractive index changes and all-optical switching", *Adv. Mat.* **18** 1267 (2006).

87. A.O. Govorov and I. Carmeli, "Hybrid structures composed of photosynthetic system and metal nanoparticles: plasmon enhancement effect", *Nano Lett.* **7** 620 (2007).

88. J.J. Sánchez-Mondragón, N.B. Naroznhy and J.H. Eberly, "Theory of spontaneous-emission line shape in an ideal cavity", *Phys. Rev. Lett.* **51**, 550 (1983).

89. G.S. Agarwal, "Vacuum-field Rabi splittings in microwave absorption by Rydberg atoms in a cavity", *Phys. Rev. Lett.* **53**, 1732 (1984).

90. A.J. Haes and R.P. Van Duyne, "A nanoscale optical biosensor: sensitivity and selectivity of an approach based on the localized surface plasmon resonance spectroscopy of triangular silver nanoparticles", *J. Am. Chem. Soc.* **124** 10596 (2002).

91. J.M. Nam, C.S. Thaxton and C.A. Mirkin, "Nanoparticle-based bio-bar codes for the ultrasensitive detection of proteins", *Science* **301** 1884 (2003).

92. E. Galopin, J. Niedziólka-Jönsson, A. Akjouj, Y. Pennec, B. Djafari-Rouhani, A. Noual, R. Boukherroub and S. Szunerits, "Sensitivity of plasmonic nanostructures coated with thin oxide films for refractive index sensing: experimental and theoretical investigations", *J. Phys. Chem. C*, **114** 11769 (2010).

93. E.M. Larsson, J. Alegret, M. Käll and D.S. Sutherland, "Sensing characteristics of NIR localized surface plasmon resonances in gold nanorings for application as ultrasensitive sensors", *Nano Lett.* **7**, 1256 (2007).

94. B. Luk'yanchuk, N.I. Zheludev, S.A. Maier, N.J. Halas, P. Nordlander, H. Giessen and C.T. Chong, "The Fano resonance in plasmonic nanostructures and nanomaterials", *Nat. Mat.* **9**, 707 (2010).

95. J.A. Fan, K. Bao, C. Wu, J. Bao, R. Bardhan, N.J. Halas, V.N. Manoharan, G. Shvets, P. Nordlander and F. Capasso, "Fano-like interference in self-assembled plasmonic quadrumer clusters", *Nano Lett.* **10**, 4680 (2010).

96. J. Kessler and J. Lorenz, "Experimental verification of the Fano effect", *Phys. Rev. Lett.* **24**, 87 (1970).

97. C.P. Holfeld, F. Löser, M. Sudzius, K. Leo, D.M. Whittaker and K. Köhler, "Fano resonances in semiconductor superlattices", *Phys. Rev. Lett.* **81**, 874 (1998).

98. U. Fano, "Effects of configuration interaction on intensities and phase shifts", *Phys. Rev.* **124**, 1866 (1961).

99. C.L. Garrido-Alzar, M.A.G. Martínez and P. Nussenzveig, "Classical analog of electromagnetically induced transparency", *Am. J. Phys.* **70**, 37 (2002).

100. D.M. Riffe, "Classical Fano oscillator", *Phys. Rev. B* **84**, 064308 (2011).

101. N. Verellen, Y. Sonnefraud, H. Sobhani, F. Hao, V.V. Moshchalkov, P. Van Dorpe, P. Nordlander and S.A. Maier, "Fano resonances in individual coherent plasmonic cavities", *Nano Lett.* **9**, 1663 (2009).

102. Z. Zhang, A. Weber-Bargioni, S.W. Wu, S. Dhuey, S. Cabrini and P.J. Schuck, "Manipulating nanoscale light fields with the asymmetric bowtie nano-colorsorter", *Nano Lett.* **9**, 4505 (2009).

103. F. Hao, Y. Sonnefraud, P. Van Dorpe, S.A. Maier, N.J. Halas and P. Nordlander, "Symmetry breaking in plasmonic nanocavities: subradiant LSPR sensing and tunable Fano resonances", *Nano Lett.* **8**, 3983 (2008).

104. F.J. García de Abajo and A. Howie, "Retarded field calculation of electron energy loss in inhomogeneous dielectrics", *Phys. Rev. B* **65**, 115418 (2002).

105. Y. Zhu, D.J. Gauthier, S.E. Morin, Q. Wu, H.J. Carmichael and T.W. Mossberg, "Vacuum Rabi splitting as a feature of linear-dispersion theory: analysis and experimental observations", *Phys. Rev. Lett.* **64**, 2499 (1990).

106. S. Rudin and T.L. Reinecke, "Oscillator model for vacuum Rabi splitting in microcavities", *Phys. Rev. B* **59**, 10227 (1999).

PUBLICATIONS

- A. Reyes-Coronado, O. Pérez-González, N. Zabala and J. Aizpurua, "Optical forces in metallic nanoparticles induced by fast electron beams", *Proc. of the 2nd Int. Congress on Advanced Electromagnetic Materials in Microwave and Optics*, published on-line (http://proceedings.metamorphose-vi.org/2008/), (2008).

- O. Pérez-González, N. Zabala, A.G. Borisov, N.J. Halas, P. Nordlander and J. Aizpurua, "Optical spectroscopy of conductive junctions in plasmonic cavities", *Nano Lett.* **10**, 3090 (2010).

- O. Pérez-González, N. Zabala and J. Aizpurua, "Optical characterization of charge transfer (CTP) and bonding dimer (BDP) plasmons in linked interparticle gaps", *New J. Phys.* **13**, 083013 (2011).

- N. Zabala, O. Pérez-González, P. Nordlander and J. Aizpurua, "Coupling of nanoparticle plasmons with molecular linkers", *Proc. of SPIE* **8096**, 80961L (2011).

- O. Pérez-González, N. Zabala, P. Nordlander and J. Aizpurua, "LSPR sensing using plexcitonic systems", manuscript to be submitted.

ACRONYMS

Acronyms used along this thesis (in order of appearance):

- **SPR** - Surface Plasmon Resonance
- **LSPR** - Localized Surface Plasmon Resonance
- **NIR** - Near-Infra-Red
- **EELS** - Electron Energy Loss Spectroscopy
- **SP** - Surface Plasmon
- **SPP** - Surface Plasmon Polariton
- **FDTD** - Finite Difference Time Domain
- **DDA** - Discrete Dipole Approximation
- **BEM** - Boundary Element Method
- **BDP** - Bonding Dimer Plasmon
- **CTP** - Charge Transfer Plasmon
- **PC** - Plasmonic Cavity

- **BQP** - Bonding Quadrupolar Plasmon
- **SERS** - Surface Enhanced Raman Scattering
- **PCC** - Plasmonic Conductive Cavity
- **SBDP** - Screened Bonding Dimer Plasmon
- **FWHM** - Full Width at Half Maximum
- **PEC** - Plasmon-Exciton Cavity

LIST OF FIGURES